Experimental study of H- negative ion production by electron cyclotron resonance plasmas

Spyridon Aleiferis

To cite this version:

Spyridon Aleiferis. Experimental study of H- negative ion production by electron cyclotron resonance plasmas. Plasma Physics [physics.plasm-ph]. Université Grenoble Alpes; Panepistīmio Patrṓn, 2016. English. NNT : 2016GREAI032 . tel-01492954

HAL Id: tel-01492954
https://theses.hal.science/tel-01492954v1

Submitted on 20 Mar 2017

THÈSE

Pour obtenir le grade de

DOCTEUR DE LA COMMUNAUTE UNIVERSITE GRENOBLE ALPES

préparée dans le cadre d’une cotutelle *entre la Communauté Université Grenoble Alpes et l’Université de Patras*

Spécialité : **Mécanique des fluides, procédés, énergétique**
Arrêté ministériel : le 6 janvier 2005 - 7 août 2006

Présentée par

Spyridon ALEIFERIS

Thèse dirigée par **Stéphane BÉCHU** et
codirigée par **Panagiotis SVARNAS**

préparée au sein du **Laboratoire de Physique Subatomique et de Cosmologie** et du **Laboratoire des Hautes Tensions**

dans **l’École Doctorale Ingénierie - Matériaux, Mécanique, Environnement, Energétique, Procédés, Production** et **l’École Doctorale de Génie Électrique et d’Informatique**

Étude expérimentale de la production d’ions négatifs H^- par des plasmas à la résonance cyclotron électronique

Thèse soutenue publiquement le **07/07/2016**,
devant le jury composé de :

M. Thierry BELMONTE
Directeur de Recherche à l’Institut Jean Lamour, Président
M. Igor KAGANOVICH
Directeur de Recherche à l’Université de Princeton, Rapporteur
M. Khaled HASSOUNI
Professeur à l’Université Paris XIII, Rapporteur
M. Stéphane BÉCHU
Chargé de Recherche au LPSC, Directeur de thèse
M. Panagiotis SVARNAS
Professeur Assistant à l’Université de Patras, Co-directeur de thèse
Mme. Eleftheria PYRGIOTI
Professeur Assistant à l’Université de Patras, Membre
M. Kyriakos HIZANIDIS
Professeur à l’Université Polytechnique Nationale d'Athènes, Membre

Dedicated to my family for their support

and to Maria for being by my side.

Acknowledgments

The present thesis is the result of my work during the last four years. The presented experiments have been realized in the High Voltage Laboratory of the Electrical and Computer Engineering Department of the University of Patras (Greece) and the Laboratory of Subatomic Physics and Cosmology of the University of Grenoble (France), in the frame of an international cotutelle of doctoral thesis.

First of all, I offer my profoundest gratitude to my thesis advisors, Prof. Panagiotis Svarnas (University of Patras) and Dr. Stéphane Béchu (University of Grenoble), for their inspiring guidance, the patience and the encouragement during these years.

Besides my advisors, I would also like to thank Dr. Igor Kaganovich (University of Princeton) and Prof. Khaled Hassouni (University of Paris XIII), for reviewing my thesis. Also, I would like to thank the president of my thesis committee, Dr. Thierry Belmonte (Jean Lamour Institute), as well as the other members, Prof. Eleftheria Pyrgioti (University of Patras) and Prof. Kyriakos Hizanidis (National Technical University of Athens) for accepting to participate in my viva.

I also feel indebted to Mme. Marthe Bacal (Ecole Polytechnique), for the great interest she has shown to my work and for her valuable advises during these years. The same is true for Dr. Olli Tarvainen and Mr. Janne Laulainen of the University of Jyväskylä, who so generously provided the equipment for the VUV measurements and, most importantly, their time for experiments and fruitful discussions. For sharing with me his valuable opinion on many of the problems I met, I also owe a great thanks to Prof. Nicolaos Spyrou (University of Patras).

I would also like to recognize how fortunate I was to be a member of both the High Voltage Laboratory and the Plasma-Materials-Nanostructures Research Center (LPSC). In particular, I want to recognize the high quality work realized in the mechanical workshops of both laboratories, the help of my colleagues, Alexandre Bès (Research Engineer) and Laurent Bonny (Technician), in LPSC and, of course, the help of the scientific team of the DERIRS beamline during our experiments in Synchrotron Soleil.

Furthermore, I would like to acknowledge the financial support of "Andreas Metzelopoulos Scholarships" of the University of Patras. This work would not have been possible without the three years full time scholarship, granted to me by the Institute "Andreas Metzelopoulos".

For all our interactions, whether it involved working together or simply having a drink after work, I want to thank my labmates, Kristaq Gazeli, Pierre Baële, Codrin Prahovteanu, Christos Konispoliatis, Rémi Maurau, Giorgos Peppas, Ioannis Tsiroudis, Alexandru Todoran, Long Phan Than and Thierry Grocaut.

It gives me great pleasure to acknowledge that this work would not have been possible without the help, the support and the encouragement that I received in the good company of many friends. I particularly want to thank Giorgos Athanasiou, Geoge Christidis and most importantly, Andreas Emeretlis, who has been my closest friend from the first day in the university. I wish you guys the best.

I want to express my deepest love to my father Pavlos, my mother Stamatiki and my sister Evaggelia, for their support during my entire life. Finally, a heartfelt thanks goes to my girlfriend Maria for always being with me through every single step, no matter how hard it is.

Abstract

The present PhD thesis is devoted to the experimental study of hydrogen negative ion (H^-) production in microwave-driven (2.45 GHz) multi-dipolar Electron Cyclotron Resonance (ECR) plasma sources. H^- sources are required in high-energy accelerators and more importantly in neutral beam injection systems for fusion plasma heating. Towards this directions, two sources (namely, "Prometheus I" and "ROSAE III") are designed, fabricated and studied. Both sources are driven by 2D networks of dipolar ECR elementary sources. It is proven that, negative ion formation in these ion sources is governed by the volume production mechanism, which mostly refers to the dissociative attachment of low energy electrons to vibrationally excited molecules. Contrary to the so called surface sources, volume production sources have the advantage of cesium-free operation. Extended experimental study on fundamental principles of H^- production is realized, and possible ways for potential source optimization are tested by means of: electrostatic probes, laser photodetachment, optical emission spectroscopy, both in the visible and vacuum ultra-violet spectral range and finally, vacuum-ultraviolet absorption and induced fluorescence spectroscopy using synchrotron radiation in a specially designed setup ("SCHEME"). Analytically:

The source "Prometheus I" is initially studied in detail (EEDF, H^- density, optical emission spectra etc), under a wide range of experimental conditions (e.g., pressure, power, ECR-zone location), proving its efficiency for H^- volume production, and unveiling optimum operational window and paths for obtaining higher H^- densities. The contribution of the dissociative attachment process and neutral resonant ionization to H^- production in this source, is evaluated, and the dominance of the former is finally confirmed by an equilibrium model.

Due to the importance of the ro-vibrationally excited molecules to the dissociative attachment process, the study is focused on their formation reactions. Two formation reactions are considered by adequately adapted experiments: the recombinative desorption of hydrogen atoms on the surface of various materials ("ROSAE III" and "SCHEME") and the electron impact excitation through temporary singlet states ("Prometheus I"). The study of recombinative desorption is approached in two different ways. With the source ROSAE III, the indirect impact of the process to the production of negative ions, through the formation of ro-vibrationally excited molecules, is evaluated in ECR plasmas. In the second approach, the source SCHEME is designed for the independent investigation of the recombinative desorption of unexcited atoms using synchrotron radiation based diagnostics. The formation of vibrational states through singlet excitation in the source "Prometheus I" is studied by vacuum-ultraviolet emission measurements.

A study that combined vacuum-ultraviolet emission spectroscopy, photodetachment and the characterization of electron kinetics with electrostatic probes, allowed the identification of the factors that limit negative ion production in the ECR plasma of "Prometheus I". Perspectives for overcoming these limitations are finally proposed.

Keywords

H^- sources, ECR Plasmas, photodetachment, VUV-UV spectroscopy, electrostatic probes, plasma kinetics

Résumé

Cette thèse porte sur l'étude expérimentale de la production d’ions négatifs (H^-) par des sources multi-dipolaires microondes (2.45 GHz) fonctionnant à la Résonance Cyclotron des Electrons (RCE). Les sources H^- sont nécessaires aux accélérateurs de haute énergie et surtout pour les systèmes d’injection de neutres à haute énergie pour le chauffage des plasmas de fusion. Pour cette étude, deux sources (Prometheus I et ROSAE III) ont été conçues, fabriquées et étudiées. Ces deux sources sont munies de réseaux 2D des sources multi-dipolaires. Il est prouvé que la formation des ions négatifs dans ces sources d'ions, est due à un mécanisme de production en volume : l'attachement dissociatif des électrons de faible énergie sur des molécules ro-vibrationallement excitées. Contrairement aux sources impliquant des réactions de surface, la production en volume a l’avantage de fonctionner sans césium. Une étude détaillée des principes fondamentaux de la production de H^- est réalisée, et les voies possibles pour d'optimisation sont explorées au moyen de : sondes électrostatiques, photodetachment laser, spectroscopie d'émission optique dans la région spectrale du visible et de l'ultraviolet du vide et finalement par spectroscopie d'absorption et de fluorescence induite dans la région spectral de l'ultraviolet du vide en utilisant radiation synchrotron dans un montage expérimental spécial (SCHEME). Analytiquement :

La source "Prometheus I" est d'abord étudiée en détails, dans une large gamme de conditions expérimentales (par exemple, pression, puissance, position des zones RCE). Cette étude souligne l’efficacité de production des ions H- en volume, et dévoile une fenêtre de fonctionnement optimal et des voies d'optimisation pour atteindre de plus fortes densités d'ions H^-. La contribution du processus d'attachement dissociatif et de l'ionisation résonnante des neutres, à la production H^- pour cette source ont été évaluée et la prépondérance de la première finalement confirmée par un modèle rendant compte du bilan des créations et pertes d’espèces.

En raison de l'importance des molécules ro-vibrationnallement excitées lors du processus d'attachement dissociatif, l'étude se concentre sur leurs réactions de formation. Deux réactions de formation sont étudiées par des expériences dédiées : la désorption recombinative des atomes d'hydrogène à la surface de divers matériaux ("ROSAE III" et "SCHEME") et l'excitation par impact d'électrons à travers les états singulets temporaires ("Prometheus I"). L'étude de la désorption recombinative a été appréhendée de deux façons différentes. Avec la source ROSAE III, l'impact indirect du processus pour la production d'ions négatifs, à travers la formation de molécules ro-vibrationnellement excitées, a été évaluée dans les plasmas RCE. Dans la deuxième approche, la source "SCHEME" a été conçue pour l'étude de la désorption recombinative des atomes en utilisant le rayonnement synchrotron. La formation des états vibrationnels suite à l’excitation des états singulets, dans la source "Prometheus I" a été étudiée par des mesures d'émission de l'ultraviolet du vide.

Une étude qui combine la spectroscopie d'émission de l'ultraviolet du vide, le photodétachement et la caractérisation de la cinétique des électrons par sondes électrostatiques, a permis l'identification des facteurs qui limitent la production d'ions négatifs dans le plasma RCE de "Prometheus I". Des perspectives pour surmonter ces limitations sont finalement proposées.

Mots clés

Sources H^-, plasma RCE, photodetachement, spectroscopie VUV-UV, sondes électrostatiques, cinétique des plasmas

Περίληψη

Η παρούσα διδακτορική διατριβή αφορά στην πειραματική μελέτη της παραγωγής αρνητικών ιόντων υδρογόνου (H^-) από μία πολύ-διπολική πηγή πλάσματος Κυκλοτρονικού Συντονισμού Ηλεκτρονίων (ECR) οδηγούμενη από μικροκύματα. Οι πηγές H^- είναι απαραίτητες σε επιταχυντές υψηλής ενέργειας και κυρίως σε συστήματα έγχυσης ουδετέρων σωματιδίων για τη θέρμανση του πλάσματος θερμοπυρηνικής σύντηξης. Σε αυτή την κατεύθυνση, δύο πηγές ("Προμηθέας Ι" και "ROSAE III") σχεδιάστηκαν, κατασκευάστηκαν και μελετήθηκαν. Και οι δύο πηγές οδηγούνται από δισδιάστατα δίκτυα στοιχειωδών διπολικών πηγών ECR. Αποδεδειγμένα, ο σχηματισμός αρνητικών ιόντων στις πηγές αυτές οφείλεται στον μηχανισμό παραγωγής στον όγκο του πλάσματος, ο οποίος αφορά κυρίως στην διαχωρίζουσα προσκόλληση ηλεκτρονίων χαμηλής ενέργειας σε δονητικά διεγερμένα μόρια. Σε αντίθεση με τις αποκαλούμενες πηγές επιφάνειας, οι πηγές όγκου έχουν το πλεονέκτημα της λειτουργίας χωρίς κέσιο. Εκτενής παραμετρική μελέτη των θεμελιωδών αρχών της παραγωγής αρνητικών ιόντων πραγματοποιείται και πιθανοί τρόποι βελτιστοποίησης της πηγής δοκιμάζονται μέσω: ηλεκτροστατικών καθετήρων, φωτο-απόσπασης με laser, οπτικής φασματοσκοπίας εκπομπής, τόσο στην περιοχή του ορατού όσο και στην περιοχή του υπεριώδους κενού, καθώς και φασματοσκοπία απορρόφησης και επαγόμενου φθορισμού στην περιοχή του υπεριώδους κενού χρησιμοποιώντας την ακτινοβολία συνχροτρονίου σε μία ειδικά σχεδιασμένη διάταξη ("SCHEME"). Αναλυτικά:

Η πηγή "Προμηθέας Ι" μελετάται αρχικά λεπτομερώς (EEDF, πυκνότητα H^-, φάσματα εκπομπής κλπ), σε μία ευρεία περιοχή πειραματικών συνθηκών (π.χ. πίεση, ισχύ, θέση ζωνών ECR), αποδεικνύοντας την αποδοτικότητα της στην παραγωγή αρνητικών ιόντων και αποκαλύπτοντας την περιοχή βέλτιστης λειτουργίας και τρόπους για αύξηση των πυκνοτήτων αρνητικών ιόντων. Η συνεισφορά της διαχωρίζουσας απόσπασης και του συντονισμένου ιονισμού ουδετέρων στην παραγωγή ιόντων της πηγής εκτιμάται, και η υπεροχή του πρώτου μηχανισμού τελικά αποδεικνύεται με ένα μοντέλο ισορροπίας.

Λόγω της σημασίας των περιστροφικά-δονητικά διεγερμένων μορίων για την διαχωρίζουσα απόσπαση, η μελέτη επικεντρώνεται στους μηχανισμού σχηματισμού τους. Δύο μηχανισμοί λαμβάνονται υπόψη με κατάλληλα προσαρμοσμένα πειράματα: η ανασυνδέουσα εκρόφηση ατόμων υδρογόνου στις επιφάνειες διαφόρων υλικών ("ROSAE III" και "SCHEME") και η διέγερση από κρούσεις με ηλεκτρόνια διαμέσου προσωρινών μοριακών καταστάσεων singlet ("Prometheus I"). Η μελέτη της ανασυνδέουσας εκρόφησης προσεγγίζεται με δύο τρόπους. Με την πηγή "ROSAE III", η έμμεση συνεισφορά του μηχανισμού στην παραγωγή αρνητικών ιόντων, μέσω του σχηματισμού περιστροφικά δονητικά διεγερμένων μορίων, εκτιμάται σε πλάσμα ECR. Στη δεύτερη προσέγγιση, η πηγή SCHEME σχεδιάζεται για την ανεξάρτητη μελέτη της συνεισφοράς της ανασυνδέουσας εκρόφησης μη διεγερμένων ατόμων με τη χρήση διαγνωστικών που βασίζονται στην ακτινοβολία συγχροτρονίου. Ο σχηματισμός δονητικά διεγερμένων μορίων μέσω διεγέρσεων μοριακών καταστάσεων singlet στην πηγή "Προμηθέας Ι" μελετάται με τη χρήση φασματοσκοπίας εκπομπής στην περιοχή του υπεριώδους κενού.

Μία συνδυαστική μελέτη μέσω φασματοσκοπίας εκπομπής στην περιοχή του υπεριώδους κενού, φωτο-απόσπασης και ηλεκτροστατικών καθετήρων επέτρεψε την ταυτοποίηση των παραγόντων που περιορίζουν την παραγωγή αρνητικών ιόντων στο πλάσμα ECR της πηγή "Προμηθέας Ι". Τελικά, προτείνονται πιθανές λύσεις ώστε να ξεπεραστούν αυτοί οι περιορισμοί.

Λέξεις κλειδιά

Πηγή H^-, πλάσμα κυκλοτρονικού συντονισμού ηλεκτρονίων, διαγνωστικές τεχνικές πλάσματος, φασματοσκοπία, ηλεκτροστατικοί καθετήρες, κινητική πλάσματος

Table of Contents

Chapter 1. Introduction

Abstract

This chapter serves as an introduction to the present thesis, entitled *Experimental Study of the Production of* H^- *Negative Ions by Electron Cyclotron Resonance Plasmas*. The historical development and the current state of the art of negative ion production are shortly presented. Then, the contributions of this work are summarized and the context of the thesis is outlined.

1.1 Historical development of negative ion sources

Plasmas containing negative ions have a variety of applications, including negative ion implantation [1], nanotechnology [1], micro-fabrication [2] and propulsion [3]. However, the development of hydrogen negative ion sources, is mostly motivated by two applications: negative ion injection in high-energy accelerators and neutral beam injection in fusion reactors.

Historically, accelerator applications predate fusion, dating back to the 50's [4–7]. It was initially this application that motivated negative ion source research and development worldwide [8]. In the 1970s, a new stage in the development of negative ion sources was reached by the invention of the surface sources [9] which rely on the surface production mechanism [10]. In 1977 at Ecole Polytechnique (Palaiseau, France), the presence of unexpectedly high fraction of H^- ions in low pressure hydrogen discharges was observed [11,12]. This result was confirmed in 1979 using the photodetachment technique [13], demonstrating the existence of an efficient volume production mechanism that was not considered until then. The H^- ion source research in the following decades was dedicated to the understanding of the physics involved in the surface and volume production mechanisms and to the development of negative ion sources that incorporate them [8].

During the last decades, production of electricity from fusion reactors is in the spotlight of plasma research (see the European Fusion Roadmap [14]), with the International Tokamak Experimental Reactor (ITER) being currently under construction in France. The pathway toward fusion power generation starts from today's tokamaks such as JET (Joint European Torus), passing through ITER and possibly DEMO (DEMOnstration Power Plant) to reach a commercial fusion reactor [15]. The European Fusion Roadmap calls for construction of DEMO to commence in 2030 at the point when ITER has successfully demonstrated sufficient performance. Neutral Beam Injection (NBI) systems appear highly competitive with other methods for heating full scale fusion reactors [16] and consequently became a key component for the heating and current drive system of fusion devices [17]. NBI heating power as high as 33 MW is planned for ITER [18], while 135 MW will be necessary for the steady state operation of DEMO [15].

Neutral beams can be generated from positive or negative hydrogen ion beams that are neutralized. Both positive and negative hydrogen ions can be neutralized by collisions with hydrogen molecules [19]. However, the efficiency of neutralization (Figure 1) of positive hydrogen ions declines rapidly as the ion kinetic energy exceeds 60 keV/nucleon and becomes prohibitively low above this energy. The neutralization efficiency of negative hydrogen ions in a neutralizer cell of optimum thickness remains acceptable (~60%) at higher kinetic energies and is nearly independent of the beam energy above 100 keV/nucleon. Additionally, for negative ion beams, various proposals have been made [15,17,20–24] for neutralization systems based on photodetachment, with expected neutralization efficiencies above 90%. Since high energy atomic beams are required in fusion research, the need for producing their precursors, the negative ion beams, in sufficient intensity becomes urgent.

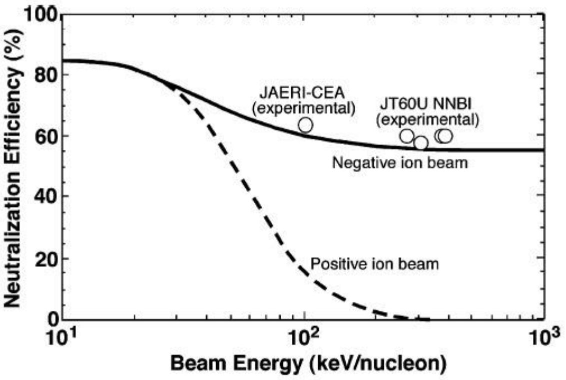

Figure 1.1 Efficiency of the neutralization process as a function of beam energy [19].

In ITER, a D^- ion current of 40 A will be accelerated up to 1 MeV before negative ions are neutralized to pass through the confinement magnetic field [8]. The development of negative ion sources and extractors for long-pulse and high-power ion beams is pursued in various fusion research institutes, e.g., IPP Garching [25] in Germany, Consorzio RFX [26] in Italy, JAEA [27,28] and NIFS [29] in Japan. Meanwhile, research on the physical aspects of negative ion sources has been the subject of experimental [30–33] and theoretical [34–39] investigations worldwide.

Even though, traditional volume production sources are filament-driven [40], there is a tendency to replace filaments with RF [17,32,33,41,42] and ECR [31,43–45] discharges. Replacing short-lived filaments, allows continuous operation, which is necessary for fusion applications, and provides a clean plasma, with no contaminants from the evaporated cathode material.

Surface production sources are met quite frequently [17,27–29,32] and usually operate with cesium. Operation with cesium, while beneficial for the production of negative ions [46], causes a lot of problems. Cesium is difficult to work with as it reacts violently with air, making its regular replacement a complicated and undesirable process for fusion devices [33]. Additionally, when working with cesium, the ion source becomes sensitive to cesium dynamics and might also contaminate the extraction system leading to sub-nominal function of even failure. Consequently, volume production, having the advantage of cesium free operation, is still investigated using RF [47–49], ECR [31,49–51], helicon [33] or even filament discharges [52,53]. The characteristics of some typical negative ion sources are presented in Table 1-1.

Table 1-1. Parameters of some typical negative ion sources

	BATMAN [54]	Camembert III [55]	MAGPIE [33]	Camembert III [56]
Source type	Surface	Volume	Volume	Volume
Discharge type	RF	Filaments	Helicon	ECR
Frequency	1 MHz	DC	13.56 MHz	2.45 GHz
Plasma power (P)	50-120 kW	0.25-4 kW	1 kW	1 kW
Working pressure (p)	2.2-4.5 mTorr	1-8 mTorr	5-10 mTorr	1-8 mTorr
Electron density (n_e)	$0.5\text{-}5\text{x}10^{11}$ cm^{-3}	$0.1\text{-}2\text{x}10^{11}$ cm^{-3}	$2\text{-}9\text{x}10^{10}$ cm^{-3}	$0.5\text{-}3\text{x}10^{10}$ cm^{-3}
Neg. ion density (n_-)	$0.1\text{-}3\text{x}10^{11}$ cm^{-3}	$0.1\text{-}2\text{x}10^{10}$ cm^{-3}	$1\text{-}6\text{x}10^{9}$ cm^{-3}	$0.3\text{-}1.5\text{x}10^{9}$ cm^{-3}

Finally, in order to use the produced negative ions in any application, there is always the need for an extraction system or extractor [57]. The first electrode of the extractor (called plasma electrode [58]) is in direct contact with the plasma and has an important effect on operation of the source [58–60]. On the other hand the design of an efficient extraction system should take account of the parameters of the plasma in its vicinity [61]. Overall, the implementation of an extraction system is a complex process that, nowadays, requires the use of sophisticated computational tools [62].

1.2 Thesis contributions

The main reactions that create H^- in both volume and surface sources are identified and sufficiently understood [8]. However, volume production, which is relevant to this work, is extremely sensitive to: a) electron kinetics, b) the internal energy of the hydrogen molecules [63] and c) the specific source design (e.g. geometrical characteristics of the chamber [64], plasma electrode design [58] or magnetic field configuration [65,66]). This dependency, makes volume H^- production an active topic of research.

The use of the ECR sources related to this work [67] for the production of hydrogen negative ions has been investigated for more than a decade [44]. The design, implementation and detailed study of new H^- sources based on this ECR heating scheme adds to the understanding of the underlying physics. The main contributions of this thesis to this direction refer to:

- Design and fabrication of a new ECR negative ion source ("Prometheus I") that is installed in the High Voltage Laboratory of the University of Patras (Greece). Prometheus I is driven by a network of five independent dipolar ECR sources [67] facilitating the potential scaling-up of the system (Article 2[1]).
- Development of the necessary diagnostic tools for the experimental investigation of negative ion production. These include:
    - Electrostatic probe measurements based on a) a custom-made system for the automated acquisition of Langmuir probe curves with high accuracy and resolution (Article 3 and Conference 4) and b) a program developed for the treatment of the acquired data the determination of electronic parameters (density, temperature, EEDF etc.).
    - Photodetachment measurements for the determination of negative ion densities. The photodetachment configuration was installed and calibrated to ensure the validity of the technique.
- Characterization of the H^- source Prometheus I, for different configurations and for a wide range of parameters (pressure and power).
    - Determination of the spatial evolution of plasma parameters
    - Study of H^- production that revealed optimum operating conditions (Conference 4).
    - Determination of the degree of dissociation, with optical emission spectroscopy.

---

[1] Reference to author's peer-reviewed articles and conference papers listed in page 104.

- Investigation of negative ion formation processes
    - Assessment of the importance of neutral resonant ionization [68] as an additional negative ion production process in the source Prometheus I (Article 4).
    - Confirmation of the main negative ion production channel in Prometheus I by comparing the measured negative ion density with the equilibrium density calculated on the basis of the widely accepted volume production mechanism (dissociative attachment of electrons to vibrationally excited molecules) (Article 4).
- Investigation of the formation of vibrational states
    - Investigation of the impact of recombinative desorption on the negative ion density of ECR plasmas, conducted in the Plasma-Materials-Nanostructures Research Center (CRPMN) of the Laboratory of Subatomic Physics and Cosmology (LPSC) in Grenoble (France) using the source ROSAE III which is specially designed for this purpose (Conference 7).
    - Development of the framework for diagnostics based on vacuum-ultraviolet synchrotron radiation for the determination of atomic hydrogen densities and ro-vibrational distributions of hydrogen molecules. This project is realized on the DESIRS beamline of Synchrotron Soleil (Saint-Aubin, France). (Conference 6 and 8).
    - Study of the volume production of vibrationally excited molecules through the decay of singlet states excited by high energy electron impact processes in the source Prometheus I (Article 5).
    - Determination of the limiting factors of negative ion production in the source Prometheus I and proposition of ways to overcome these limitations (Article 5).
- Investigation of the photoelectric effect contribution to the electron density of the source Prometheus I (Annex, Conference 9).

As mentioned earlier, the final part of any negative ion source is the extraction system. However, this work, being the first effort of characterization of the negative ion source Prometheus I, does not include the implementation of such a system. Surely, designing an extractor should be among the perspectives related to this source, once its operation has been understood and optimized.

1.3 Thesis Outline

Following the introduction of this first chapter, **Chapter 2** deals with the theoretical background of negative ion production and specifically with three key topics. Namely, the negative ion production and loss mechanisms, the reactions that determine the vibrational distribution of the ground state molecules and the principles of electron heating by the multi-dipolar ECR sources. The purpose of this chapter is to facilitate the interpretation of the results that will be presented later in Chapter 4.

Chapter 3 which follows, describes the three experimental setups that are used. Prometheus I which is the principal ECR plasma source used in this study, is presented in detail along with all the installed diagnostic techniques (electrostatic probes, photodetachment as well as visible and vacuum ultraviolet emission spectroscopy). ROSAE III is specially designed to study the effect of the chamber wall material on the production of negative ions in ECR plasmas. Diagnostic techniques used with ROSAE III are probe measurements, photodetachment and optical emission spectroscopy. Finally, the source SCHEME, which is adapted in the beamline DESIRS of Synchrotron Soleil, is used for vacuum-ultraviolet absorption and induced fluorescence measurements. Its purpose is to independently study the recombinative desorption mechanism (see Section 2.2.2) on various materials.

Results are presented and discussed in **Chapter 4**. Firstly, the source is characterized for and extended range of parameters, by means of electrostatic probe, laser photodetachment and optical emission spectroscopy, for three different configurations. Then, the importance of a recently proposed H^- production mechanism is examined. However, the dominance of dissociative attachment, which is the widely accepted mechanism, is confirmed. After this confirmation, the study is focused on the formation of vibrational states via two different channels. The first formation process, refers to the recombinative desorption of atoms on various materials and is investigated with two specially designed sources. The second formation process refers to the radiative decay of singlet states, excited by collisions of ground state molecules with energetic electrons and is studied in Prometheus I. By correlating negative ion production with the formation of vibrational states, the factors that limit negative ion production in Prometheus I are identified and discussed.

Finally, **Chapter 5**, which is the last chapter, summarizes the important conclusions of this work. A series of photoelectron effect measurements in the source Prometheus I, are briefly presented in the Annex.

Chapter 2. Theoretical Background

Abstract

This chapter is a brief presentation of the theoretical background related to this work. It is separated into three parts, related to the volume production of H^- in ECR plasma sources. The first part refers to the processes that are directly involved in the production and destruction of negative ions. The second treats the crucial subject of vibrational excitation of hydrogen molecules. In the third part, the employed electron heating scheme is presented.

2.1 Production and destruction of hydrogen negative ions

The steady state density of negative ions in a hydrogen discharge is determined by the equilibrium between formation and loss processes. The evaluation of the importance of these processes in the studied plasmas, is a major part of the present work. This section refers to their analytical presentation.

2.1.1 Production of negative ions

Negative ion formation takes place in the plasma volume (volume production) and on the surfaces facing the plasma (surface production). In volume sources, H^- ion production is attributed to collisional processes of electrons with molecules and molecular ions in the bulk of the plasma [69], with dissociative attachment (DA) of electrons to hydrogen molecules being the most important. On the other hand, on surface sources, H^- ions are formed by the direct electron transfer from the solid material facing the plasma to hydrogen atoms [8].

Volume production of H^-

Initial attempts for the development of hydrogen negative ion sources lacked the understanding of the involved fundamental processes [70]. In 1977, Nicolopoulou et al [11,12] calculated the equilibrium density of hydrogen negative ions in a low pressure hydrogen plasma by taking the known production and destruction processes into account. At the time, the known production processes were dissociative electron attachment (DA) to hydrogen molecules in their ground state and dissociative recombination of molecular positive ions [11]. The calculated negative ion density ($\sim 10^7$ cm^{-3}) was two orders of magnitude lower than the density measured with electrostatic probes ($\sim 10^9$ cm^{-3}) [11]. This discrepancy was confirmed, in hydrogen and deuterium plasmas, by Bacal and Hamilton in 1979 [13] using the photodetachment diagnostic technique for the measurement of the H^- ion density. Clearly, the considered formation mechanisms of negative ions were not sufficient to explain their actual density [8].

Meanwhile, progress had been made in the theory of DA which was approached with a resonance model [71–73]. In this theory, the incident electron is temporarily captured in the neighborhood of the molecule, forming a temporary molecular negative ion. The decay of this ion can lead to DA and the formation of a negative ion and a neutral atom:

$$H_2 + e \rightarrow H_2^- \rightarrow H^- + H \qquad (2.1)$$

or to auto-detachment with the possibility of changing the vibrational state of the molecule (eV process):

$$H_2(v) + e \rightarrow H_2^- \rightarrow H_2(v + \Delta v) + e \qquad (2.2)$$

Theoretical [74,75] and experimental [76] works have shown that, when the molecule is ro-vibrationally excited, the DA cross section increases considerably (up to 5 orders of magnitude) and, at the same time, the energy threshold of the process is reduced. The vibrational and rotational state dependence of the cross section is presented in Figure 2.1.

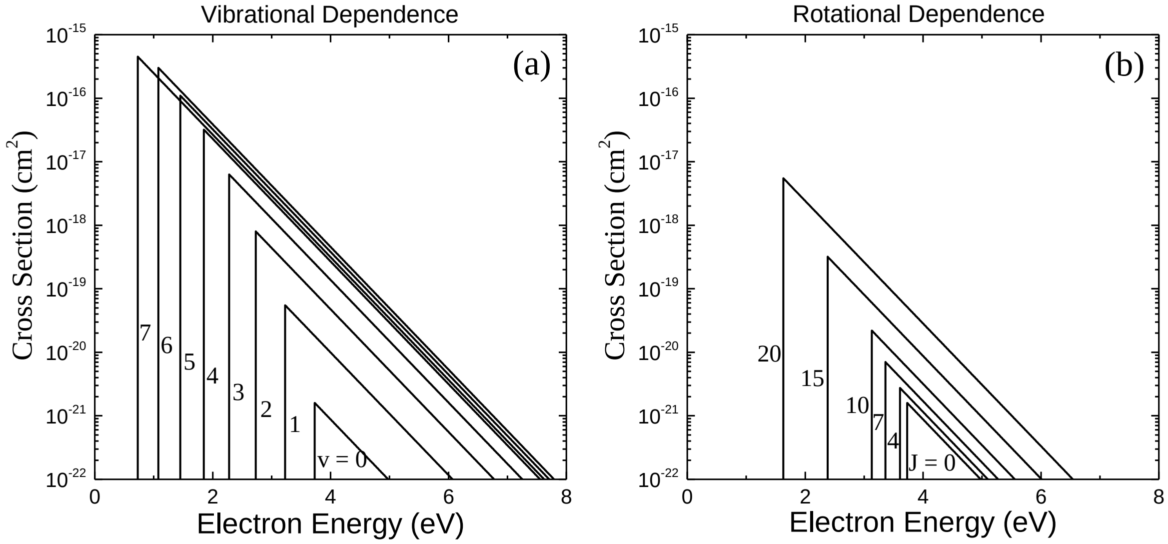

Figure 2.1. Vibrational (a) and rotational (b) state dependence of the DA cross section. The cross section has been approximated by a single exponential function as proposed in [77,78]. The values of the energy thresholds and the cross section peaks are from [75].

In these initial results [76] vibrational excitation appeared to be more important than the rotational excitation in enhancing the DA cross section. To explain this, the underlying mechanism that enhances dissociative attachment cross section to high ro-vibrational states must be discussed. The basic reason for the enhancement of the dissociative attachment cross section is an increment in the range of internuclear separations over which the electron capture can occur when the molecule is internally excited [63]. This range is increased due to an increased vibrational amplitude for vibrational excitation or due to centrifugal stretching for rotational excitation. It is interesting to note that the attachment rate appears to depend on the total internal energy and not so much on the specific partitioning between vibrational and rotational modes [63]. Due to the greater energy separation of vibrational levels rotational excitation might play an important role only if the molecule is vibrationally unexcited. The rate coefficient of DA (for an electronic temperature of 1 eV) for some of the 294 ro-vibrational levels of the H_2 ground state are presented in Figure 2.2 [63]. The maximum rate coefficient is about 10^{-8} cm^{3}s^{-1} and corresponds to an internal energy of 3.994 eV. Above this energy the attachment process becomes exoergic. Further increase in the internal energy, does not have any beneficial effect in the DA rate coefficient. These results were later independently recalculated and confirmed [79].

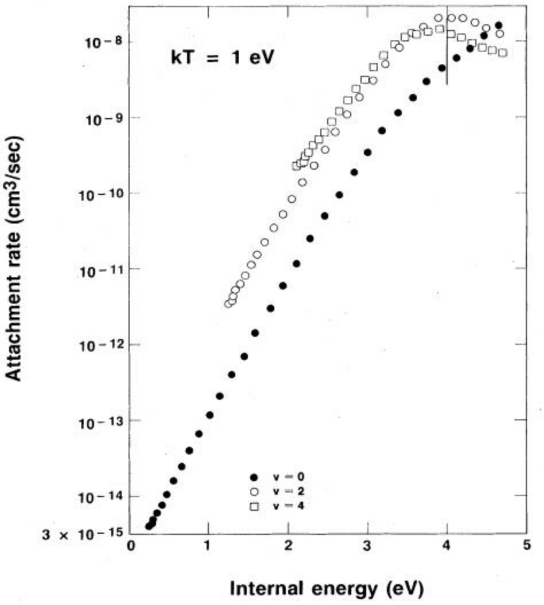

Figure 2.2. Rate coefficients of dissociative electron attachment to all possible rotational levels for v = 0, 2 and 4 for electron temperature of 1 eV. The vertical line at 3.994 eV defines the internal energy above which the attachment process becomes exoergic. [63]

An improved nonlocal resonance model proposed by Čizek et al [80] was used by Horacek et al [81] for the calculation of cross sections of electron DA on molecular hydrogen by the impact of low-energy electrons. This model also shows that the magnitude of the DA cross section in the low-energy range increases rapidly with increasing vibrational quantum number of the target molecule; the DA increases by nearly five orders of magnitude from v = 0 to v = 8-9. However, the theory of Horacek et al [81] leads to a new view on the effect of rotational excitation on the DA cross section. According to him, excitation to high rotational levels ($J \geq 24$), appears to be more efficient in increasing the DA cross section compared with vibrational excitation. The sensitivity of the DA rate on the rotational excitation of the molecules, observed under certain conditions [82], may be explained by this theory.

In low pressure molecular plasmas, the distribution of energy takes place through a complex collision physics, where the primary role is played by electron molecule collisions. These collisions efficiently populate the vibrational spectrum through optically allowed singlet excitations (see Section 2.2) [39]. Therefore, in the plasmas under study, vibrational kinetics play the most prominent role.

Due to the sensitivity of DA on the internal energy of molecules, other mechanisms of negative ion production have been proposed as well. For example, DA to the metastable $H_2\left(c^3\Pi_u\right)$ [83] and to molecular Rydberg states [84,85] have also been considered. However, while the importance of these additional mechanisms should definitely be discussed, the dominance of DA to ground state ro-vibrationally excited molecules seems unquestionable when considering volume production. An important diagnostic effort by Mosbach [30] allowed the comparison of the H^- density measured by laser induced photodetachment to that calculated from the spectrum of ro-vibrationally excited levels of hydrogen molecules measured by Laser-Induced Fluorescence (LIF). The calculated density is in good agreement with H^- density as shown in Figure 2.3, proving that DA to vibrationally excited ground state molecules is the main production channel of hydrogen negative ions.

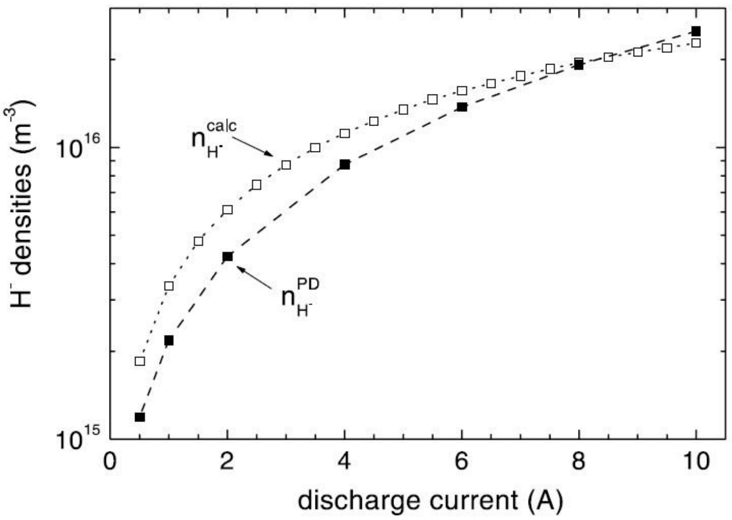

Figure 2.3. Dependence of the absolute H^- densities on the discharge currents of a filament discharge (filament bias is 100 V) in pure hydrogen (11.2 mTorr). Full squares are H^- densities measured with laser induced photodetachment, while open squares are H^- densities calculated from measured VDFs of the ground state molecule [30].

So far the dependence of DA on the internal state of the molecule has been discussed. However, there is another important factor that affects DA rate, which is the temperature of the electrons. This becomes obvious from the DA cross section presented in Figure 2.1, which is reduced quite dramatically (exponentially) as a function of electron energy. This behavior is related to the process of electron capture by the molecule, which leads to the formation of the aforementioned temporary negative ion. In order to form this temporary ion, the incident electron is predominantly captured at an internuclear separation where the difference between the potential curves of H_2 and H_2^- is equal to the electron energy [63]. For high energy electrons, this happens at smaller internuclear separations, where the probability of auto-detachment is much higher. Electrons with energies close to the threshold of the cross section are captured at higher internuclear separations, where the probability of DA is relatively large.

To sum up the theory presented so far negative ion production demands molecules excited to high vibrational levels and low temperature electrons. In Figure 2.4, a graphical representation of the production scheme considered for this work is attempted. The vibrationally resolved total DA cross sections borrowed from [78] are presented in (Figure 2.4a). The Maxwellian EEDF presented in the same graph is reconstructed from typical temperature values measured in the plasmas under study (see Chapter 4). Using these data, the rate coefficients of DA are calculated. The rate coefficient energy density of Figure 2.4b is presented to show how higher vibrational levels "claim" a bigger part of the electron population to form negative ions. The total rate coefficients are presented in Figure 2.4c. Their greatest values are observed for the vibrational levels 8 and 9.

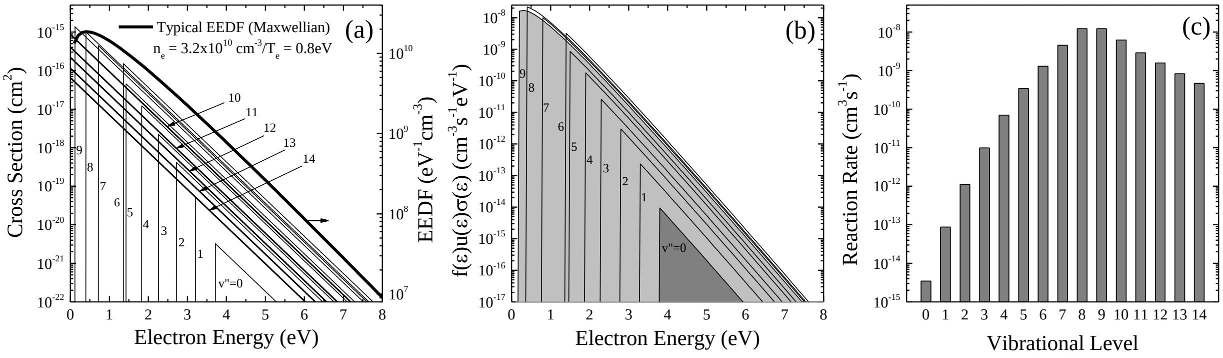

Figure 2.4. Vibrationally resolved production scheme based on DA. (a) Vibrationally resolved cross sections of DA [78] and a typical Maxwellian distribution (b) Rate coefficient energy distribution for production from different vibrational levels (data from (a)). (c) Rate coefficients for each vibrational level for the EEDF of (a).

The reaction rate for each vibrational level as a function of electron temperature is presented in Figure 2.4a. Here two different tendencies are observed. For high vibrational levels (v"≥9), the reaction rate decreases monotonically, while for lower levels (v"<6) it increases and saturates at about 1 eV. Only high vibrational levels require electron temperatures that are as low as possible. For lower vibrational levels, a certain electron energy is required in order to have a sufficient portion of electrons above the DA threshold.

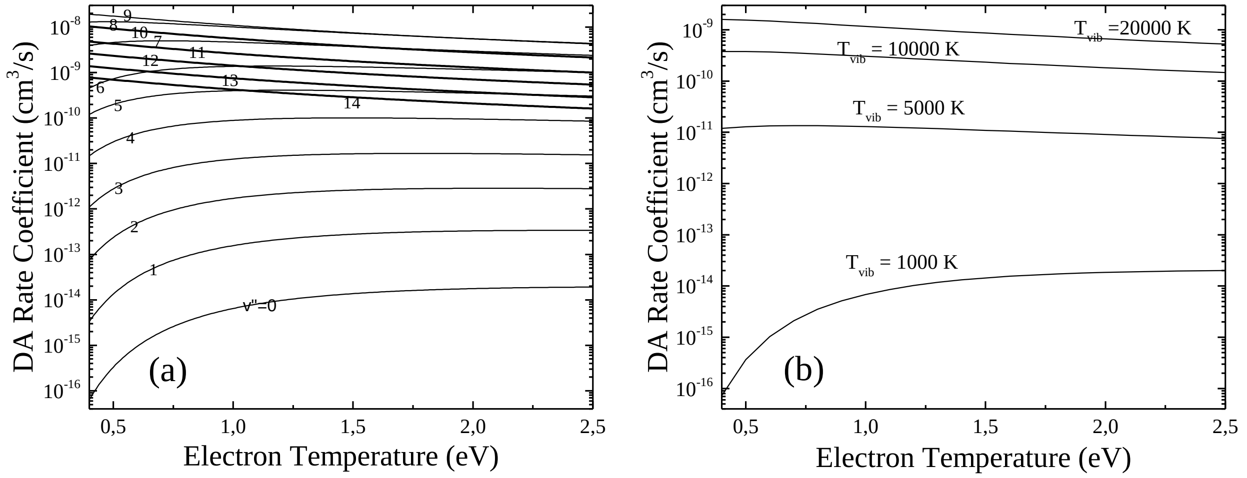

Figure 2.5. Electron temperature dependence of DA rate coefficient (a) Rate coefficients for each vibrational level as a function of electron temperature. (b) Total rate coefficients for all vibrational levels of the ground state molecules as a function of electron temperature (assuming a Maxwellian vibrational distribution of various temperatures).

Assuming Maxwellian vibrational distribution, the total rate coefficients of DA as a function of electron temperature, are presented in Figure 2.5b. This calculation quantitatively demonstrates what was previously qualitatively understood: for a high formation rate of negative ions, the combination of a vibrationally excited plasma with the presence of sufficiently cold electrons is required. An important observation is that the vibrational temperature plays a more important role than the electron temperature. Evidently, high vibrational excitation rates are highly desirable for negative ions sources. The main vibrational excitation processes are presented in Section 2.2.

The theory presented so far, refers only to electron impact processes to ground state molecules. Indeed, for molecular low-pressure low-temperature plasmas, electron impact processes represent the majority of binary collisions, while ground state molecules represent the majority heavy species [30]. However, in plasmas with higher degree of dissociation, the frequency of atom-atom collisions increases and might have some effect. Dissociated plasmas, are optically dense to Lyman-α emission [86], which might lead to an over population of H(n=2) atoms. Recently, the neutral resonant ionization of excited atoms H(n=2) has also been proposed as a possible production route [68,87] of negative ions. The physical path for the creation of stable negative ions is presented on potential energy plot of the hydrogen molecule in Figure 2.6.

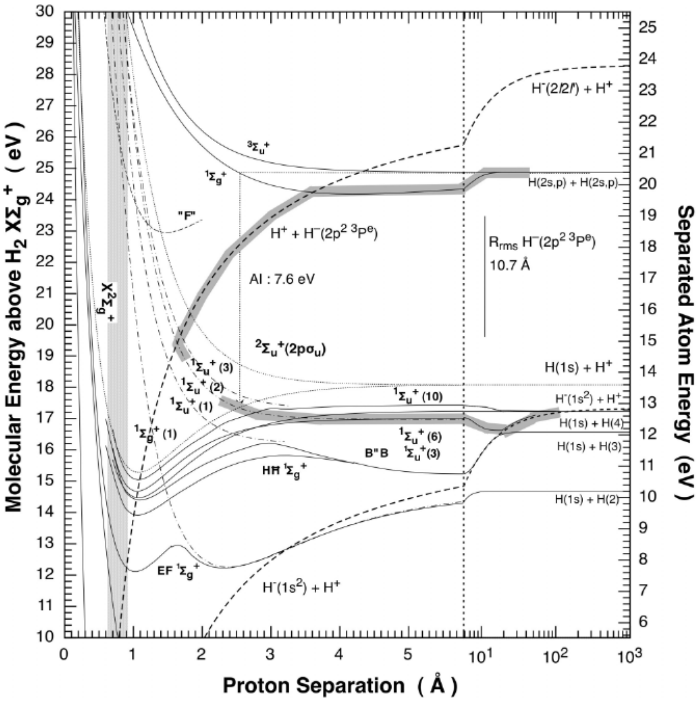

Figure 2.6. Potential energy plot of the hydrogen molecule [87]. The shaded line corresponds to the hypothesized path of H^- formation.

In Figure 2.6, both the 2s and the 2p states of the first excited state of hydrogen are mentioned. However, the 2p state has a lifetime in the order of ~ns [88] while the 2s state has a natural lifetime of 200 ms [87], which is actually shortened by collisional quenching [88]. If any contribution of this mechanism to negative ion production is to be expected, the 2s state needs to be considerably populated.

It is noteworthy that this mechanism also predicts the existence of the second bound state of the hydrogen negative ion (doubly excited $H^-\left(2p^2\ ^3P^e\right)$) [89]. This negative ion is calculated to have an electron affinity of only 9.7 meV and a lifetime of a few ns [87]. Its effects are seen in astrophysical settings but it hasn't been observed in laboratory plasmas [87]. The extrapolation of electron capture cross sections from collisions of excited H atoms, predicts a cross section for the doubly excited negative ion which is greater than 10^{-11} cm^2 for the 9.7 meV electron deficit [87]. Then, the process follows the path through an excited molecular state, to finally reach the formation of an ion pair. The probability of the entire process and the contribution of this mechanism to production of negative ions is not determined yet. To this direction, additional theoretical and experimental work is required.

Surface production H^-

Emission of H^- ions from solid surfaces was observed as early as 1931 [90]. Since the report of a high density H^- beam being extracted from a surface plasma source [91], many theoretical and experimental works have been realized in order to explain H^- surface production. Negative surface ionization of hydrogen is the single step process of direct electron transfer from solid material to a hydrogen atom leaving the surface [8]. The electron affinity of hydrogen is only 0.754 eV, while surface work functions of common metals used in plasma sources (stainless steel, copper, aluminum etc.) exceed 4 eV. Under these conditions direct negative surface ionization is not an efficient process, making it necessary to lower the surface work function, which is mostly achieved by alkali or alkaline earth metal adsorption. By doing so, the hydrogen affinity level goes below the work function at a small distance from the metal surface and the production of H^- is greatly enhanced [46]. On the basis of this production mechanism, many sources have been developed for fusion and for accelerator applications [8].

While operation with cesium is quite beneficial for the negative ion yield, it also causes many problems. Plasma heating by negative ion based neutral beam injection demands large current H^- ion beam which requires a considerable Cs consumption (0.16 g/hour predicted for ITER [18]). Replacing and managing this difficult to work with material is certainly an undesirable process. Another problem is the Cs contamination of the downstream accelerator that could cause high voltage holding problems [8]. Furthermore, the source is extremely sensitive to Cs dynamics making more difficult the stable operation of the source [33]. An additional challenge for Cs delivery system is the efficient coverage of the converter surface [8]. Attempts made to reduce Cs leakage include the use of porous materials for Cs supply [92]. Research has also been realized for cesium substitutes like barium (Ba) [93], carbon (C) [94,95], highly oriented pyrolytic graphite (HOPG) and boron doped diamond (BDD) [96].

Cesium seeding has also been used for the enhancement of negative ion production in volume sources. Direct surface production is not the only reason for this change in performance. Lowering the work function of the chamber walls may also affect secondary electron emission [97,98] and absorption of species [99] and have an indirect but still important impact on the production and destruction on negative ions.

In the frame of this work, plasmas are generated in pure hydrogen. Furthermore, the chamber walls are made from conventional materials (stainless steel, copper, Pyrex etc.) with relatively high work functions. Consequently, the direct surface production process is completely disregarded. On the other hand, the surface of the materials might have an important indirect impact. The surface recombination of atoms, might lead to the formation of ro-vibrationally excited molecules (see Section 2.2.2) which may enhance the production of negative ions through the volume process.

2.1.2 Destruction of negative ions

The small electron affinity of hydrogen negative ions (0.75 eV [69]) makes them quite fragile. The various H^- loss mechanisms can be divided into three categories: mutual neutralization in collisions with positive ions, electron detachment in collisions with neutral particles and electron detachment in collisions with electrons. A list of some important loss mechanisms is given in Table 2-1.

Table 2-1. Negative ion loss processes. T refers to an effective temperature determined by the translational temperature of the reactants [36].

Reaction	**Reaction Rate**	Reference
$H^- + H^+ \rightarrow H + H(n=2)$ (2.3)	$9.1\times10^{-11}(T/300)^{0.83}$	[78,100]
$H^- + H^+ \rightarrow H + H(n=3)$ (2.4)	$1.28\times10^{-7}(300/T)^{1/2}$	[101]
$H^- + H^+ \rightarrow H_2^+ + e$ (2.5)		[78]
$H^- + H_2^+ \rightarrow H_2 + H$ (2.6)	$2\times10^{-7}(300/T)^{1/2}$	[100]
$H^- + H_2^+ \rightarrow 3H$ (2.7)	$8.29\times10^{-7}(300/T)^{1/2}$	[101]
$H^- + H_2^+ \rightarrow H_3^+ + e$ (2.8)	$\max\sigma \sim 10^{-15}\,cm^2$	[78]
$H^- + H_3^+ \rightarrow H_2 + 2H$ (2.9)		[78]
$H^- + H_3^+ \rightarrow H_2 + H_2$ (2.10)	$2\times10^{-7}(300/T)^{1/2}$	[78]
$H^- + H_3^+ \rightarrow 4H$ (2.11)	$8.29\times10^{-7}(300/T)^{1/2}$	[101]
$H^- + H_5^+ \rightarrow 3H_2$ (2.12)	$2\times10^{-7}(300/T)^{1/2}$	[78]
$H^- + H \rightarrow H_2 + e$ (2.13)	Figure 2.7b	[78]
$H^- + H \rightarrow H + H + e$ (2.14)	Figure 2.7b	[78]
$H^- + H_2 \rightarrow H_2 + H + e$ (2.15)	~$1.3\text{x}10^{-9}$ cm^{3}s^{-1} and Figure 2.7b	[78,100]
$H^- + e \rightarrow H + e + e$ (2.16)	Figure 2.7c	[78]

In low temperature plasmas where heavy species translational temperatures are typically in the order of ~0.1 eV, mutual neutralization (MN) by electron capture has quite high cross sections. For energies below 0.1 eV the cross section of MN from atomic positive ions (H^+) reaches values above 10^{-10} cm^2, while those of molecular positive (H_2^+, H_3^+) ions are about one order of magnitude higher [78,102]. The cross section of reactions (2.3) and (2.4) are presented in Figure 2.7a. The rate coefficient of all the important MN reactions (Reactions (2.4), (2.7) and (2.11)) are described by the $T^{-1/2}$ law.

In the low energy range, negative ion losses by neutrals are dominated by associative detachment (AD, Reaction (2.13), Figure 2.7b) [78]. Non-associative detachment by atoms and molecules becomes important for higher energies. Electron detachment depends on electron energy, but its cross section does not exceed $4\text{x}10^{-15}$ cm^2. In order to avoid negative ion losses due to electron detachment, many negative ion sources feature a magnetic filter [65,66]. Simply put, a magnetic filter is a magnetic field configuration that separates the source in two regions (tandem sources [103]). The first one is the driver region which is characterized by an intense presence of hot electrons that promote ionization and excitation. The second is the negative ion production region, where the low energy electrons and vibrationally excited molecules, not being affected by the magnetic field, may diffuse and create negative ions through DA.

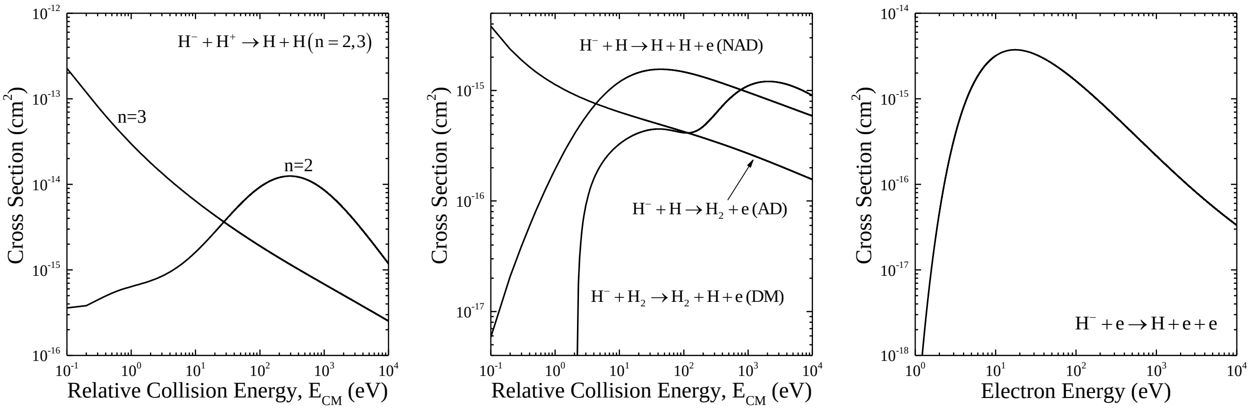

Figure 2.7. Cross sections of indicative negative ion loss mechanisms. (a) Mutual neutralization with atomic positive ions. (b) Negative ion losses in collisions with neutrals, i.e. associative detachment (AD), non-associative detachment (NAD) and detachment by molecules (DM). (c) Electron detachment (ED)

Evidently, mutual neutralization dominates negative ion losses in low temperature plasmas. Negative ion losses also include diffusion to the chamber wall which is characterized by a lifetime (τ_-). Loss frequency is inversely proportional to this lifetime and is equal to [55]:

$$\frac{1}{\tau_-}=\frac{1}{4}\frac{S}{V}u_-^{th}\exp\left(-\frac{eV_p}{kT_-}\right) \qquad (2.17)$$

Where S is the total wall surface, V is the source volume, u_-^{th} is the thermal velocity of negative ions, V_p the plasma potential and T_- the negative ion temperature. While in volume sources, the negative ion temperature is considered to be in the range of 0.1 eV [36], some higher temperatures (up to 2 eV) have been reported [104]. In any case, even plasma potentials of some volts can confine negative ions quite efficiently and H^- diffusion losses to the walls may be ignored.

2.2 Vibrational kinetics

The Vibrational Distribution Function (VDF) of ground state molecules is of fundamental importance for all molecular plasmas [39]. In low-temperature low-pressure molecular plasmas vibrational kinetics together with dissociation/association phenomena play a prominent role in the redistribution of the injected energy [105]. Furthermore, since H_2 has no electric dipole moment, vibrationally excited H_2 molecules have long lifetimes [106] which allows them to constitute a great portion of the gas particles. The importance of the VDF in the production of negative ions has been established in the previous section. This section briefly presents the main excitation and de-activation routes for vibrational states.

2.2.1 Volume processes involving vibrational levels

Direct vibrational excitation of homonuclear molecules like H_2 is an inefficient process. Most mechanisms that take place in the volume of plasmas, involve indirect excitation through a temporary state [39]. This might be the result of an enormous number of collision processes dominated by electron-molecule collisions [39]. On the other hand, in low pressure plasmas, the increased mean free path of particles enhances the importance of wall processes. Depending on the wall material and its condition, wall processes, like recombinative desorption, may have and important contribution to the enrichment of the vibrational spectrum [39].

A possible vibrational excitation process involves the capture of an electron and the formation of a temporary molecular negative ion (see Section 2.1.1). When the DA route is not followed, the electron is auto-detached and the neutral molecule may end up in a different vibrational level (eV excitation, Reaction (2.2)). However, the most probable change in vibrational state is ±1 which means that: a) a large number of collision is required for the population of high levels [107] and b) the eV process might also have a considerable contribution in the deactivation of vibrationally excited molecules [30].

An effective source of highly vibrationally excited molecules, is the radiative decay from higher electronic states excited by collisions of ground state molecules with energetic electrons (EV excitation):

$$\mathrm{H_2}\left(\mathrm{X}^1\Sigma_g^+,\mathrm{v_i}\right)+\mathrm{e}\rightarrow \mathrm{H_2^*}\left(\mathrm{B}^1\Sigma_u,\mathrm{C}^1\Pi_u...\right)+\mathrm{e}\rightarrow \mathrm{H_2}\left(\mathrm{X}^1\Sigma_g^+,\mathrm{v_f}\right)+\mathrm{e}+\mathrm{hv} \qquad (2.18)$$

Optically allowed singlet excitations will lead to spontaneous radiative decay in a direct or a successive manner. The final vibrational level of the ground state will not necessarily be the same as the initial one. $\mathrm{B}^1\Sigma_u^+$ and $\mathrm{C}^1\Pi_u$ are the singlet states of the first excited electronic state (n=2) from which the decay to the electronic ground state is optically allowed [108]. Being in the first electronic state, the excitation to these singlets have cross sections that exceed those of higher states [78], making them the main contributor of vibrational excitation. For a complete account of the EV excitation, one should include vibrational population from: a) the singlets in higher electronic states from which the transition to the ground state is optically allowed ($\mathrm{B'}^1\Sigma_u^+$ and $\mathrm{D}^1\Pi_u$ for n=3 and perhaps $\mathrm{B''}\overline{\mathrm{B}}^1\Sigma_u^+$ and $\mathrm{D'}^1\Pi_u$ for n=4) and b) higher singlets through successive decay. The contribution of those higher singlet states is estimated to be about 25% [109]. The probabilities for populating a ground state vibrational level through the $\mathrm{B}^1\Sigma_u^+$ and $\mathrm{C}^1\Pi_u$ singlets as a function of the initial vibrational level is calculated by Hiskes [109] and presented in Figure 2.8.

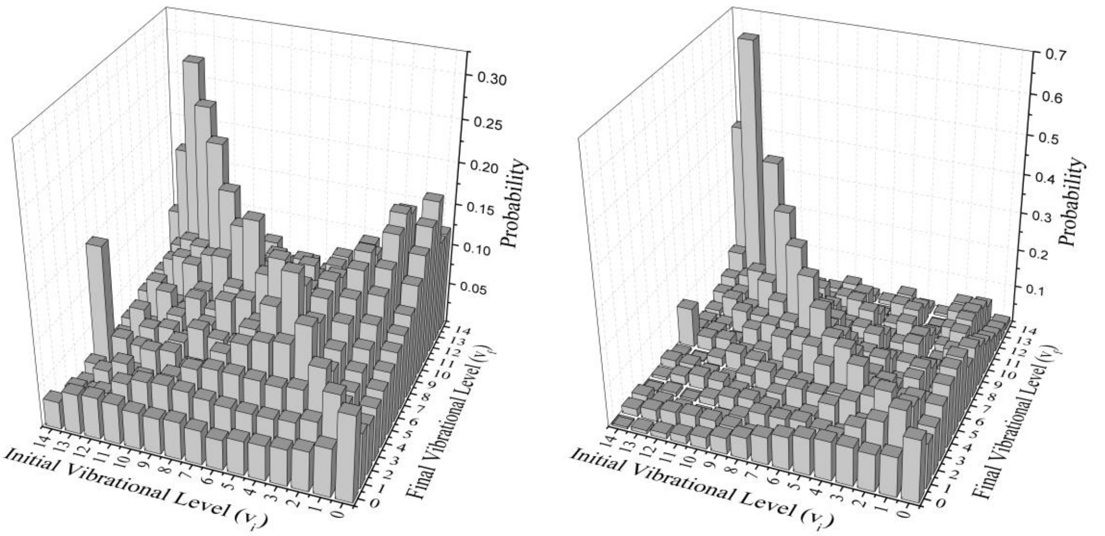

$\mathrm{e}+\mathrm{H_2}\left(\mathrm{X}^1\Sigma_g^+,\mathrm{v_i}\right)\rightarrow \mathrm{e}+\mathrm{H_2^*}\left(\mathrm{B}^1\Sigma_u^+\right)\rightarrow \mathrm{e}+\mathrm{H_2}\left(\mathrm{X}^1\Sigma_g^+,\mathrm{v_f}\right)+\mathrm{hv}$ $\mathrm{e}+\mathrm{H_2}\left(\mathrm{X}^1\Sigma_g^+,\mathrm{v_i}\right)\rightarrow \mathrm{e}+\mathrm{H_2^*}\left(\mathrm{C}^1\Pi_u\right)\rightarrow \mathrm{e}+\mathrm{H_2}\left(\mathrm{X}^1\Sigma_g^+,\mathrm{v_f}\right)+\mathrm{hv}$

Figure 2.8. Probabilities for populating final vibrational levels (v_f) via excitation from initial vibrational levels (v_i) through the $\mathrm{B}^1\Sigma_u^+$ (left) and $\mathrm{C}^1\Pi_u$ (right) singlet.

Figure 2.8 allows for some discussion. The first observation is the enhanced probabilities on the diagonal of this graphs, indicating that it is most probable that the singlets will decay to the vibrational level they were excited from. However, the probability on the diagonal also increases as a function of the vibrational state. This behavior explains the accumulation of higher vibrational states, and is partially responsible for the non-equilibrium vibrational kinetics of low-pressure low-temperature plasmas [110] in which typically the VDF exceeds the Maxwellian for higher vibrational states. An additional observation is that the low vibrational levels have a bigger chance of being excited to high vibrational levels through the $B^1\Sigma_u^+$ singlet than through the $C^1\Pi_u$ singlet (for the $B^1\Sigma_u^+$ singlet, the probabilities on the right side of the diagonal are considerably higher and increase as a function of the final vibrational number).

Collision with electrons can also deactivate vibrationally excited molecules in various ways with the obvious one, being DA. Indeed DA, regardless of being the main negative ion production process, from the point of view of vibrational kinetics, is considered a loss mechanism. Other deactivation processes that involve electrons are electron impact ionization and dissociation [36].

Vibrational states may also be influenced by heavy body collisions. Vibrational-vibrational energy exchange between two molecules redistributes the energy among vibrational levels. Most probable changes in vibrational number are ±1. The rate coefficient of this process [100] increases as a function of the vibrational level of both reactants/products. This indicates that this mechanism mostly effects the population distribution of high vibrational levels. Collisions with neutrals might also lead to vibrational-translational energy exchange. This process involves collisions with molecules (VT) [100] and collisions with atoms (Vt) [111]. Positive ions may also destroy vibrationally excited molecules through ion conversion [112]. If vibrationally excited molecules are not deactivated or destroyed by one of the above mentioned processes, they will be finally deactivated on the chamber walls [111,113].

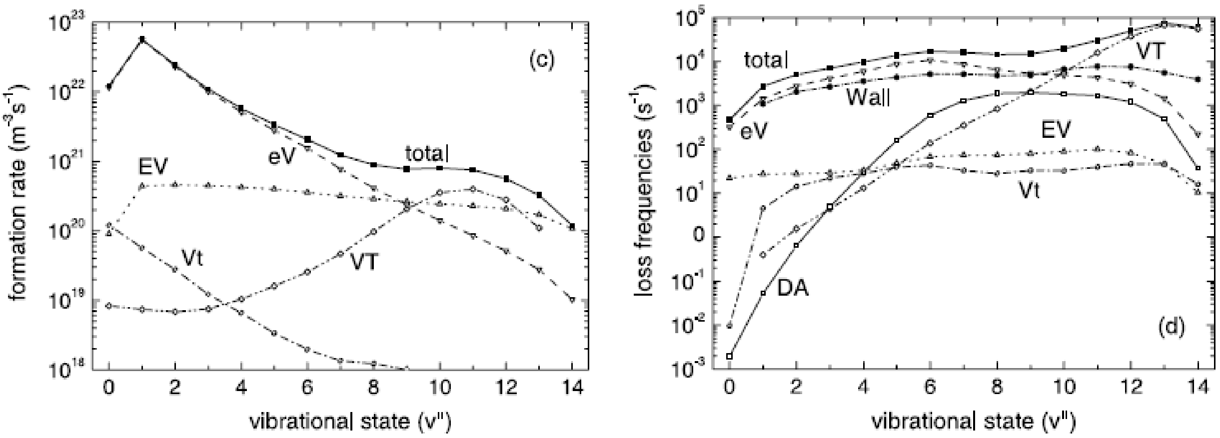

Figure 2.9. Formation rate and loss frequency of vibrational states for a filament driven magnetic multi-pole discharge [30]. The abbreviations are explained in the text. The Wall losses refer to vibrational relaxation on the chamber walls.

Figure 2.9 presents the formation rates and loss frequencies as they were calculated for a magnetic multi-pole H_2 discharge. An important observation concerns the VT and eV mechanisms. The first impression might be that these processes contribute considerably to the formation rate of high vibrational states. However, this is quite misleading, since they are also responsible for many of the losses. In fact, what is actually happening, is that they "steal" vibrational energy from high vibrational states and turn them into lower states. The "stolen" energy is released as kinetic energy of the molecule or the electron (super-elastic collision). On the other hand, the EV process is connected with a considerable formation rate and a very low loss frequency. Consequently, is safe to assume that the EV process is mainly responsible for the volume produced vibrational states.

There is an additional mechanism involved in vibrational kinetics which is not presented in Figure 2.9. This mechanism, concerns the formation of vibrationally excited molecules via recombinative desorption of atoms on surfaces facing the plasma. Under certain conditions (related to plasma parameters, wall material, wall temperature) this process might greatly influence vibrational and rotational kinetics [39]. The following section is a brief presentation of its basic principles.

2.2.2 Recombinative desorption on surfaces

The chamber walls have a catalytic effect on various elementary processes such as elastic scattering of particles, adsorption, vibrational deactivation, dissociative and associative mechanisms. Recombination of gas phase atoms is of particular importance in negative ion sources as it may recycle hydrogen atoms into vibrationally excited molecules [114]. This way, the density of vibrationally excited molecules with enhanced DA cross section is increased and the density of the atoms which can destroy negative ions through detachment processes is reduced.

The catalyticity of the surface depends on the interaction of the gas phase species with the atoms on the crystal lattice of the surface and, on a bigger (microscopic) scale, the morphology of the surface. This catalyticity is quantified by the recombination coefficient γ which is defined as the ratio of the number of particles undergoing recombination to the total number of particles that flow to the surface per unit time. Therefor γ assumes values from 0, for a non-catalytic, to 1 for a fully catalytic surface [39].

The atom recombination mechanisms, namely Eley-Rideal (ER), Langmuir-Hinshelwood (LH) and hot-atoms, are depicted in Figure 2.10. All of them require the earlier adsorption of an atom by the surface (Reaction (2.19)) and lead to the formation of a molecule which is released (desorbed) back into the gas-phase.

$$(\mathrm{H})_{\mathrm{gas}} + \mathrm{surface} \rightarrow (\mathrm{H})_{\mathrm{ads}} \qquad (2.19)$$

Based on a simplified 1D model of the potential profile near a clean surface, the distinction of two adsorption schemes is possible: physisorption and chemisorption. In the first case the adsorbed atom is located in a shallow potential well created near the surface due to van der Waals or electrostatic dipole long-range attraction forces of the surface atoms. In the chemisorption scheme, the atom creates a chemical bond characterized by a deeper potential well located even closer to the surface [39]. Multidimensional modelling of the gas-solid interface, allows studying additional phenomena attributed to the presence of defects or impurities as well as the dependence on the angular coordinates of the approaching trajectory [115].

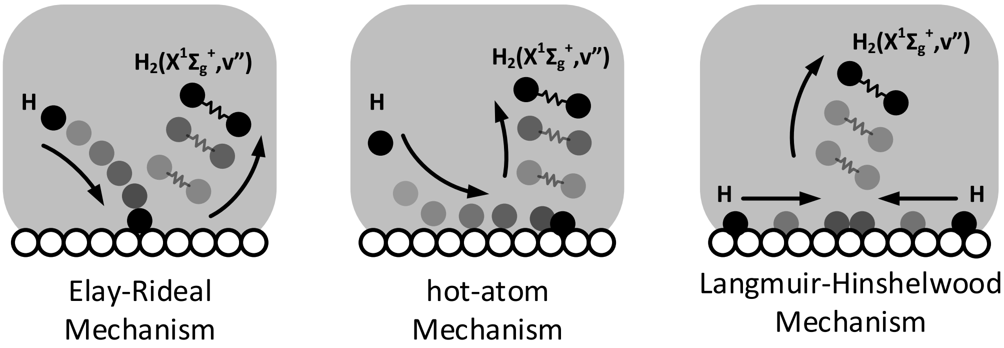

Figure 2.10. Pictorial view of the surface recombination mechanisms

In the ER recombination (Reaction (2.20)) a free gas-phase atom approaches the surface and recombines with an adsorbed atom. On the other hand, the LH recombination (Reaction (2.21)) involves two adsorbed atoms able to migrate on the surface (most likely physisorbed) and recombine with each other. Both reactions are exothermic (ΔE is the energy released during the desorption of the molecule).

$$\left(\mathrm{H}\right)_{\mathrm{ads}}+\left(\mathrm{H}\right)_{\mathrm{gas}}\rightarrow\left(\mathrm{H}_2\left(\mathrm{v}'',\mathrm{J}\right)\right)_{\mathrm{gas}}+\mathrm{surface}+\Delta\mathrm{E} \qquad \text{(ER)(2.20)}$$

$$\left(\mathrm{H}\right)_{\mathrm{ads}}+\left(\mathrm{H}\right)_{\mathrm{ads}}\rightarrow\left(\mathrm{H}_2\left(\mathrm{v}'',\mathrm{J}\right)\right)_{\mathrm{gas}}+\mathrm{surface}+\Delta\mathrm{E} \qquad \text{(LH)(2.21)}$$

The hot-atom recombination [116], is somewhere between these two mechanisms and involves a gas phase atom becoming weakly bound on the surface. This atom (designated as hot-atom) may easily migrate on the surface and recombine with an adsorbed atom [39].

All these mechanisms, may be quantified by a thermal macroscopic recombination coefficient. This coefficient however, is the result of integration over the translational energy distribution of atoms and includes all the components that correspond to each ro-vibrational state. In order to study the effect of wall recombination on the vibrational kinetics, the state-specific recombination probability is needed [117,118]. Such studies have been realized for hydrogen at graphite and crystal metals surfaces, due to their relevance in plasma reactors for nuclear fusion [119,120] and interstellar chemistry [121,122]. For a more complete review on the phenomena involving hydrogen atom recombination on surfaces, the reader is referred to the work of Capitelli et al [39], and the references therein.

2.3 Electron cyclotron resonance sources

Recently Electron Cyclotron Resonance (ECR) plasma sources have been widely explored in various plasma and ion beam technologies [123]. Their applicability on the production of hydrogen negative ions has been an ongoing investigation [31,51,124]. This section is a short presentation of its basic principles.

The ECR concept was initially used in the 1940s [125,126], while the fundamental properties and characteristics of microwave plasmas in static magnetic fields where studied later by Brown and his colleagues [127,128]. Such phenomena include breakdown, plasma confinement and ionization balance, microwave power absorption and resonant phenomena. In the years that followed, the ECR plasma generation was applied in various fields including fusion plasma heating [129], multiply charged heavy ion sources [130], plasma etching [131] and various others.

A typical ECR plasma source involves a microwave introduction technique (window, waveguide, antenna) and a magnetic field arrangement (coils, permanent magnets). The key element, is the principal microwave absorption zone where the plasma is generated. This zone is defined as locus where the imposed microwave frequency is equal to the gyrofrequency (Equation (2.22)).

$$\omega = \omega_{ce} = \frac{eB}{m_e} \tag{2.22}$$

where ω is the imposed microwave frequency, ω_{ce} is the electron cyclotron frequency, e and m_e are the electron charge and mass and B the value of the magnetic field. The requirement for resonance came from the expression of time averaged microwave power density which is transferred to "cold" electrons at the microwave breakdown [125,126]:

$$P = \sigma E_{\perp}^2 = \frac{e n_e E_{\perp}^2}{4 m_e} \left\{ \frac{\nu_e^2}{\nu_e^2 + \left(\omega - \omega_{ce}\right)^2} + \frac{\nu_e^2}{\nu_e^2 + \left(\omega + \omega_{ce}\right)^2} \right\} \tag{2.23}$$

where σ is the plasma conductivity, $E_{\perp}$ is the component of the magnetic field that is perpendicular to the magnetic field and v_e is the electron collision frequency. The first term in the right-hand part of Equation (2.23) represents the right-hand polarized waves (R-wave), while the second one the left-hand polarized waves (L-wave). In the first case, the electron rotates around the magnetic field in the same direction as the vector of the electric field while in the second case it rotates in the opposite direction. It can be seen that electron cyclotron resonance can only happen for the R-waves [123].

While this "pure" ECR absorption describes accurately enough the microwave breakdown, when the plasma is present the analysis of microwave absorption becomes much more complicated and various dissipative mechanisms may coexist. These mechanisms include: "pure" electron cyclotron heating [125], Doppler shifted ECR [132], Whistler wave absorption [133], L-wave absorption [134,135], hybrid resonances [136,137], harmonic resonances [136], plasma geometrical resonances [138], stochastic heating [139], nonlinear power absorption [140] and non-resonant collisional absorption [136]. For an extensive review of these processes the reader is referred to [123,136,141] and the references therein.

Plasma processing research motivated the extrapolation of ECR plasma sources, leading to the development of the distributed ECR sources [142]. In these sources, the confinement structure consists of multidipolar magnetic field, usually generated by permanent magnets. In such designs, the plasma is obtained by applying the microwave electric field along a multipolar magnetic structure. However, the production of uniform plasmas requires standing waves with constant amplitude along the linear applicators [142]. In order to obtain a standing wave along a transmission line, a reflected wave is required meaning that the microwave power sent to the antenna must be sufficiently high and its absorption by the plasma sufficiently weak [67]. However, input power cannot be increased indefinitely due technical limitations leading to limited density plasmas (maximum limit being the critical density [67]). Additionally, impedance matching becomes quite tricky, especially when the microwave applicators are positioned close to each other so that they may interact [67,143].

For circumventing the limitations of DECR plasmas, the concept of elementary plasma sources was introduced [67,143]. Using these elementary, independently powered microwave applicators in two- or even three-dimensional networks plasma sources may be extrapolated in size without any limitations.

2.3.1 Elementary dipolar electron cyclotron resonance sources

The operation of the elementary plasma sources is described in detail by Lacoste et al [67]. Briefly, each one consists of two parts: a cylindrical samarium-cobalt (Sm_2Co_{17}) permanent magnet, magnetized along its axis, and a coaxial line parallel to the magnetization vector, with an open end at the rear pole of the magnet (Figure 2.11).

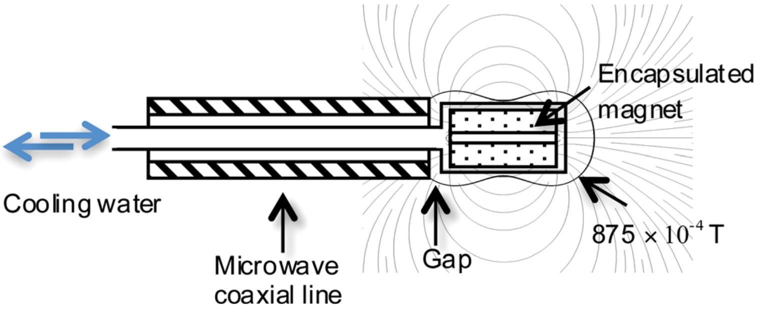

Figure 2.11. Conceptual design of an dipolar plasma source [124]. Microwaves are introduced by the left side. The microwave coaxial line ends at the rear side of the encapsulated magnet. The size of the gap between the coaxial line and the magnet is 4.5 mm. Magnetic field lines (thin lines) and contours of equal intensity (875 G) (peanut shaped line) are also represented.

Thus, the microwave power can be transmitted through the plasma and be mostly absorbed near the region where the ECR condition is fulfilled (peanut shaped line of Figure 2.11). For the microwave frequency of 2.45 GHz used here, the required magnetic field is 875 G (Equation (2.22)).

The operation of a source of similar geometry has been the subject of a numerical study [144]. This study clearly shows that the electric field, dominated by its radial and azimuthial components, remains perpendicular to the mainly axial magnetic field. Under these conditions, even for low working pressures (~ mTorr), the microwave coupling is highly efficient and produces locally hot electrons that induce high ionization and excitation. This selective electron heating should be quite beneficial for negative ion sources, where high energy electrons are needed for the production of the DA reactants: vibrationally excited molecules created through high threshold singlet excitation (Equation (2.18)) and low energy electrons generated by the even higher threshold electron impact ionization.

Synopsis

An efficient hydrogen negative ion source would require the abundance of two reactants: low energy electrons and hydrogen molecules excited to high vibrational states. High energy electron impact processes is the main source of both these species. An additional source for vibrationally excited molecules might be the recombinative desorption of atoms on the plasma chamber walls. ECR appears to be an efficient way of electron heating that could lead to the necessary ionization and vibrational excitation. At the same time an ECR configuration contributes to the spatial separation of hot and cold electrons. The ECR sources used in this study have a particularly practical design and very stable operation [67,143]. In the following chapters, the application of these sources to negative ion production and the analysis of the related phenomena will be presented.

Chapter 3. Experimental setups

Abstract

The H^- negative ion source Prometheus I, which is the main source of this study, is presented in detail along with the installed diagnostic techniques. These techniques include electrostatic probes and laser photodetachment as well as visible and vacuum ultraviolet emission spectroscopy. This source is devoted to the study of H^- production when vibrational excitation is mainly attributed to volume processes like EV excitation. Then, the negative ion source ROSAE III and the concept on which it was designed are also described. The design of this source aims at the assessment of the role of recombinative desorption of atoms on negative ion production in ECR plasmas. The final part of the chapter, presents the source SCHEME which is adapted in the beamline DESIRS of Synchrotron Soleil. The VUV synchrotron radiation is used for absorption and induced fluorescence measurements. This effort aims at the independent investigation of recombinative desorption of atoms into ro-vibrationally excited molecules.

3.1 Negative ion source Prometheus I

The source Prometheus I is installed in the High Voltage Laboratory of the Electrical and Computer Engineering Department of the University of Patras (Greece). Its design is presented in Figure 3.1. The chamber of the source is cubic (24 cm inside edge) and made out of stainless steel. Viewports have been adapted on the front and back side of the chamber, as presented in Figure 3.1, to give access for the necessary optical and laser diagnostics. On the other two sides, feedthroughs are adapted to give access for pressure monitoring and probes.

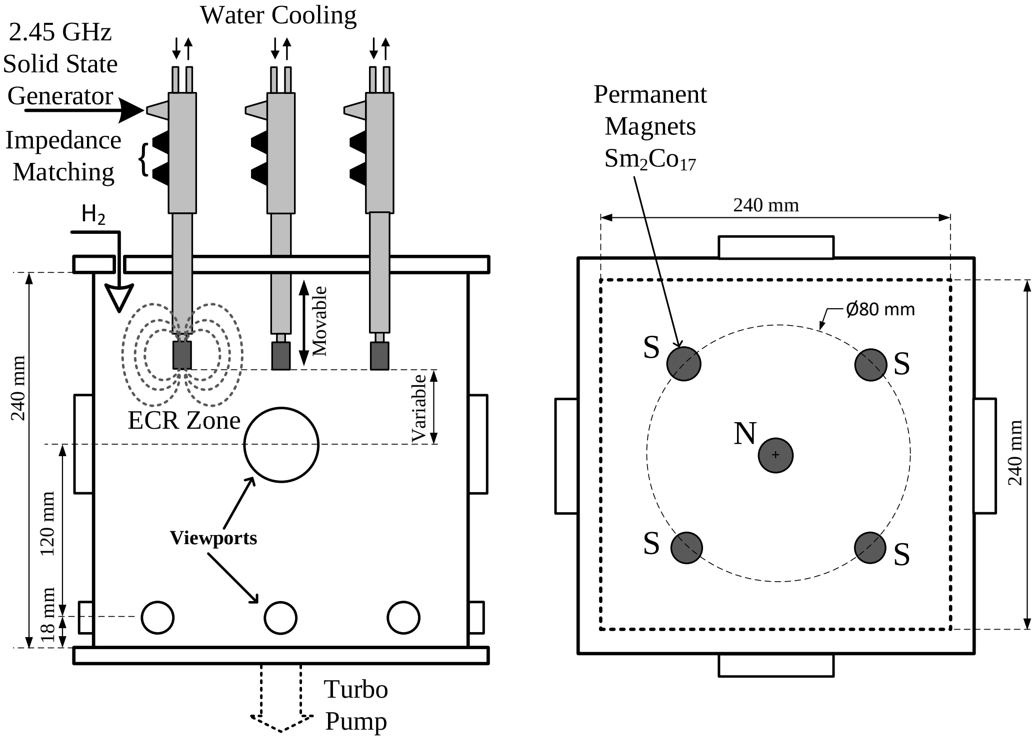

Figure 3.1. Conceptual diagram of the H^- source Prometheus I (side-view and top-view).

A turbo-molecular pump (Adixen Alcatel ATP 80), adapted under the bottom flange of the chamber, pumps the source down to $3x10^{-7}$ Torr. Pure H_2 (N50) is introduced by a digital mass flow controller (MKS 1179B) at a flow rate up to 24 sccm. Filling gas pressure up to 20 mTorr is accurately monitored by an absolute pressure transducer (MKS Baratron 627D). The discharge is operated with flowing neutral gas with a typical duration for a complete gas exchange being approximately 0.5-1 s, greatly exceeding all equilibration times in plasma. Therefore, the only effect the continuous gas flow has on the stationary plasma equilibrium is to prevent impurities from building up [30].

The plasma is sustained by a network of five dipolar ECR plasma sources [67] (see Section 2.3.1). The sources are introduced in the chamber by o-ring glands that tighten around them to sustain the vacuum, allowing at the same time their vertical movement. Each elementary plasma source is driven by an independent microwave power supply (2.45 GHz) able to provide up to 180 W. A tuner embedded on the main body of each source is used for impedance matching. By matching the impedance, the power that is reflected back to the supplies can be minimized and the incident microwave power is transmitted towards the plasma almost in its entirety. During the operation of Prometheus I, the matching is manually optimized. The maximum acceptable reflected power is 5 W. Both the sources and their supplies are cooled by a closed circuit of water, driven by an industrial scale water-cooling system (CoolMaster K-003.6).

One source is positioned in the center of the top flange and the other four are peripheral. Peripheral sources have a distance of 80 mm from the center. In order to create a more homogeneous plasma, the permanent magnets of the sources should have alternating polarities [67]. In Prometheus I the peripheral sources have the opposite polarity from the central one. The magnetic field created by the five sources is calculated using the ACDC module of the COMSOL Multiphysics numerical suite. The iso-B contours on a diagonal cut-plane are presented in Figure 3.2a. The ECR zones correspond to the inner contours where the magnetic field intensity is 875 G.

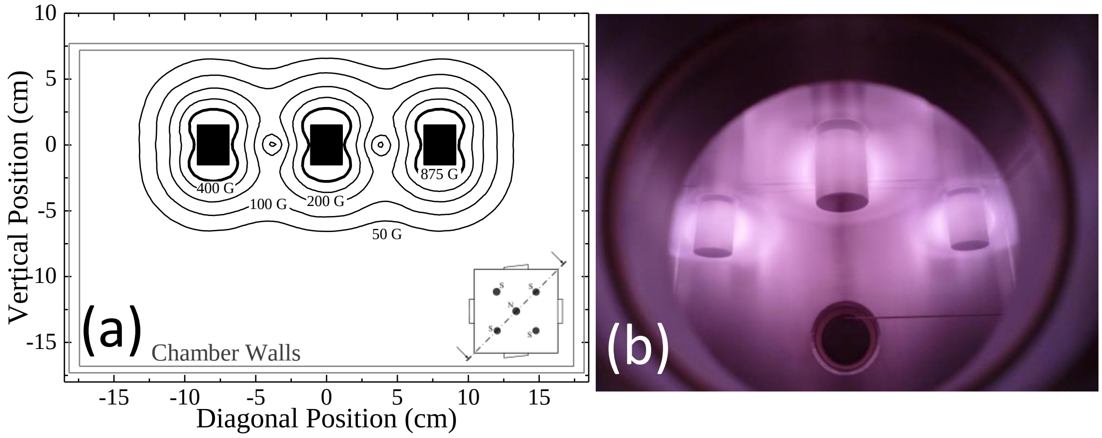

Figure 3.2. (a) Static magnetic field created by the five permanent magnets. The inlet indicates the chosen diagonal cut-plane. This calculation assumes that the five sources are positioned with their mid-plane 65 mm above the central viewport. (b) Operation of the five (only three are visible from the chamber viewport) ECR dipolar sources in pure H_2. The filling gas pressure is 10 mTorr and each source is supplied with 180 W of microwave power.

For the application of negative ion production, the magnetic field has two functions. The first one is the creation of the necessary magnetic field configuration that satisfies the ECR condition. The second function is to confine energetic electrons in the vicinity of the magnets and, in that respect, be the magnetic filter of the source (see Section 2.1.2). The plasma of the source Prometheus I is depicted in Figure 3.2b. The considerably more luminous areas near the magnets indicate the regions where highly energetic electrons are confined.

A conceptual diagram of the entire experimental setup is presented in Figure 3.3. The diagnostics that are installed are electrostatic (Langmuir) probes, laser photodetachment, optical emission spectroscopy and VUV emission spectroscopy. In the subsections that follow each diagnostic technique is presented in detail.

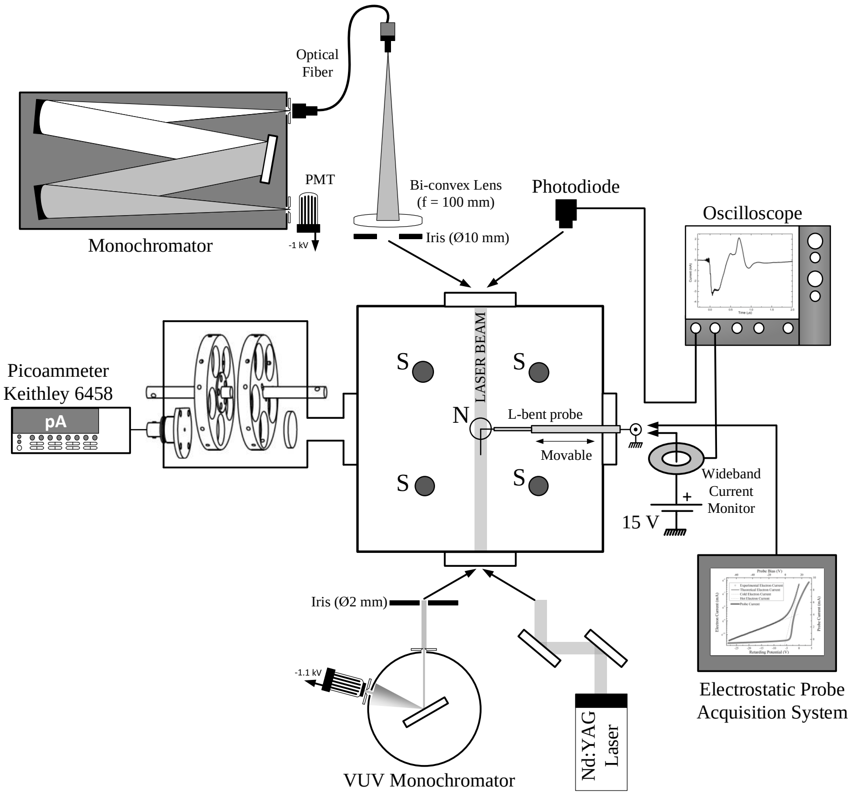

Figure 3.3. Experimental setup of the negative ion (H^-) source Prometheus I. The diagnostics installed include: Electrostatic probes, photodetachment as well as visible and VUV emission spectroscopy.

The source is depicted in Figure 3.4. The important parts of the experimental setup are numbered and explained. Currently the photodetachment diagnostic technique is operating with a single laser pulse in order to measure negative ion densities as will be presented in Section 3.1.2. However, a main perspective of this project is to use the second laser of the experimental setup, in order to perform photodetachment measurements with two laser pulses, for the determination of negative ion temperatures [145].

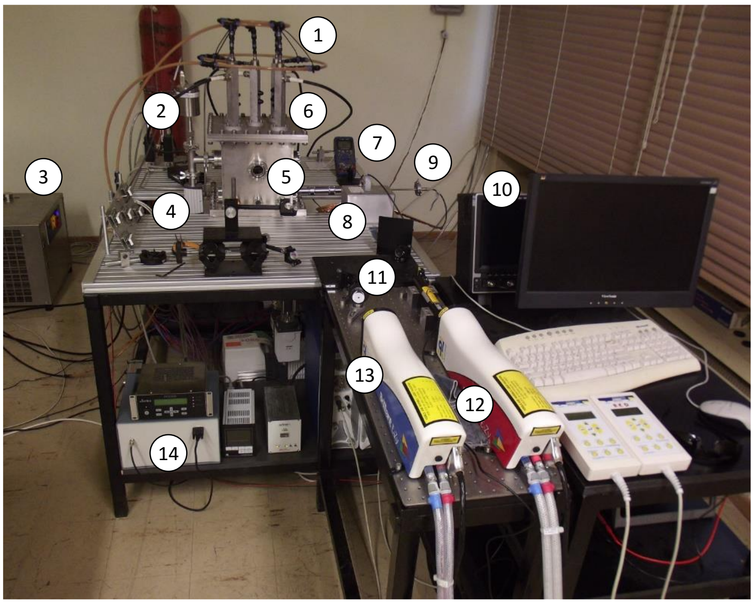

1. Closed circuit of water for cooling
2. Baratron (Working pressure monitoring)
3. Industrial Cooler
4. Pinani (Base pressure monitoring)
5. Negative Ion Source Prometheus I
6. Dipolar ECR sources
7. Chamber temperature monitoring
8. Photodetachment current measuring circuit
9. Electrostatic probe
10. Oscilloscope for photodetachment signal
11. Optics for the alignment of the two lasers
12. First laser for single pulse photodetachment
13. Second laser for two pulse photodetachment
14. Electrostatic probe acquisition system

Figure 3.4. The source Prometheus I, with the probe and the laser photodetachment diagnostics.

3.1.1 Electrostatic probes

A cylindrical electrostatic (Langmuir) probe is inserted in the plasma by the side of the chamber as presented in Figure 3.5. The probe tip is a 0.25 mm thick tungsten wire, which is L-bent so it can be aligned with the laser beam for the photodetachment measurements (see next sub-section). The exposed part of the wire is 15 mm with the long part being 11 mm and the short one 4 mm. The probe wire is housed in a telescopic configuration of dielectrics (alumina tube inside a wider quartz tube) that protect it from the plasma. The quartz tube is supported inside a stainless steel tube that ends in a standard BNC connector. A gland that tightens around the steel tube sustains the vacuum and at the same time allows the linear movement of the probe.

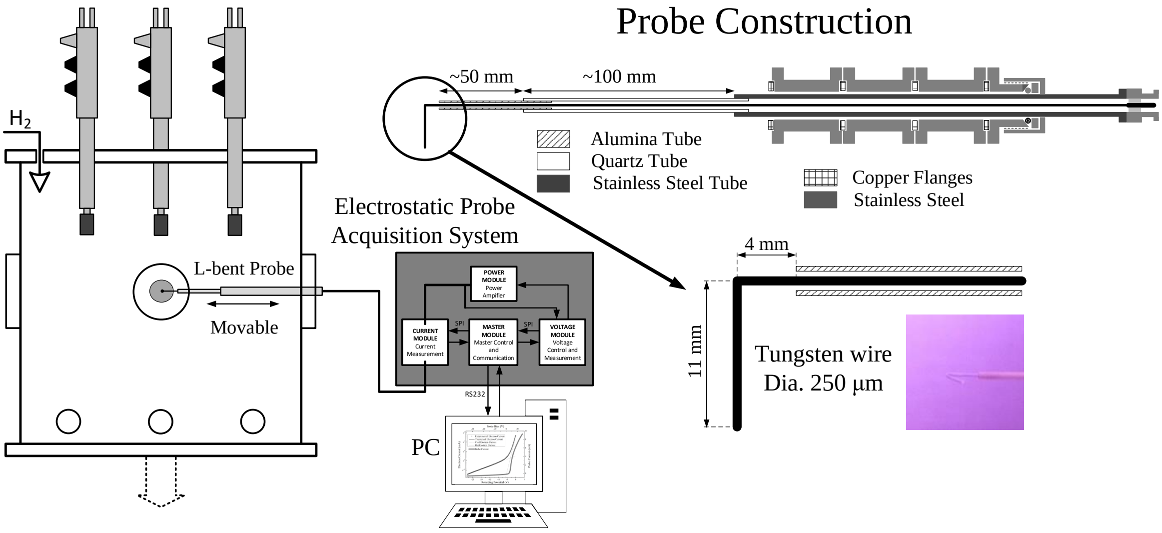

Figure 3.5. Electrostatic probe configuration and probe construction. The dimensions of the tip of the probe are presented in detail. The system that biases the probe and acquires the voltage-current curves is described elsewhere [146].

The acquisition of electrostatic probe curves is accomplished with a custom-made system designed and implemented in the frame of this thesis. For a detailed description of the circuit the reader is referred to the author's Article 3[2]. Each measurement procedure starts with 10 s of probe cleaning by electron current-induced incandescence followed by another 10 s of cooling-down. The voltage-current curve acquisition that follows is realized point by point in steps of approximately 100 mV. For each point 2^{12}-2^{13} voltage-current samples are averaged in order to reduce plasma induced noise. If necessary, the average of many curves might also be calculated.

The magnetic field at the probe tip depends on the position of the probe and the position of the sources. In this work, the closest position of the probe to the magnets, is 65 mm below their mid-plane. In that case the maximum magnetic field intensity is 51 G (from the magnetostatic calculation of Figure 3.2a), while the direction of the magnetic field is always perpendicular to the probe. For the experiments that are

---

[2] Reference to the list of publications in page 104

conducted, the lowest electron temperature observed is 0.5 eV which corresponds to an electron Larmor radius of about 0.34 mm. Thus, even in the worst case the probe radius (0.125 mm) is smaller than the electron Larmor radius, which validates the use of "classical" non-magnetized probe theory [33,147,148].

Typical plasma parameters are obtained by a fitting procedure directly on the probe voltage-current (V-I) curve [149]. More specifically, the plasma potential is estimated from the maximum of the first derivative of the V-I curve and the floating potential from the zero-crossing point. The current of positive ions is estimated by linear extrapolation of the probe current in high retarding potentials and is subtracted from the total current. The rest of the current (electron current) is fitted by the sum of two exponential functions (bi-exponential function, Figure 3.6a) which corresponds to a bi-Maxwellian electron energy distribution function (EEDF). The experimental EEDF is derived from the second derivative of the total probe current (Druyvesteyn method) [148,150]. Figure 3.6b shows how well the experimental EEDF coincides with the bi-Maxwellian EEDF that corresponds to the parameters obtained by the fitting procedure.

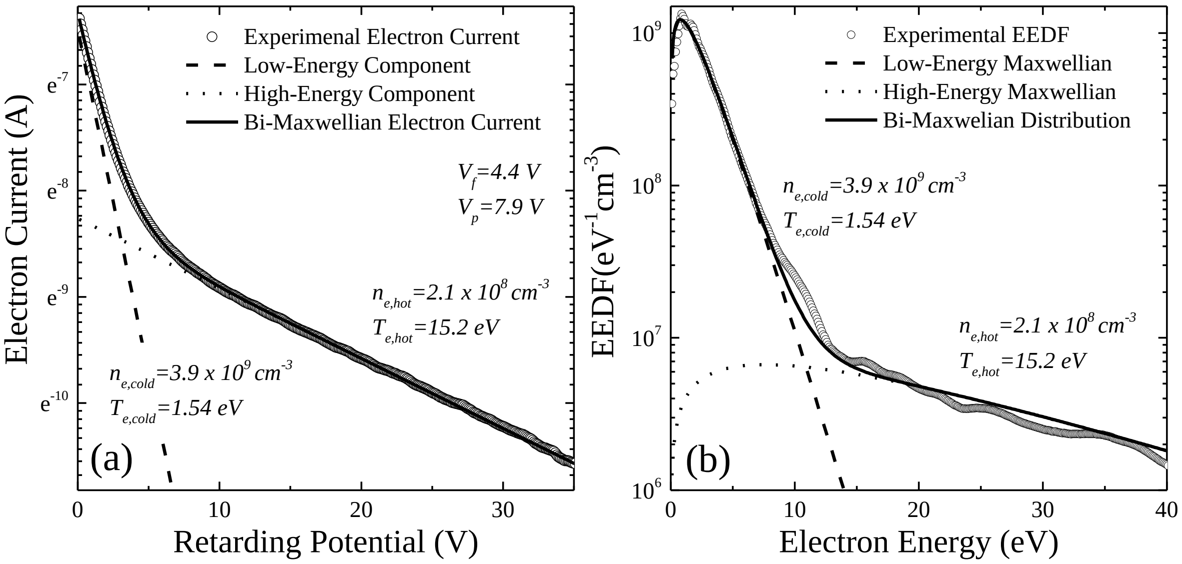

Figure 3.6. Typical case of electrostatic probe measurement (Power = 180 W/sources, Pressure = 4 mTorr). (a) Bi-exponential fitting to electron current data for the determination of the density and the temperature of cold and hot electron populations. (b) Experimental EEDF derived by the Druyvesteyn method compared with the EEDF derived by (a).

For the treatment of experimental data, a Matlab™ program was developed. The program applies the fitting procedure for the determination of electron densities and temperatures, and then calculates the second derivative for the determination of EEDF. For the removal of noise, a sliding Savitzky-Golay filter [151] is designed. In order to correctly apply the Savitzky-Golay filter, evenly spaced data are acquired through and interpolation procedure on the experimentally derived curve. The window of the filter starts from low values (~0.3 eV) in the low energy area and is gradually increased by about 0.2 – 0.3 eV per eV of electron energy [152]. Naturally, this filtering procedure reduces the resolution of the acquired EEDF for higher energies.

3.1.2 Laser Photodetachment

The laser induced photodetachment diagnostic technique with one laser beam [145] is used for measuring the negative ion density. The experimental configuration is presented in Figure 3.7.

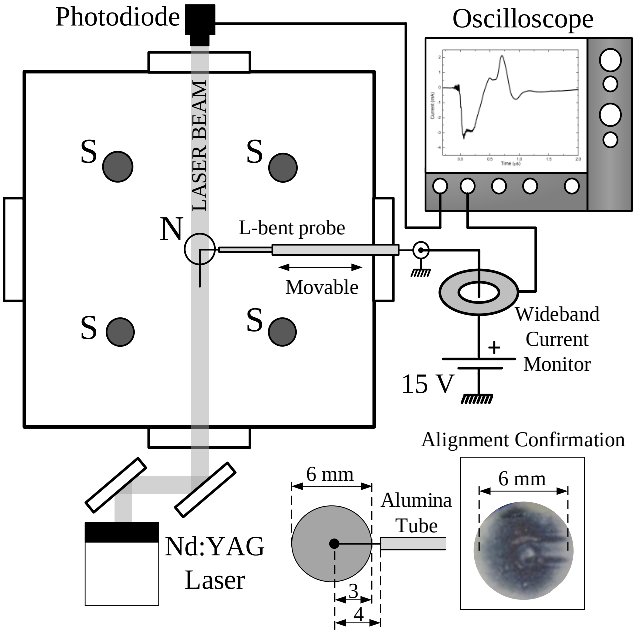

Figure 3.7. Experimental configuration for the photodetachment measurements. The inlet presents the confirmation of alignment on infrared photo-sensitive paper.

A short (~5 ns) Nd:YAG 1064 nm laser pulse generated from a Quantel-Brilliant EaZy (330 mJ/pulse), concentrically aligned with the long part of the electrostatic probe mentioned above, detaches the extra electron of negative ions inside the cylindrical irradiated volume. The excess electrons in the area sharply increase the electron current collected by the positively biased probe. A typical photo-electron current pulse is presented in Figure 3.8.

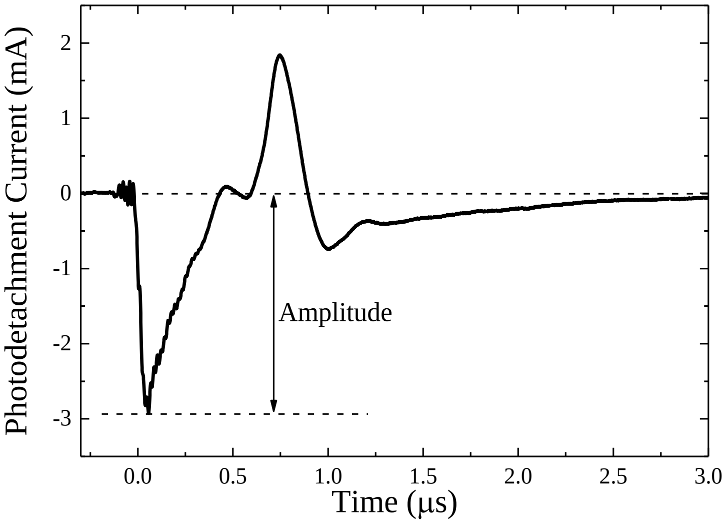

Figure 3.8. Typical photodetachment signal. From the amplitude of this signal the negative ion density can be estimated.

Negative ion density (n_-) can be calculated from the equation [54,145]:

$$\frac{\Delta I_{PD}}{I_{DC}} = \frac{n_-}{n_e} \tag{3.1}$$

where ΔI_{PD} is the amplitude of the photodetachment signal, I_{DC} is the DC electron current collected when it has the same bias used for the photodetachment technique and n_e is the electron temperature which is determined by the electrostatic probe measurements.

In order to decouple the transient photodetachment current from the continuous current of the background electrons, an AC decoupling circuit has to be used. However, the conventional capacitive decoupling circuit [145] has some limitations regarding its bandwidth [153] and can lead to errors in the measurement of negative ions density. To avoid any potential bandwidth related errors, the photodetachment pulse is measured with a wideband AC current transformer (Pearson electronics 6585) which is connected directly to the oscilloscope (LeCroy WaveSurfer 104Xs-A).

For the valid application of the photodetachment technique, the parameters of the system had to be chosen according to specific rules [54,145,154]. One has to choose a proper laser beam radius and energy density, as well as a proper probe bias. The radius of the laser beam should be greater from the collecting radius of the probe. The collecting radius is determined by the probe radius and the thickness of the electron sheath. The radius of the probe is 0.125 mm while the sheath thickness is in the order of the Debye length. For the worst case (highest electron temperature of about 2 eV and lower electron density of about $1x10^9$ cm^{-3}) the Debye length can be as high as 0.4 mm. The radius of the laser beam is 3 mm, which exceeds the collecting radius.

The energy density of the beam should be high enough to detach the electrons from all the negative ions inside the illuminated volume. The energy that is necessary can be theoretically calculated using the photodetachment cross section [145]. However, the simplest way to confirm the detachment of all electrons is to vary the laser energy and verify that the measured photodetachment pulse is saturated. The evolution of the normalized pulse amplitude as a function of laser energy density is presented in Figure 3.9a. An energy density of about 20 mJ/cm^2 seems to be enough to reach saturation. However, the operation of the available laser system (Quantel-Brilliant EaZy) becomes unstable below 40 mJ/cm^2 energy densities. Nevertheless, by varying the energy density between 40 and 100 mJ/cm^2 it is verified that the photodetachment current pulse is well saturated. The energy that was finally chosen for the conducted experiments was 70 mJ/cm^2.

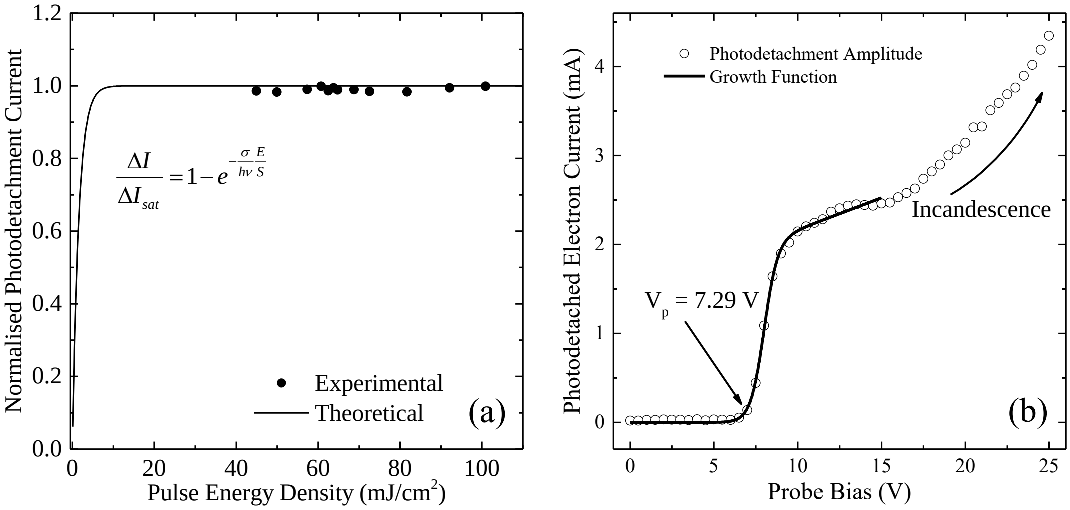

Figure 3.9. Dependence of photodetachment current amplitude on (a) the energy density of the laser beam and (b) the probe bias. The equation inside the first graph describes the theoretical dependence of the normalized photodetachment pulse amplitude. σ is the photodetachment cross section [145], hν the energy of the photons, E the energy of the laser pulse and S the laser beam cross-sectional area.

The general rule for choosing a proper probe bias, is to be well above the plasma potential, so that the probe will collect all the photo-detached electrons in its vicinity. The evolution of the photodetachment current as a function of the probe bias is presented in Figure 3.9b. It is obvious that after the plasma potential the pulse amplitude increases abruptly and becomes saturated. However, if the probe bias is further increased, the excess electron current starts to heat the probe and lead to incandescence. This is related with an increase in the photodetachment current and operation in this bias region should be avoided. A series of measurements like the one presented in Figure 3.9b concluded that a probe bias of 15 V is always well above plasma potential and never leads to probe incandescence. Thus the probe bias was fixed to 15 V for all the photodetachment measurements presented in this work.

3.1.3 Visible Emission Spectroscopy

Visible emission spectroscopy, is a diagnostic technique that is routinely used on H^- sources. The main advantages of this technique is being non-invasive and experimentally simple and robust. The experimental configuration of the high-resolution visible emission spectroscopy system used in this study is presented in Figure 3.10.

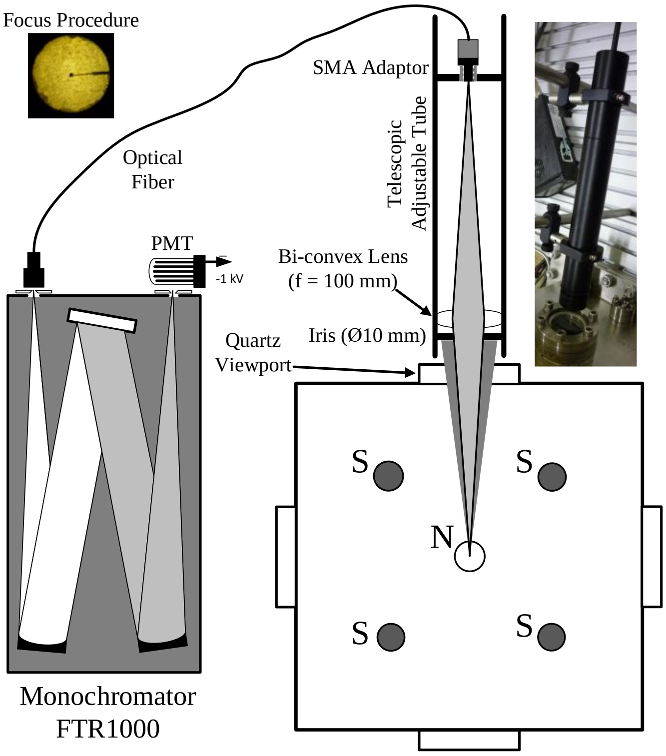

Figure 3.10. Visible emission spectroscopy configuration. The focus procedure is described in the inset.

For the visible spectroscopy measurements, a monochromator with a focal length on 1 m is used (FTR 1000). The light is driven into the monochromator with an optical fiber. In order to collect the light from the bulk of the plasma, a bi-convex lens is used to focus the light from the center of the chamber into the entrance of the optical fiber. The lens is adapted inside a telescopic tube which is depicted in the inset of Figure 3.10. The probe which is located in the center of the chamber is used as a target to focus on. During spectroscopy measurements, the probe is removed so that there are no objects in the line of sight of the measurement. The measured spectra are relatively calibrated in terms of intensity. This is achieved by employing a tungsten calibration lamp having a known emission spectrum (Newport 6333, 3300 K black body emission for 12 V supply). The calibration curve is presented in Figure 3.11.

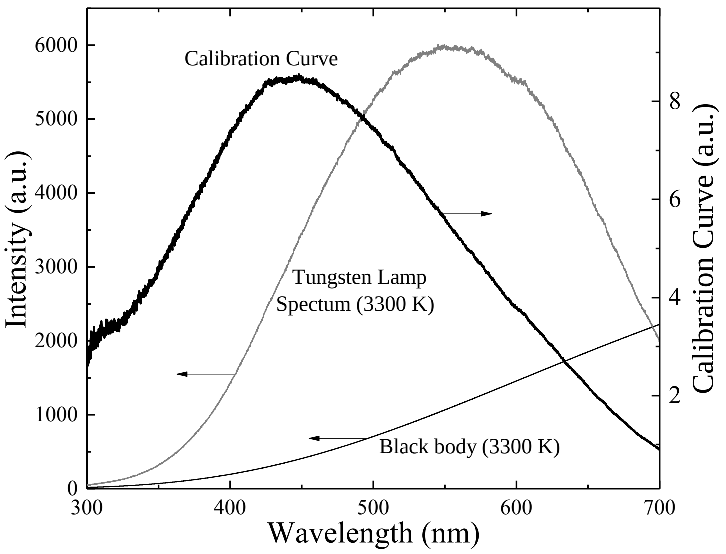

Figure 3.11. Calibration of the visible emission spectroscopy system. The calibration curve is derived by dividing the measured spectrum of the tungsten calibration lamp and the theoretical emission spectrum of the lamp (black body at 3300 K).

A typical emission spectrum of the H_2 plasma of Prometheus I is presented in Figure 3.12. Two components of the spectrum, which are very important for diagnostics, can be easily distinguished. The first is the Balmer series of atomic hydrogen. The first five spectral lines of the series are indicated in the figure as H_α, H_β etc. The other important component of the spectrum is the Fulcher band, which is emitted from the triplet transition $d^3\Pi_u \rightarrow a^3\Sigma_g^+$. The inset of Figure 3.12 focuses on the 600 – 650 nm wavelength region, where the diagonal bands $v_i = v_f$ =0, 1, 2, 3, 4 can be observed [155].

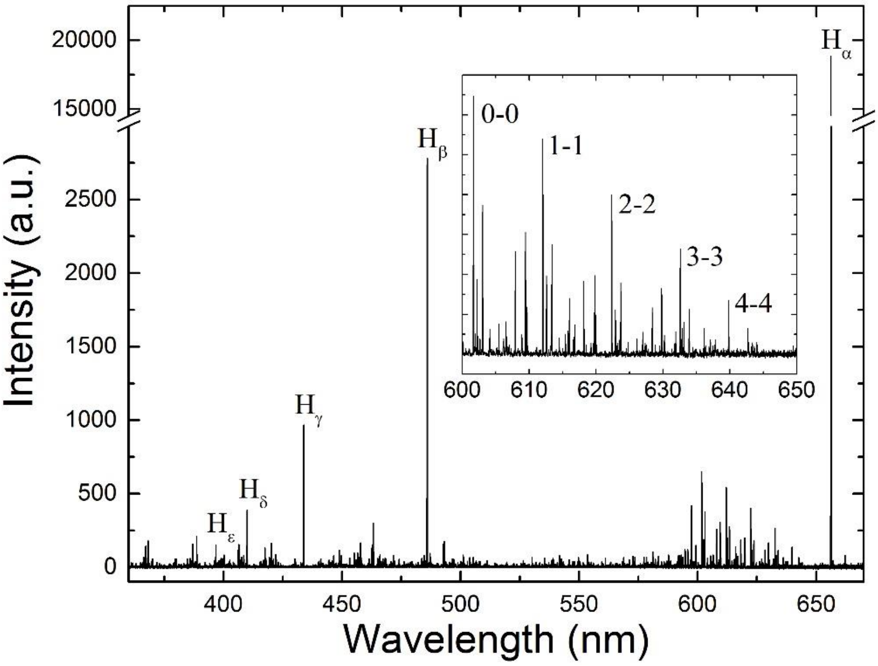

Figure 3.12. Typical emission spectrum of the H_2 plasma of Prometheus I.

The main drawback of emission spectroscopy, is that the interpretation of the spectra is not straightforward. Especially for molecular plasmas, the quantification of plasma parameters might require simple or even complex collisional-radiative models [156]. One parameter that can be measured in a direct manner is the translational temperature of the neutral atoms. This temperature can be measured directly from the Doppler broadening of atomic lines.

In low pressure plasmas the measured broadening $\Delta\lambda_{Meas}$ (Full Width at Half Maximum, FWHM) of atomic lines is given by the equation:

$$\Delta\lambda_{Meas}^2=\Delta\lambda_{Instrum}^2+\Delta\lambda_{Doppler}^2 \tag{3.2}$$

where $\Delta\lambda_{Instrum}$ is the instrumental broadening and $\Delta\lambda_{Doppler}$ is the Doppler broadening of the atomic line [157]. In order to calculate the instrumental broadening, the spectrum of HeNe laser beam can be used, which have a very thin spectral line. The FWHM of the measured laser spectrum (Figure 3.13) is essentially the FWHM that corresponds to the instrumental broadening. By considering a typical value of 0.0017 nm [158] for the laser linewidth broadening, the instrumental broadening would be 0.00848 nm which is only 1.7% lower. Since an accurate linewidth value was not available for the used HeNe laser (Oriel 79288, 633 nm, 4 mW), the introduced error is disregarded.

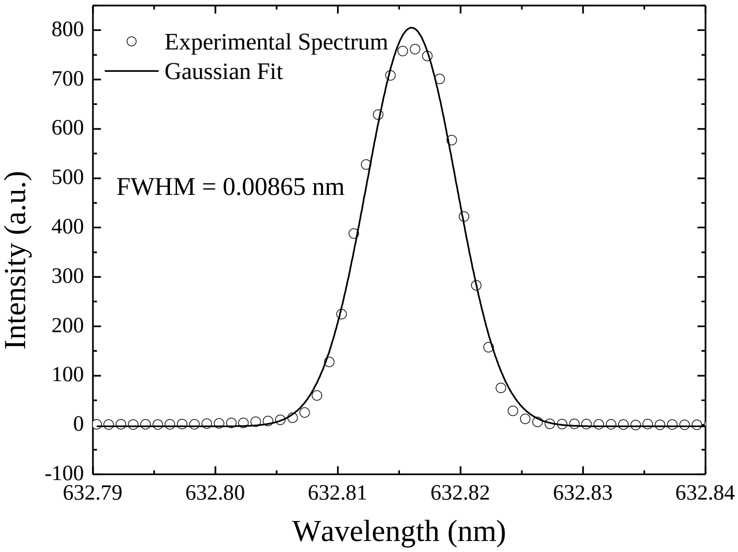

Figure 3.13. Spectrum of a HeNe laser, used to determine the instrumental broadening of the spectroscopic system (the entrance and exit slit is 20 μm).

A typical spectrum of the second Balmer line (H_β) is presented in Figure 3.14. The structure of the spectrum is bi-Gaussian owing to the different mechanisms that create H(n=4) atoms [159]. The central narrow component is attributed to the direct excitation of ground state hydrogen atoms, while the wider component (wings) is attributed to the dissociative processes [157,160]. The translational temperature of the atoms in their ground state is equal to the temperature of the H(n=4) atoms that are created through direct excitation [157]. This temperature can be determined by the central component of the H_β spectrum which needs to be separated. To accomplish this, the atomic spectrum is fitted by a tri-Gaussian function Figure 3.14. The first two components correspond to cold and hot atoms while the third one corresponds to a molecular emission at 486.17 nm [161].

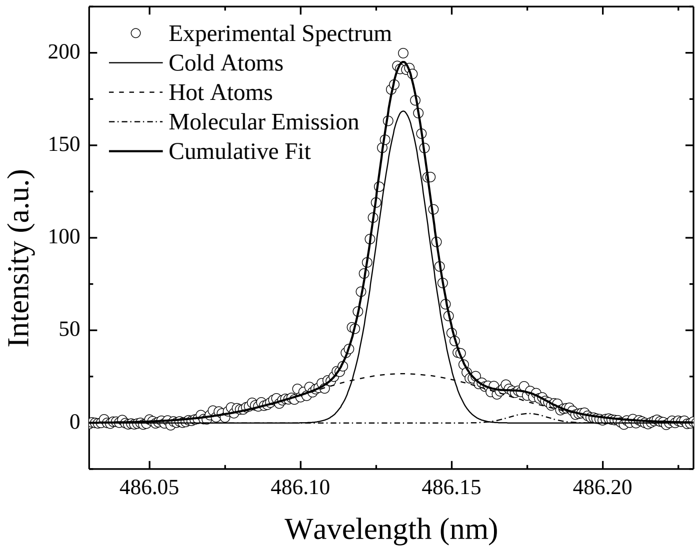

Figure 3.14. Typical spectrum of H_β atomic line. The bi-Gaussian structure of the spectrum reveals the presence of two atomic hydrogen populations (hot and cold atoms). The filling gas pressure is 4 mTorr and the power is 180 W. The entrance and the exit slits of the monochromator are 20 μm.

The Gaussian functions that correspond to emission by the hot atoms and the molecules, are subtracted and the remaining spectrum, which corresponds solely to direct excitation of ground state atoms, is used for the determination of the atomic hydrogen translational temperature (Figure 3.15). To account for the fine structure of atomic lines the experimental spectrum is approximated by two components (barycenters) as proposed in [157]. The two barycenters share the same broadening and are separated by 77 mÅ, which is the fine structure separation for the H_β line [160]. The broadening of the atomic line is calculated by equation (3.2) and is equal to 0.01499 nm. This broadening corresponds to a translational temperature of atomic hydrogen which can be calculated (in kelvins) by the following equation [157]:

$$\mathrm{T_H} = \left(\frac{\Delta\lambda_{\mathrm{Doppler}}}{\lambda} \frac{1}{716\times10^{-9}} \right)^2 \tag{3.3}$$

where λ is the central wavelength of the atomic line. The translational temperature that corresponds to Figure 3.15 is 1856 K. For this calculation the instrumental broadening is considered equal to the total broadening of Figure 3.13. If the typical value for the HeNe laser broadening is considered, the calculated temperature is 1879 K, i.e. only 23 K or 1.2% higher. For all practical purposes, the error introduced by the broadening of the laser can be ignored.

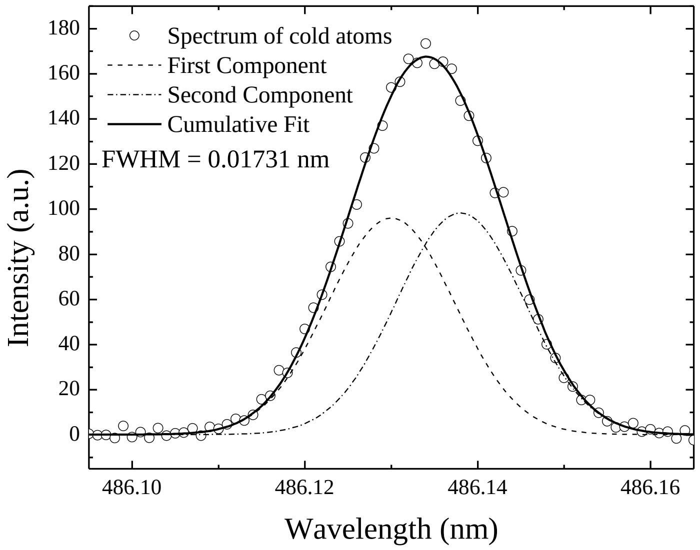

Figure 3.15. H_β line that corresponds solely to direct excitation from the ground state atomic hydrogen. The spectrum is fitted by two Gaussian components (barycenters) to account for the fine structure of atomic lines [157].

Emission spectroscopy is also used for the determination of the degree of dissociation. The spectra in this case have to be interpreted by using a simple collisional-radiative model (also known as corona model) that was developed by Lavrov et al [162,163]. This model requires the ratio of the first two atomic lines of Balmer series (H_α and H_β), to the Q1 line of the 2-2 band of the Fulcher-α band system (F(2-2)Q1). The central wavelengths of the H_α, H_β and F(2-2)Q1 lines in air are 656.283, 486.134 and 622.481 nm respectively. The spectra of these lines are presented in Figure 3.16.

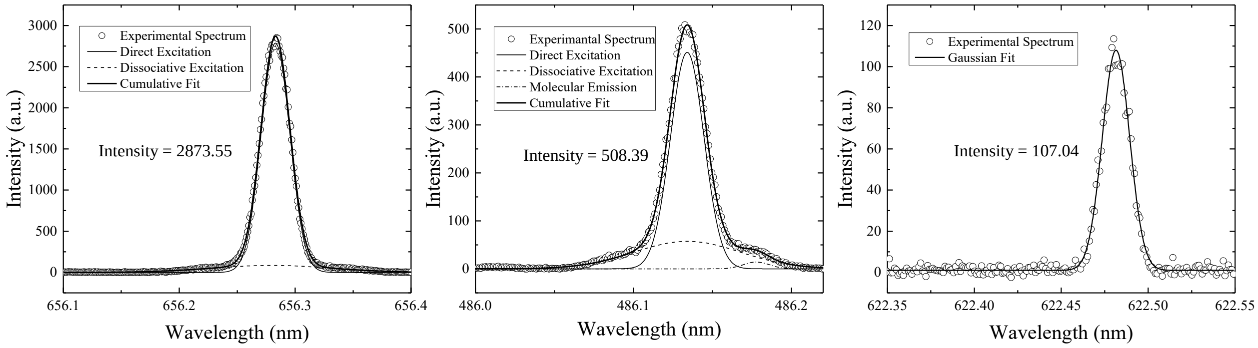

Figure 3.16. Spectra of the atomic and molecular lines used for the determination of the degree of dissociation (p = 12 mTorr, P = 180 W/source).

The ratio of the atomic to the molecular line is given by the equation:

$$\frac{I_{\alpha,\beta}}{I_{F(2-2)Q1}} = \frac{1}{\eta(T_g)} \frac{([H]/[H_2])K_{dir}^{\alpha,\beta}(T_{tail}^{eff}) + K_{dis}^{\alpha,\beta}(T_{tail}^{eff})}{A_{a21}^{d^-21}\tau_{d^-21}K_{ex}^{d^-21}(T_{tail}^{eff})} \tag{3.4}$$

where $\eta(T_g)$ is a function that reflects the dependence of F(2-2)Q1 line intensity on the molecular translational temperature, $[H]/[H_2]$ is the ratio of atomic to molecular density, $A_{a21}^{d^-21}$ is the probability of the $d^3\Pi_u^-$,v=2,J=1 →$a^3\Sigma_g^+$,v=2,J=1 radiative transition and τ_{d^-21} is the radiative lifetime of the $d^3\Pi_u^-$,v=2,J=1 state. The coefficients $K_{dir}^{\alpha,\beta}$, $K_{dis}^{\alpha,\beta}$ and $K_{ex}^{d^-21}$ are the rate coefficients of the direct excitation of ground state atoms to the n=3 (α) and n=4 (β) electronic states, the dissociative excitation of ground molecules to the same states and the excitation of ground state molecules ($X^1\Sigma_g^+$,v=0,J=1) to the $d^3\Pi_u^-$,v=2,J=1 triplet state. The values of the variables that are necessary for the calculation of [H]/[H_2] based on the line ratio are calculated and given in [162] as a function of the effective temperature of the high energy tail of the EEDF.

The energy tail for the experimental conditions that correspond to Figure 3.16 is measured with electrostatic probes and is about 15 eV. For this electron tail temperature, the rate coefficients for direct and dissociative excitation are respectively 1.12x10^{-9} $cm^{-3}s^{-1}$ and 6.02x10^{-11} $cm^{-3}s^{-1}$ for H_α, or 2.61x10^{-10} $cm^{-3}s^{-1}$ and 1.89x10^{-12} for H_β. For the same electron temperature, the value of the product $A_{a21}^{d^-21}\tau_{d^-21}K_{ex}^{d^-21}$ is 4.23x10^{-11} $cm^{-3}s^{-1}$. The translational temperature of the molecules, which is essential for the determination of the $\eta(T_g)$ parameter, is typically lower than the atomic temperature gas calculated from Figure 3.15 [157]. By adopting the ratio of 0.6 between atomic and molecular translational temperature [36] a more realistic molecular translational temperature of about 1100 K is acquired. For this temperature the parameter $\eta(T_g)$ is found to be equal to about 0.3.

By introducing these values and the measured intensities of Figure 3.16 in Equation (3.4), two values of the ratio of atomic to molecular densities are calculated. The first corresponds to the H_α line and is equal to 0.2499 and the second to the H_β line and is equal to 0.2236. The degree of dissociation (D) is calculated from the equation:

$$D = \frac{[H]}{[H]+2[H_2]} = \frac{[H]/[H_2]}{[H]/[H_2]+2} \qquad (3.5)$$

The degree of dissociation that corresponds to the two ratios is 11.11% and 10.06% respectively.

3.1.4 VUV Emission Spectroscopy

In low pressure plasmas, since electron impact excitations is the dominant excitation process [39], transitions in the VUV range become quite valuable as diagnostics [164]. Being transitions from the first excited state, they have greater electron impact excitation cross sections compared with higher electronic states [78]. Thus, in an initial approach, cascade transitions from higher states can be ignored. Furthermore, due to their short lifetimes, they have a photon emission rate that is proportional to the electron impact excitation rate from the ground state [164]. These two properties make the interpretation of the VUV spectra quite straightforward.

Despite their advantages, VUV emission measurements have a basic drawback which is the requirement of maintaining the entire spectroscopic system under vacuum. This requirement complicates the experimental setup and increases the cost of the equipment.

The light emitted by Prometheus I in the VUV spectral region was recorded using VUV spectrometer or an irradiance meter. The experimental setup with both devices is presented in Figure 3.17.

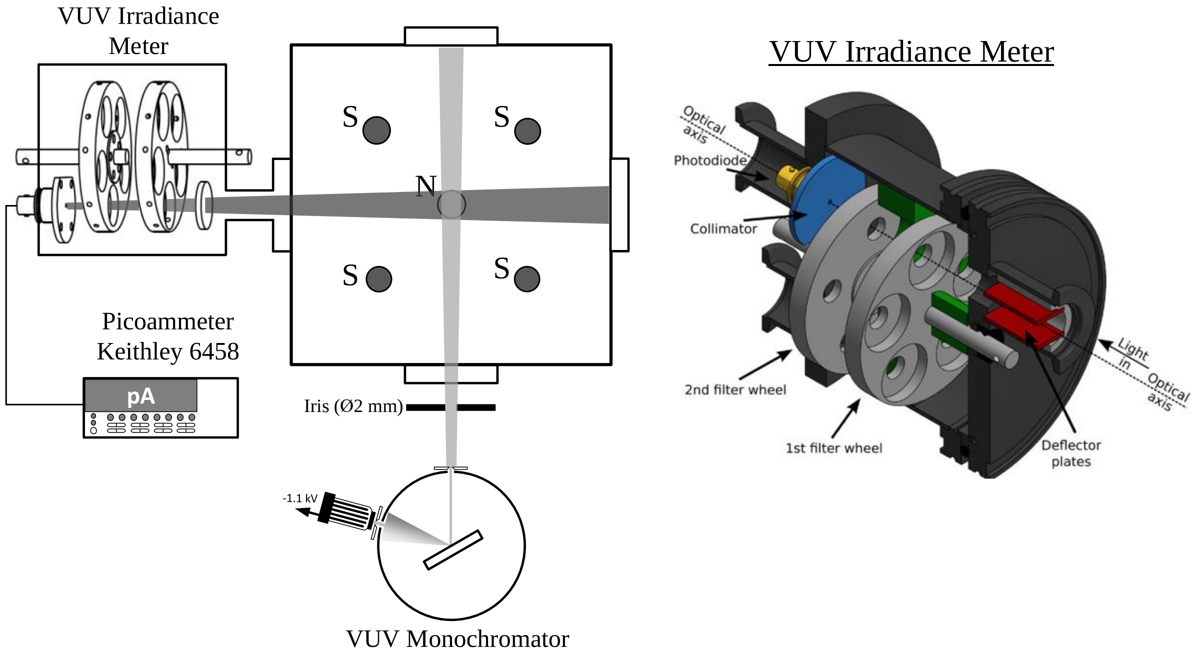

Figure 3.17. VUV emission spectroscopy configuration using the irradiance meter and the VUV monochromator. The 3D sketch presents the internal construction of the irradiance meter [51].

The VUV spectrometer consists of a monochromator with a focal length of 0.2 m (McPherson Model 234/302), a holographic grating and a photomultiplier tube (ET Enterprises 9406B). An additional iris is positioned in front of the entrance slit of the monochromator in order to increase the spectral resolution of the measurement.

A typical spectrum is presented in Figure 3.18. Four components of the spectrum are easily distinguished. The first component is the Lyman-α line at 121.6 nm, which is the first line of the Lyman series. It corresponds to the transition from the first excited state to the ground state of the hydrogen atom (1s←2p). In the VUV range there are also the Lyman band (92-184 nm) and the Werner band (84-158 nm). Intense emissions from the Lyman and Werner bands are observed around 160 nm and 120 nm respectively. These two bands correspond to transitions from the first two excited singlets ($B^1\Sigma_u^+$ and $C^1\Pi_u$) to the ground state of the hydrogen molecule ($X^1\Sigma_g^+$). As mentioned in Chapter 2, these transitions are considered to be the main production channel for high vibrational states in the bulk of the plasma. The last component of the VUV spectrum is the molecular continuum. This emission corresponds to the transition from the $a^3\Sigma_g^+$ to the $b^3\Sigma_u^+$ triplet which is repulsive and leads to dissociation.

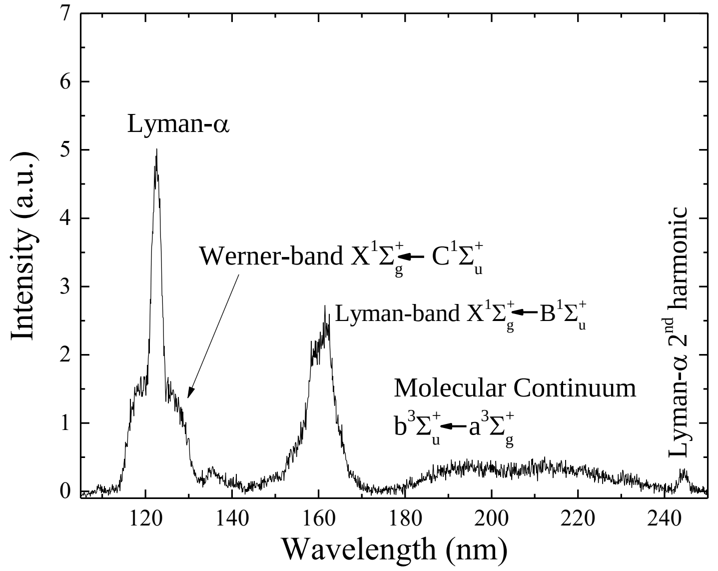

Figure 3.18. Typical VUV spectrum of the H_2 plasma of Prometheus I. In this case the monochromator looks in the ECR region. Each source is supplied with 180 W of power and the filling gas pressure is 12 mTorr. The spectrum is uncalibrated in terms of intensity.

The irradiance meter is described in detail by Komppula et al [51] and its mechanical construction is depicted in the inlet of Figure 3.17. Briefly, this device is based on an SXUV photodiode (IRD-incSXUV20BNC) with a responsivity of about 0.02 A/W in the VUV range (~100 - 200 nm). The photodiode current is measured with a digital pico-ammeter (Keithley 6458). Band-pass filters, centered in characteristic emissions of hydrogen plasmas, are placed in front of the diode. Three filters are used: a filter centered on Lyman-α at 122 nm (FWHM ~ 20 nm,), a filter centered on the peak of Lyman band at 161 nm (FWHM ~ 20 nm) and a filter on the molecular continuum emission at 180 nm (FWHM~ 40 nm).

The filters were adapted on a wheel which is placed inside a vacuum sealed cylindrical container. The wheel can be externally rotated via vacuum feedthroughs. In order to compensate any potential error related to offsets of the circuit, the wheel also included an aluminium plate to completely block the incident light. The intensity of the photodiode current, was measured with the acquired background signal as reference. Another important function of the aluminium plate is to protect the photodiode from the long-term degrading effect of VUV light when measurements are not realized. The irradiance meter was adapted on Prometheus I as presented in Figure 3.17. Due to an iris adapted right in front of the photodiode, the light is collected from a conic line of sight, with an included angle of 4.6°.

The filters were used to measure the intensity of the VUV spectral components in the light emitted from the bulk of the plasma. A typical spectrum from this plasma region is presented in Figure 3.19. The plasma was acquired for two different values of the entrance and exit slit of the monochromator. In the first case 50 μm slits are used to register the entire VUV spectrum, while in the second case the width of the slit was increased to 150 μm to amplify molecular emissions (Lyman-band and molecular continuum).

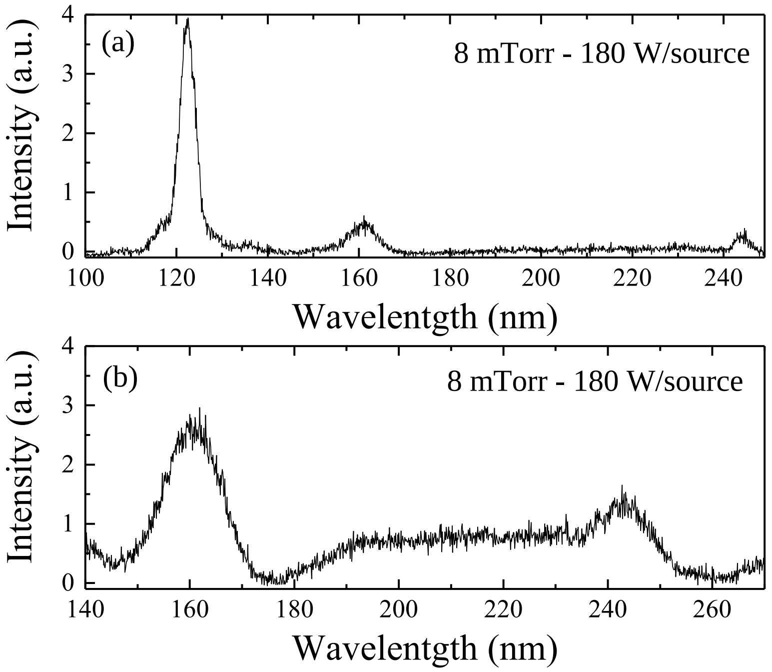

Figure 3.19. VUV emission spectra from the bulk plasma of Prometheus I. The monochromator is looking in a line of sight 65 mm bellow the mid-plane of the magnets. (a) Spectrum acquired with entrance and exit slits of 50 μm. (b) Spectrum acquired with entrance and exit slits of 150 μm.

The spectrum of the light that is emitted around Lyman-α from the bulk of the plasma (65 mm bellow the midplane of ECR zones), is presented in Figure 3.20a. Due to the low resolution of the spectroscopy system, the spectrum of Werner band is quite broadened. This allows to approximate the Werner band spectrum with a Gaussian function in order to deconvolute it from the Lyman-α emission. The intensity of the two components as a function of power is presented in Figure 3.20b. The intensity of Werner band is about an order of magnitude lower that the intensity of Lyman-α, which dominates the spectrum around 120 nm. This fact simplifies diagnostics, since the photodiode current measured with the Lyman-α filter is mostly attributed to Lyman-α emission, while the contribution of Werner band is negligible. This will prove to be convenient for the interpretation of the results in Chapter 4.

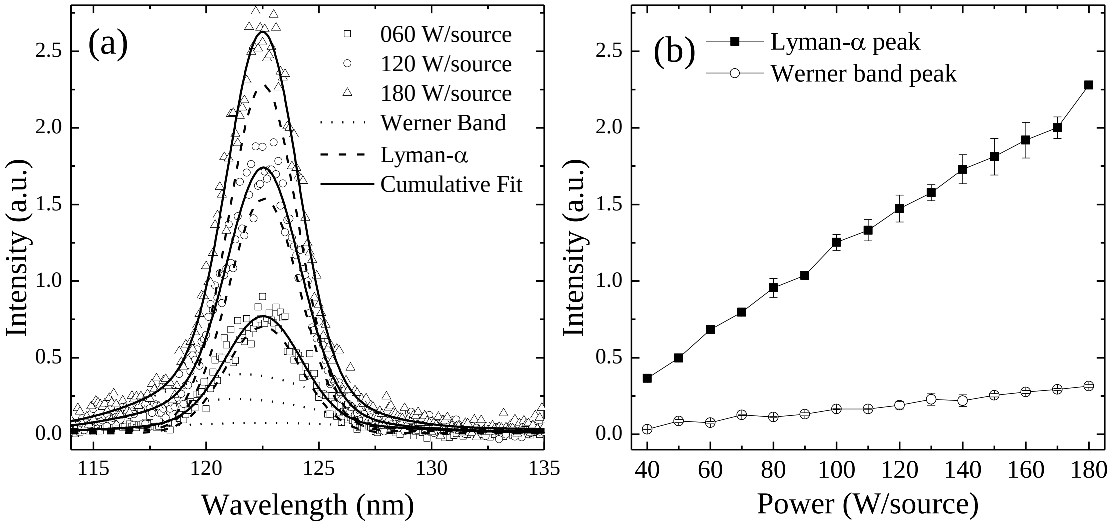

Figure 3.20. (a) Deconvolution of Lyman-α line form Werner band for 4 mTorr and three indicative powers and (b) pressure dependence of Lyman-α and Werner band intensities.

The two measuring systems (monochromator and irradiance meter) are not calibrated and the derived results are always in arbitrary units. Even the photodiode currents which are reported in pA, are in fact in arbitrary units, since the absolute response of the irradiance meter is unknown. To evaluate whether both systems give similar results the intensity of each component of the spectrum from the bulk of the plasma is plotted as a function of microwave power. The comparison of the two systems is made on the basis of the shape of this function and is presented in Figure 3.21. For the case of Lyman-α (Figure 3.21), the irradiance meter measurement is compared with the Lyman-a contribution calculated in Figure 3.20, and in the case of Lyman band and molecular continuum emissions, with the integral of the VUV spectrum in the emission regions (145-170 nm for Lyman band and 180-230 for molecular continuum).

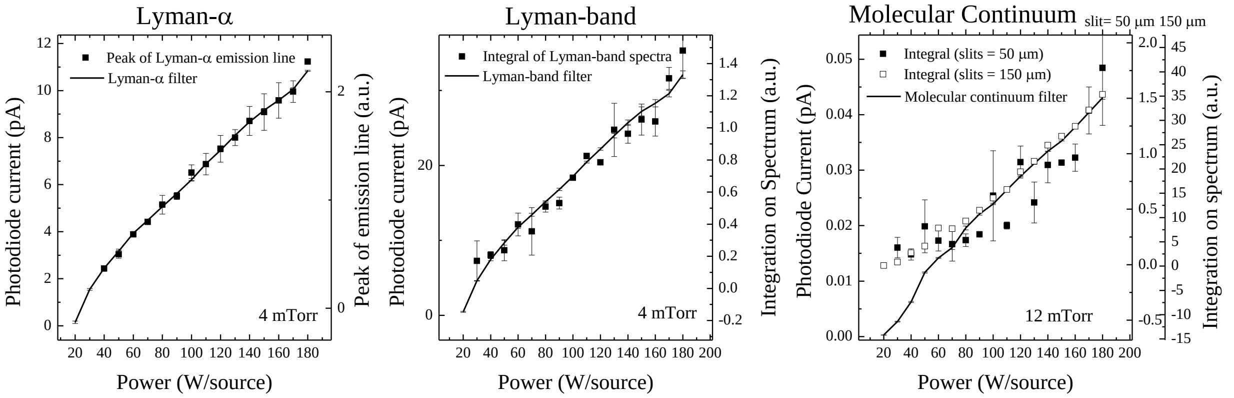

Figure 3.21. Comparison between the two different ways of measuring the total contribution of each spectral component. The lines correspond to measurement with the filters while the scatter plots correspond to measurements by integration of the VUV spectrum.

In the case of the Lyman-α and Lyman-band emissions, the measurements from the two systems have quite similar evolution. In the case of molecular continuum, problems related to low signal to noise ratio become evident. For this reason, the integral on the spectrum acquired with the 150 μm slit is also presented in Figure 3.21c. By doing so, the evolution for high power becomes similar while for low power the intensity of remains comparable to noise. It is evident that the irradiance meter is more immune to noise and is capable of making measurements even when the light intensity is relatively low, which is the case for the emission from the bulk of the plasma. This becomes more evident in the measurement of the molecular continuum intensity which in many cases becomes comparable to the noise level of the spectrometer.

3.2 Negative ion source ROSAE III

The source ROSAE III is installed in the Laboratory of Subatomic Physics and Cosmology (CNRS) in Grenoble (France). It is designed in order to investigate how the recombinative desorption, leading to the formation of vibrationally excited molecules, may assist hydrogen negative ion production in ECR plasmas. In order to study the effect of various materials, the operation should rely on a practical sample size, i.e. small enough to reduce the cost. The problem in this case is how to differentiate the formation of vibrational states that happens on the surface of the sample from the formation on the rest of the chamber walls and in the volume of the plasma. To make this distinction one of the two mechanisms needs to become dominant so that the other can be disregarded. In the case of recombinative desorption studies, the volume production needs to be suppressed. The concept of this study is depicted in Figure 3.22. The goal is to avoid vibrational excitation in the bulk of the plasma and on the surface of the chamber and increase as much as possible the vibrational excitation on the surface of the studied material.

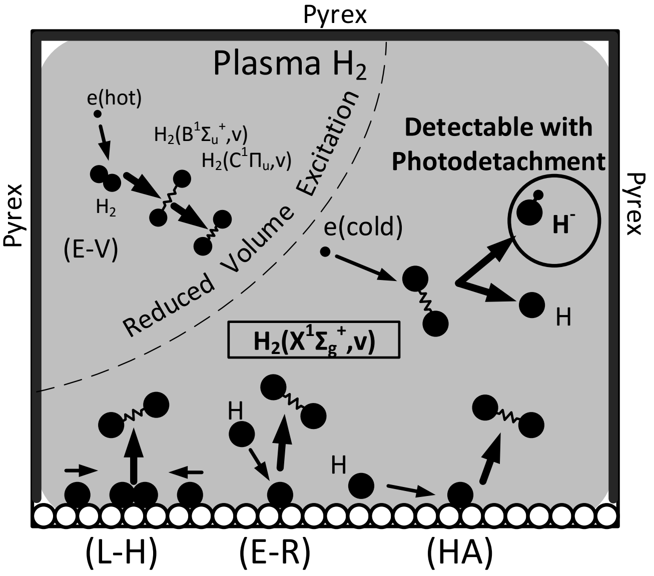

Figure 3.22. Concept of the source ROSAE III. The production of vibrationally excited molecules is limited as much as possible to the recombinative desorption on the surface of the studied material. L-H, E-R and HA refer respectively to the Langmuir-Hinshelwood, Eley-Rideal and hot atom desorption mechanisms that are presented in Section 2.2.2.

The experimental setup of the source ROSAE III is presented in Figure 3.23. It is driven by the same kind of dipolar sources as Prometheus I [67]. The power from a single microwave generator (up to 1.2 kW), is divided into four equal parts and supplied to the dipolar sources. The sources are cooled with continuous flow of water. A copper tube is welded on the cylindrical stainless steel chamber of the source. Water flows in the tube to keep the temperature of the chamber wall to relatively low levels (bellow room temperature). The Pyrex that covers the internal surface of the chamber is 5 mm thick and in direct contact with the chamber walls, in order to maximize its cooling capacity. The height of the chamber is 214 mm and its diameter is 152 mm. The pumping of the source is realized with a turbo-molecular pump (50 l/s) adapted at the bottom of the source and the base pressure is in the order of 10^{-6} Torr. The plasma is sustained in pure hydrogen in a pressure that was accurately monitored with a Baratron pressure transducer.

The source ROSAE III is equipped with electrostatic probe, photodetachment and optical emission spectroscopy (UV-Visible) diagnostic techniques. Electrostatic probe measurements are realized with a commercial automated acquisition system (SmartProbe, Scientific Systems). The probe has similar construction with the probe used for Prometheus I. The tip of the probe is an L-bent tungsten wire 0.35 mm in diameter and with a total length of 15 mm. It is positioned 90 mm below the midplane of the ECR sources. For the photodetachment technique a Q-switched Nd:YAG laser is used. For the decoupling of the AC photodetachment signal the capacitive decoupling circuit, presented in Figure 3.23, was designed as proposed in [153]. The calibration procedure for the photodetachment technique is similar to that of Prometheus I. Optical emission spectroscopy measurements are realized in the same height with the probe, with a monochromator (THR 1000) with 1 m focal length. Light is collected by a collimator and driven into the monochromator by an optical fiber. Spectroscopy measurements are calibrated and used for the determination of the dissociation degree, as presented in Section 3.1.3.

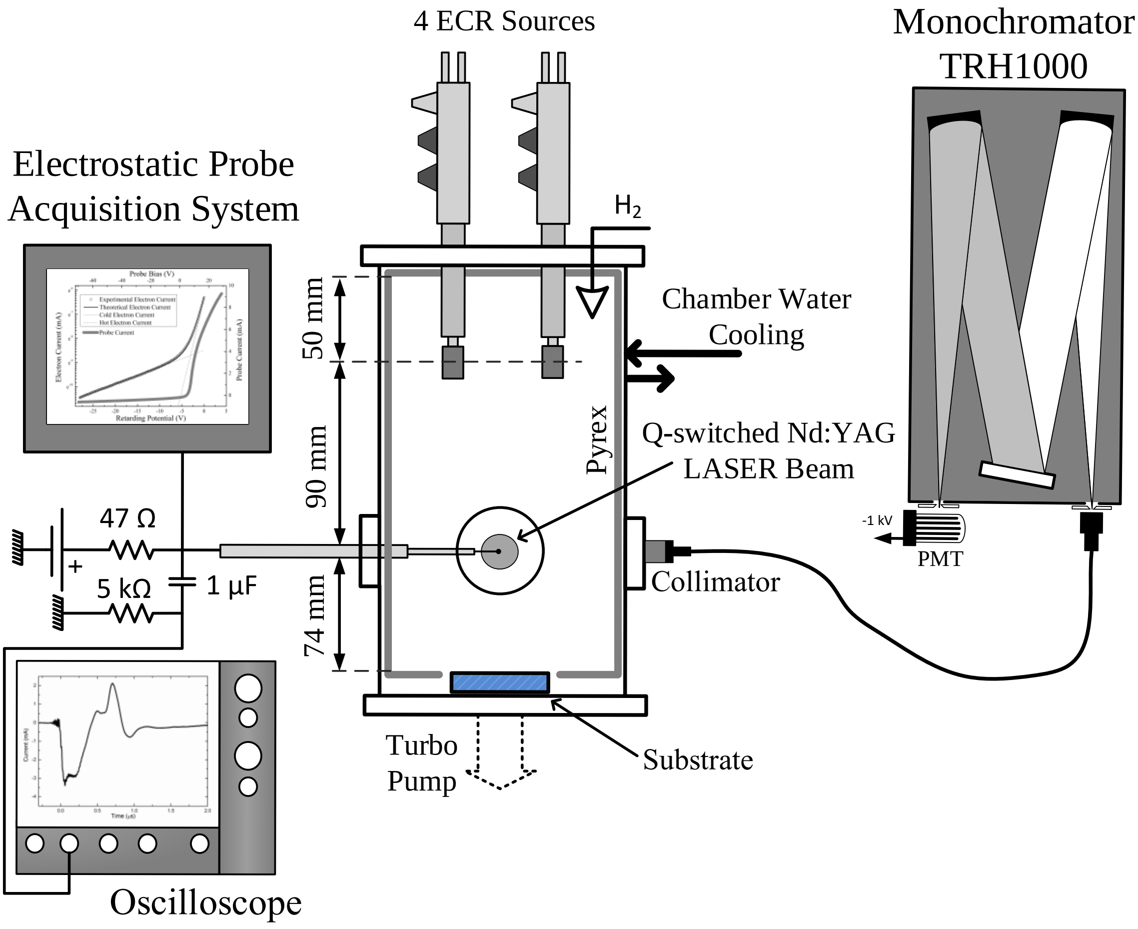

Figure 3.23. Experimental setup ROSAE III.

The volume of ROSAE III is considerably reduced compared to Prometheus I. The total volume of the source Prometheus I is 13.82 lt while the total volume of the source ROSAE III is only 3.8 lt. Additionally, most of the internal part of the chamber is covered with Pyrex. A sample, 50 mm in diameter, is positioned at the bottom of the chamber in order to study the effect of its material to negative ion production. The experimental setup ROSAE I is depicted in Figure 3.24.

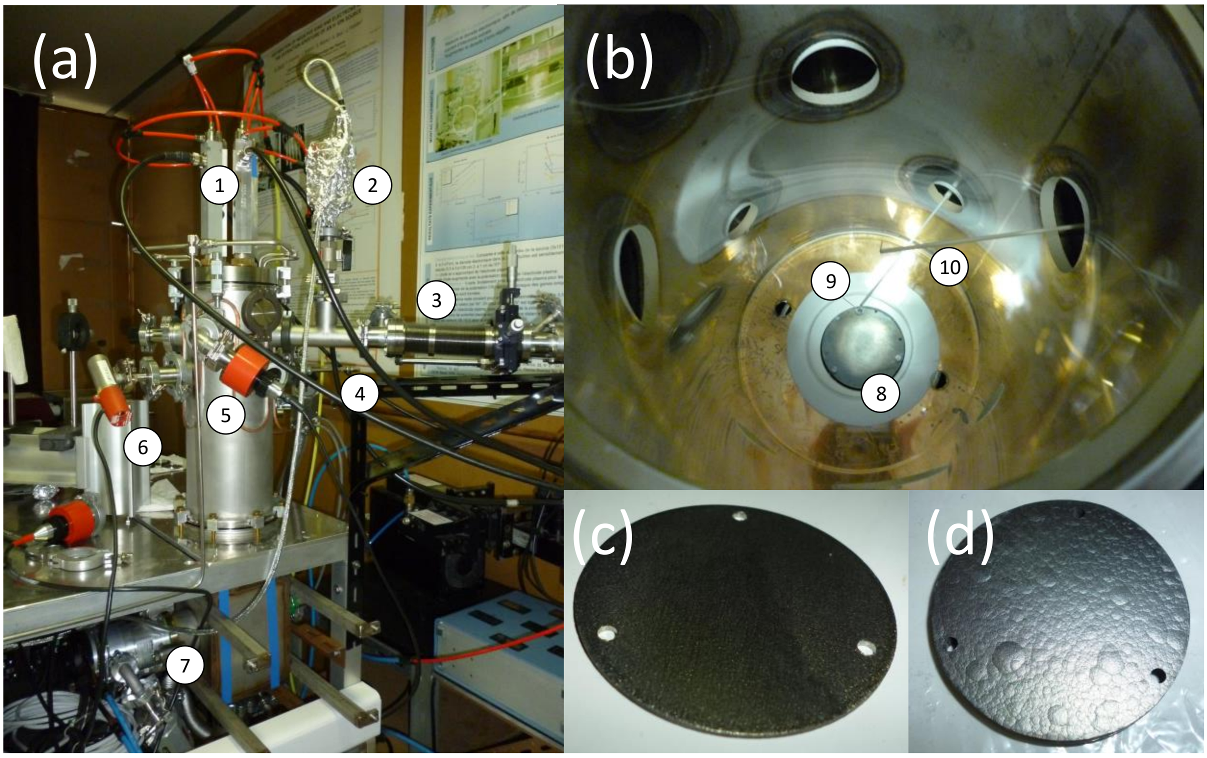

Figure 3.24. Experimental setup of ROSAE III. (a) The source ROSAE III (b) The internal part of the chamber covered with Pyrex (c) Yttrium sample (d) Highly oriented pyrolytic graphite (HOPG) sample. Numbered items: 1. Dipolar sources and water cooling system 2. Baratron for pressure monitoring 3. Electrostatic probe 4. Electrostatic probe used of EEDF and laser photodetachment measurements 5 and 6. Pirani gauges for base pressure monitoring 7. Pumping system 8. Inox sample positioned at the bottom of the chamber 9. Tip of probe (4). 10. Tip of probe (3).

To clarify how this configuration relatively amplifies vibrational heating through recombinative desorption on the surface of the studied material, the vibrational excitation mechanisms must be discussed. A simplified expression for the formation rate of vibrationally excited molecules in the volume of the plasma through EV excitation (volume production of vibrational states) is given by the equation:

$$\left.\frac{dn_v}{dt}\right|_{EV} = K_{EV}\left(T_{vib}, T_e\right) n_e n_{H_2} \tag{3.6}$$

where $K_{EV}(T_{vib,}\ T_e)$ is an effective rate coefficient that accounts for the vibrational distribution, T_{vib} is the vibrational temperature and T_e is the electron temperature. n_e is the density of electrons and n_{H_2} is the total density of molecules in their ground state. On the other hand, the recombination rate of atoms in the surface of the material, is given by the equation [39]:

$$\left.\frac{dn_v}{dt}\right|_{RD} = \frac{1}{4} n_H v_H \frac{A_{ch}\gamma_H}{V_{ch}} = \frac{1}{4} n_H v_H \frac{A_{Py}\gamma_{H,Py} + A_s\gamma_{H,s}}{V_{ch}} \cong \frac{1}{4} n_H v_H \frac{A_s\gamma_{H,s}}{V_{ch}} \tag{3.7}$$

where n_H is the density of atoms, v_H their thermal velocity, γ_H the probability of surface recombination on the chamber walls. A_{ch} is the total area of the chamber walls and V_{ch} is the volume of the source. When two different materials are used for the chamber walls, as in the case of ROSAE III, the nominator $A_{ch}\gamma_H$ is replaced to account for the two different contributions. A_{Py} and $\gamma_{H,Py}$ refer to the surface area and the recombination coefficient of the Pyrex and A_s and $\gamma_{H,s}$ refer to the surface area and the recombination coefficient of the sample of the studied material.

Pyrex is a material (along with quartz) with a recombination coefficient that is greatly affected by the material temperature [165]. By keeping the material below room temperature with water cooling the recombination coefficient is reduced to the order of 10^{-3}, while for typical plasma chamber temperatures about 350-400 K the recombination might reach the order of 10^{-2}. Metals like stainless steel have a recombination coefficient in the order of 10^{-1} [30]. By covering the chamber walls with Pyrex surface production of vibrational states is limited to the studied material.

The ratio $\mathrm{R}_{\mathrm{EV}}^{\mathrm{RD}}$ between the two sources of vibrational excitation (Equations (3.6) and (3.7)) is given by the equation:

$$\begin{aligned} R_{EV}^{RD} &= \frac{dn_v/dt|_{RD}}{dn_v/dt|_{EV}} = \frac{n_H v_H}{4K_{EV}\left(T_{vib},T_e\right)n_e n_{H_2}} \frac{A_{ch}\gamma_H}{V_{ch}} \\ &= \frac{n_H v_H}{4K_{EV}\left(T_{vib},T_e\right)n_e n_{H_2}} \frac{A_{Py}\gamma_{H,Py} + A_s\gamma_{H,s}}{V_{ch}} = \frac{n_H v_H}{4K_{EV}\left(T_{vib},T_e\right)n_e n_{H_2}} \frac{A_s\gamma_{H,s}}{V_{ch}} \end{aligned} \tag{3.8}$$

In ROSAE III, this ratio is increased in two different ways. The first refers to the reduction of the volume of the sources (compared to Prometheus I) which increases the last factor of Equation (3.8). The second refers to an increase of the atomic hydrogen density, which will happen as a consequence of the lower recombination coefficient on the chamber walls. The results obtained from the source ROSAE III, are presented in Section 4.4.

3.3 Source SCHEME

The initial objective of SCHEME is to create the framework for probing individually the ro-vibrational levels of ground state H_2 molecules by means of induced fluorescence and absorption spectroscopy in the VUV range, using synchrotron radiation. The development of such a diagnostic tool would provide a more accessible alternative to complicated and expensive laser systems with variable wavelength in the VUV spectral range. The long term objective of the project is to study the vibrational distribution of molecules that are produced via recombinative desorption on surfaces of various materials.

For the purpose of this measurement, a timeslot was assigned in the beamline DESIRS [166] (Dichroïsme Et Spectroscopie par Interaction avec le Rayonnement Synchrotron) of Synchrotron Soleil (French national synchrotron facility). DESIRS is an undulator-based beamline covering the VUV range (5-40 eV or 30-250 nm). By using a 200 grooves/mm grating the beamline light is monochromatized. The spectral resolution of the monochromatic beam is 720 mÅ and the photon flux in the order of 10^{13}-10^{14} photons/s.

The experimental setup is presented in Figure 3.25. The source SCHEME is adapted on the monochromatized branch of the beamline DESIRS. The end of the beamline is branched on a small chamber separated by the main chamber by an MgF_2 viewport. This small chamber is individually pumped and sealed with copper flanges, in order to reach the necessary vacuum for the beamline (~10^{-7} Torr). This small chamber also houses a tuning fork which is used for the chopping of the beam for phase sensitive measurements. The frequency of the chopper is constant and equal to 130 Hz. Separating the beamline from the experimental setup, allows the source to work on higher pressures that are relevant for negative ion production.

The source is mainly pumped by a turbomolecular pump of 600 l/s. Two additional turbomolecular pumps of 50 l/s are adapted on the central part and on the auxiliary chamber 1 but, for clarity, are not presented on the schematic. The base pressure of the system is in the order of 10^{-6} Torr. Krypton and hydrogen are introduced in the source with a mass flow meter. The pressure is accurately monitored with an absolute pressure transducer (Baratron).

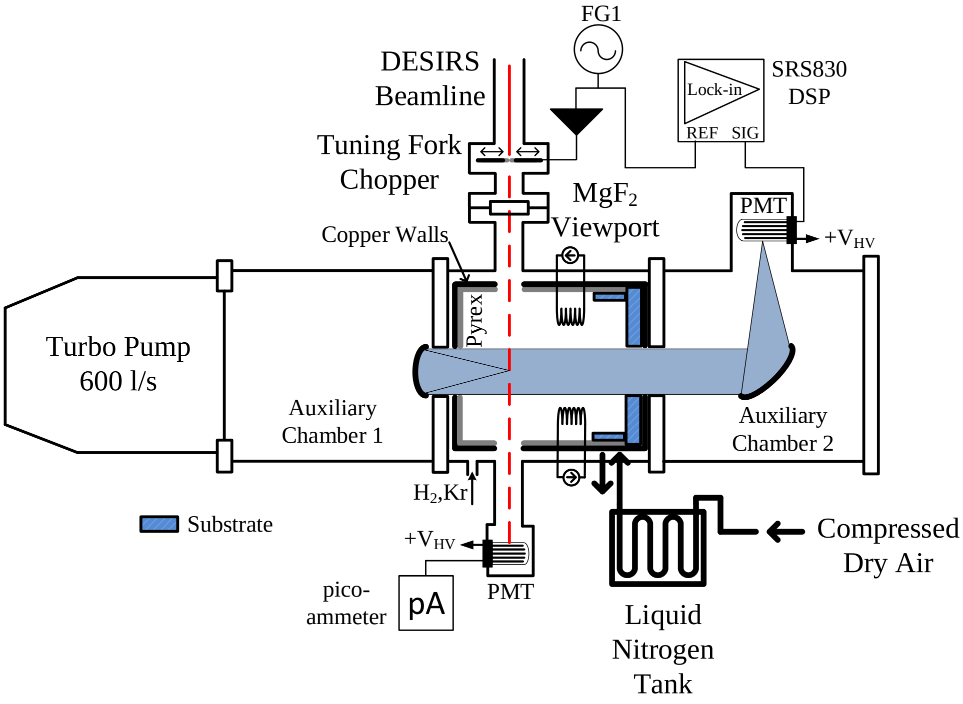

Figure 3.25. SCHEME experimental setup adapted on the DESIRS beamline of Synchrotron Soleil.

For the absorption spectroscopy measurement a solar blind PMT (R1259) was used at the opposite site of the beam entrance. The PMT current was measured with a pico-ammeter and the spectrum was registered by the beamline computer. For the fluorescence spectroscopy measurement, two mirrors 50.8 mm in diameter, were used to collect as much light as possible. One mirror was concave while the other was off-axis parabolic. The fluorescence light is focused on another solar-blind PMT (R10825), with its output connected on a lock-in amplifier (Stanford Research SR830). The reference input of the lock-in amplifier is connected to the 130 Hz driving signal of the tuning fork. The output of the lock-in amplifier is connected in an analog input of the beamline acquisition system and registered by the beamline computer.

Three hot filaments are used for dissociating molecules [167]. The temperature of these filaments is monitored by voltage/current measurements for the determination of their electrical resistivity. Based on trials, in order to avoid contamination from tungsten evaporation, the temperature of the filaments should not be higher than 2500 K. The central part of the chamber is cylindrical with a diameter of 160 mm. The internal part of the main chamber is covered with Pyrex. Just like in the case of ROSAE III, the purpose of the Pyrex is to limit recombinative desorption on the surface of the studied material. The Pyrex tube has an internal diameter of 140 mm and an internal length of 100 mm. The substrate of the material was adapted at one side of the chamber as presented in Figure 3.25. In total in consists of two parts: a disk 140 mm in diameter, covering completely one side of the cylinder and a ribbon adapted around the edge of the cylinder with a width of 35 mm.

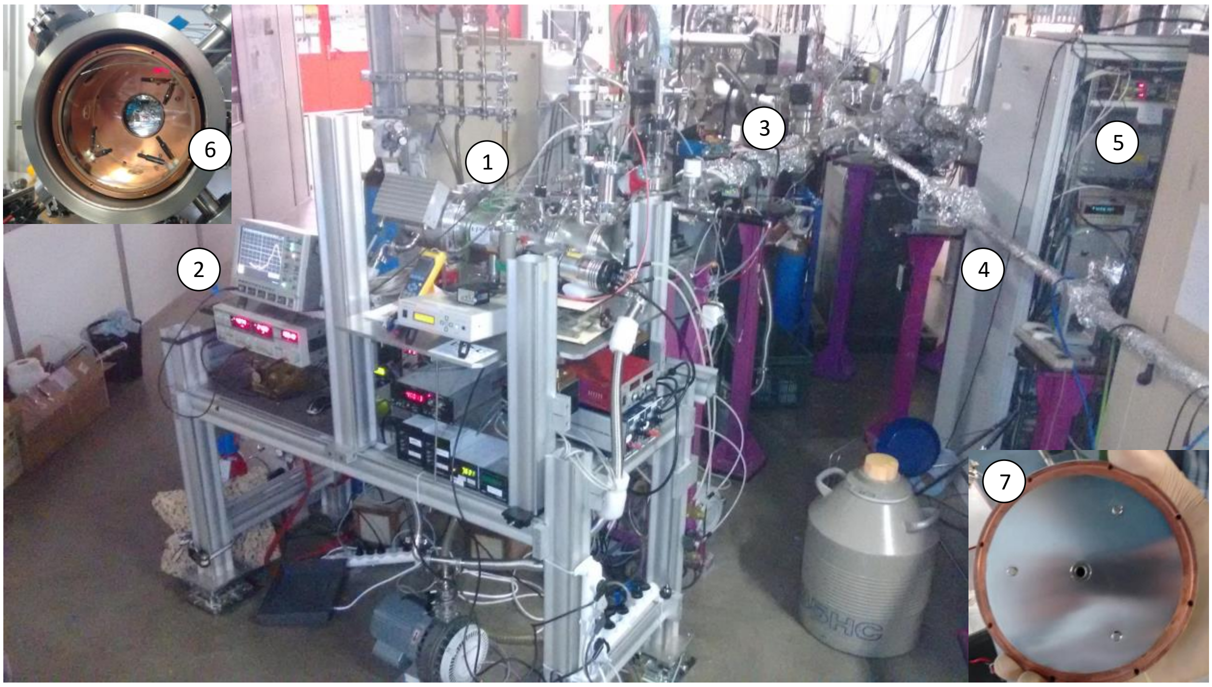

Figure 3.26. Experimental setup SCHEME adapted on the DESIRS beamline of Synchrotron Soleil. 1. Source SCHEME 2. Acquisition system for induced fluorescence 3. Monochromatized beamline 4. Beamline DESIRS 5. Signal acquisition system of beamline 6. (upper inset) Internal view of the source SCHEME 7. (lower inset) Stainless steel sample that adapts on the copper cylinder of (6).

The Pyrex cylinder and the substrate are adapted inside a copper cylinder. A copper tube is welded on the copper cylinder as a heat exchanger. Cooling of the copper is realized by continuous flow of dry air that has previously passed through a heat exchanger submerged in liquid Nitrogen (LN_2). The temperature of the copper cylinder is monitored in two places by means of thermocouples. The temperatures reached can be quite low, however, for the purposes of the campaign it was kept close to room temperature. The entire copper cylinder is under vacuum to avoid ice formation on its surface. The LN_2 cooling is necessary because of the intense heat that is radiated by the filaments. By keeping the Pyrex close to room temperature the recombination coefficient γ is in the order of 4×10^{-3} [165] while for metallic surfaces is in the order of 10^{-1} [168].

Initially measurements where realized in krypton which, as an atomic gas, has a well-defined atomic density and can be later used to calibrate measurements performed with hydrogen. The krypton transition at 10.032 eV (123.584 nm) is used for the simultaneous acquisition of the absorption and the fluorescence signal. These results confirm the good operation of the optical setup and the measuring system. The results obtained with the source SCHEME, are presented in Section 4.4.

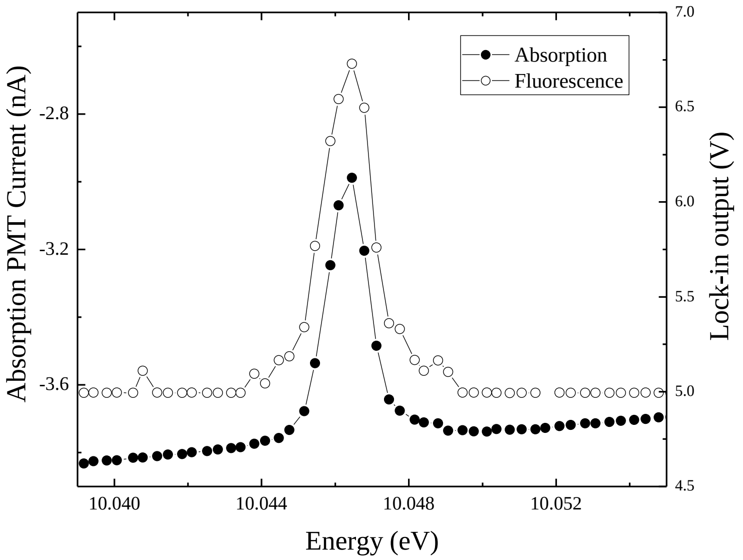

Figure 3.27. Simultaneous absorption and fluorescence measurement performed with krypton. The pressure is 10 mTorr.

Synopsis

A descriptive diagram of all the experimental setups used in this work is presented in Figure 3.28. For each setup all the installed diagnostic techniques are listed.

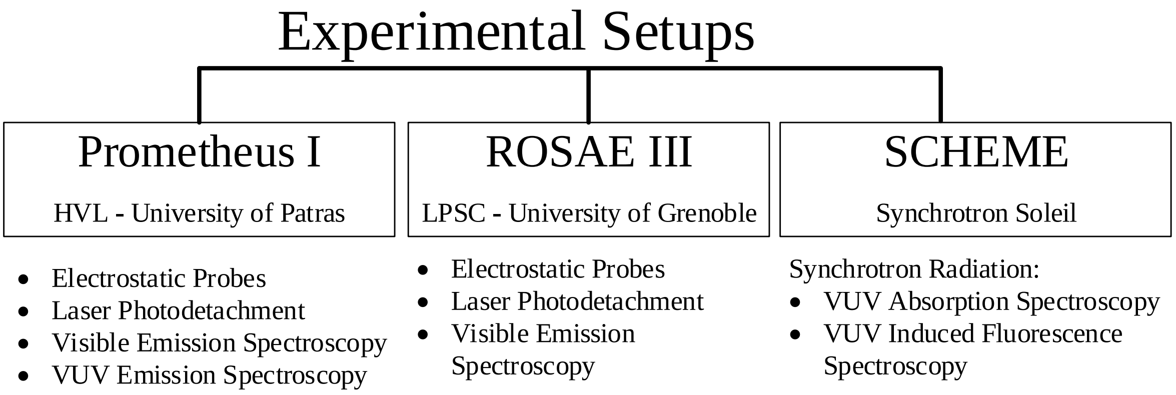

Figure 3.28. Descriptive diagram of all the experimental setups used in this work and the respective diagnostic techniques.

The two ion sources (Prometheus I and ROSAE III) are driven by identical ECR sources. However, as explained in this chapter, they are designed to study different phenomena. Results obtained with Prometheus I are presented in Chapter 4, with the exception of Section 4.4, which presents the results obtained with ROSAE III and SCHEME.

Chapter 4. Results and Discussion

Abstract

In this chapter results are presented and discussed, starting with an overview of the operation of the source Prometheus I. A wide parametric study with electrostatic probes and laser photodetachment, for three different configurations, allows the characterization of this source in terms of negative ion production and basic plasma parameters. For the first configuration, visible emission spectroscopy measurements are also realized, in order to determine the degree of dissociation and the gas temperature. Then, the mechanisms that produce negative ions are considered, starting with the assessment of the contribution of a recently proposed mechanism (neutral resonant ionization). However, the widely accepted formation process, which is dissociative attachment to vibrationally excited molecules, is confirmed to dominate the production of negative ions. After this confirmation, the efficiency of dissociative attachment is investigated by looking into the processes that create the two necessary reactants for negative ion production, i.e. vibrationally excited molecules and electrons. The formation of vibrational states on the materials that face the plasma is studied in two specially designed sources (ROSAE III and SCHEME). On the other hand, vibrational heating in the volume of the plasma is studied by vacuum-ultraviolet emission spectroscopy in the source Prometheus I. Finally, the factors that limit negative ion production in the studied ECR plasmas are identified and discussed.

4.1 Overview

The operation of a single dipolar ECR source is presented in Figure 4.1, along with the iso-B contour diagram of its magnetic field. The plasma appears to be confined in the luminous regions in the vicinity of the magnets, which roughly correspond to the regions indicated in Figure 4.1a, where the magnetic field is equal to 875 G. In this region the electron gyrofrequency is equal to the imposed frequency of the electric field (2.45 GHz). Interestingly, a second luminous region appears, which is possibly related with another dissipative mechanism of microwave power [169]. Measurements realized in a dedicated experimental setup in LPSC, in argon discharge, demonstrate that this region corresponds to a local increase of the hot electron density. However, the exact mechanisms which couple the microwave power with the plasma are still under study.

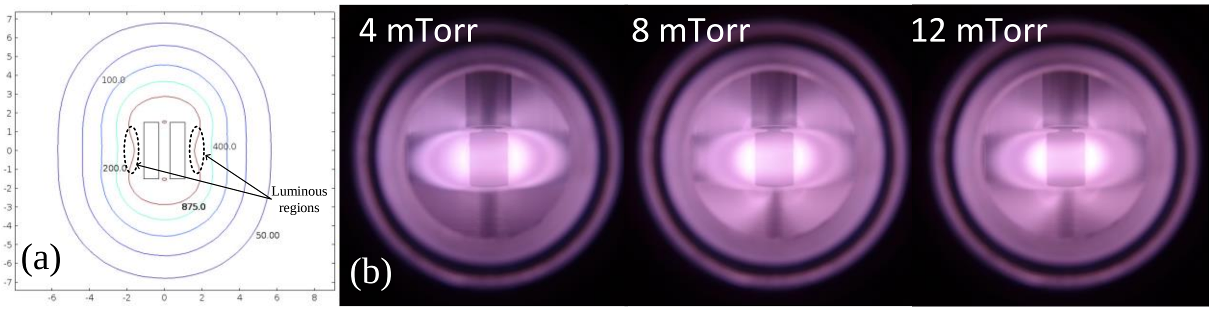

Figure 4.1. (a) Magnetic field of a single source (b) Operation of a single source for nominal power (180 W/source) and three indicative pressures.

The used dipolar sources, appear to have different modes of operation. A characteristic case is depicted in Figure 4.2. A single source is operated in 4 mTorr of pure hydrogen. For low power (40 W) the discharge is limited in the ECR luminous region in the vicinity of the magnet (indicated in Figure 4.1a). As more power is injected, this region expands and has a luminosity that appears to be homogeneous. However, when the injected power is increased from 95 to 96 W, an abrupt mode transition creates a plasma with a completely different spatial distribution.

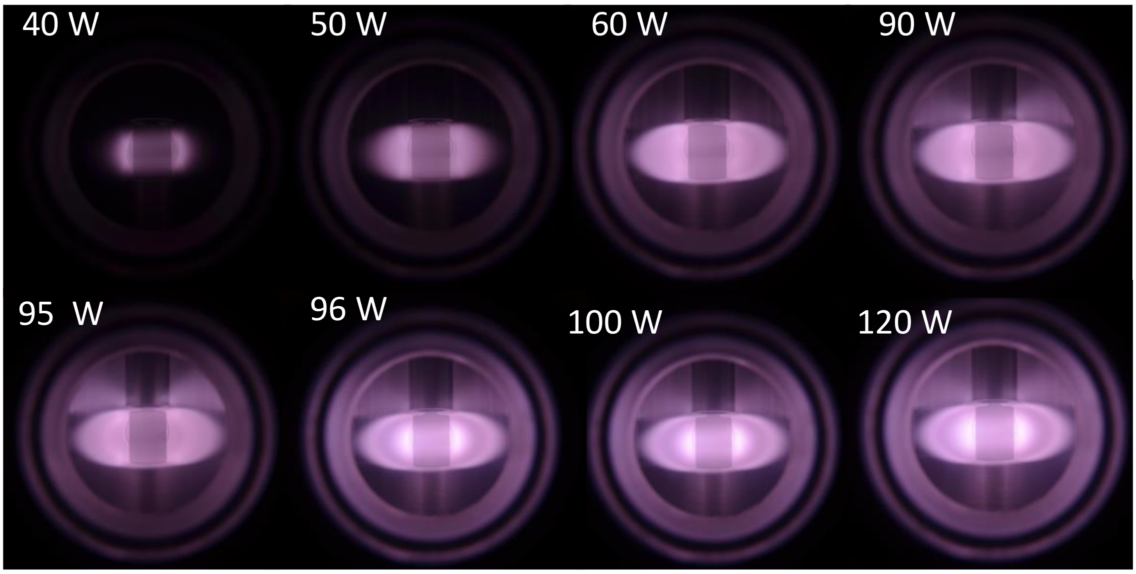

Figure 4.2. Power injection in a single dipolar source working in 4 mTorr of pure H_2.

The VUV spectrum of the plasma depicted in Figure 4.2, for the cases of 90 and 100 W is presented in Figure 4.3. Evidently, the second mode (100 W) is related with a considerably higher intensity of the spectrum which, since the pressure is the same, can be attributed to a denser or hotter electron population. It appears that in this mode of operation, the coupling of microwave power to the plasma is much more efficient. The mode transition depicted in Figure 4.2, is an extreme case which is observed only when a single source is supplied with power. In the results presented in the rest of the chapter, less abrupt mode transitions are responsible for some variations of the electron density and temperature.

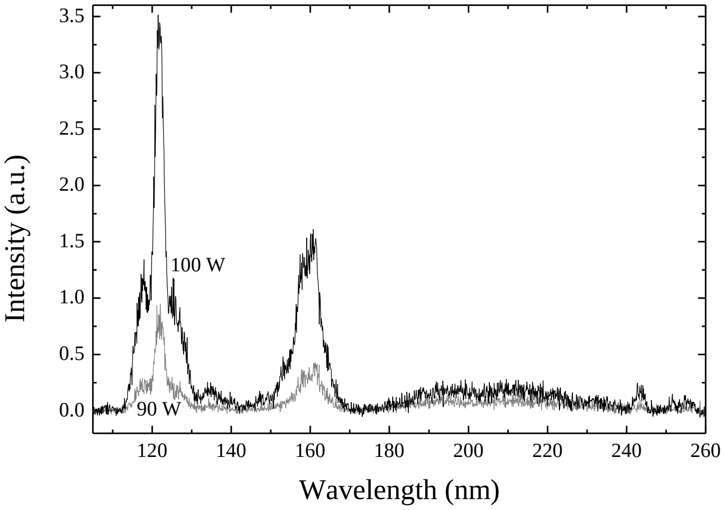

Figure 4.3. VUV spectrum of the two modes for powers of 90 and 100 W. For both cases, the spectrometer looks in the ECR zones, 3 mm above the mid-plane of the magnets. The spectra where acquired with entrance and exit slits of 20 μm. Details about the VUV spectrometer can be found in Section 3.1.4.

This work concerns the bulk plasma of Prometheus I, where negative ion production is mainly taking place. In the rest of this chapter, the closest distance between the studied area and the ECR zones is 65 mm. The operation of the source in this configuration is depicted in Figure 4.4.

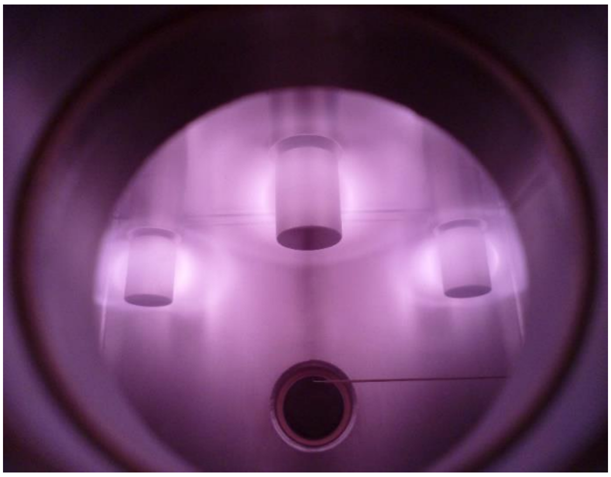

Figure 4.4. Operation of the source for measurements in the bulk plasma. The distance between the probe and the ECR zones is 65 mm. The filling gas pressure is 10 mTorr and each source is supplied with 180 W of microwave power.

Away from the ECR zones, with few exceptions, the EEDF is bi-Maxwellian consisting of cold and hot electrons. Two indicative cases are presented in Figure 4.5. Due to their low energies, it is mostly cold electrons that are directly related with negative ion production through the dissociative attachment process (see Chapter 2). On the other hand, hot electrons constitute only 1-5% of the total electron density. Nevertheless, their high temperature, being approximately 15 eV, makes them very important. Electron impact processes such as ionization and excitation have considerably high energy thresholds (>10 eV in most cases for hydrogen [78]). Hot electrons, having an important part of their population above these thresholds, are mainly responsible for most of the excitation and ionization processes.

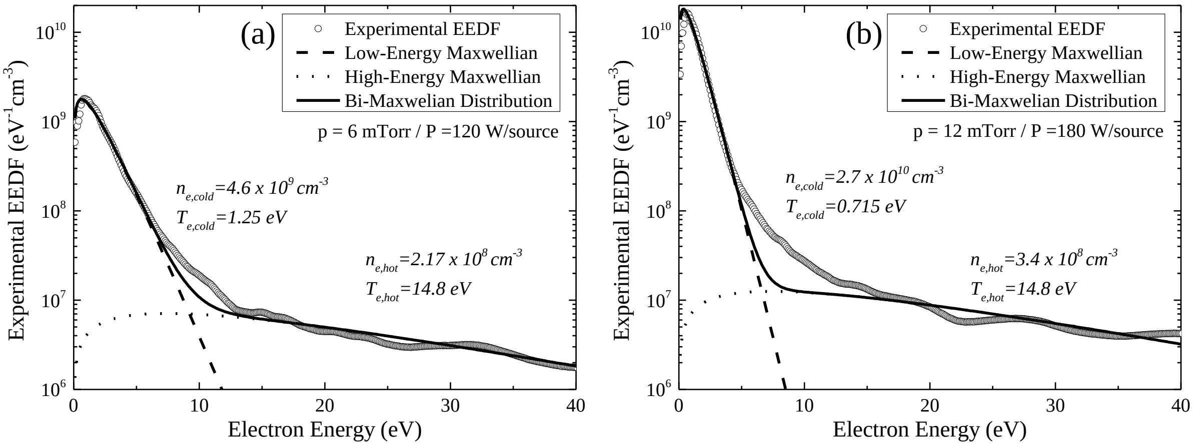

Figure 4.5. Indicative EEDF for (a) a pressure of 6 mTorr and a power of 120 W/source and (b) a pressure of 12 mTorr and a power of 180 W/source.

These EEDFs indicate that higher pressures, are related with a main body of electrons that is colder and denser, and consequently more favorable for negative ions production through dissociative attachment (see Section 2.1.1). In the next section, a wide parametric study is realized for three different configurations. Its purpose is to investigate the production of negative ions for the entire parametric space of the source and reveal optimum operating conditions.

4.2 Characterization of the source Prometheus I

The characterization of the source Prometheus I was realized, by means of electrostatic probes, laser photodetachment and optical emission spectroscopy in the visible spectral range, for the three different configurations that are depicted in the Figure 4.6. A detailed description of the source and the used diagnostics can be found in Section 3.1. For each configuration, the sources are in a different location, changing not only the distance between the ECR zones and the probe, but also the effective volume of the discharge.

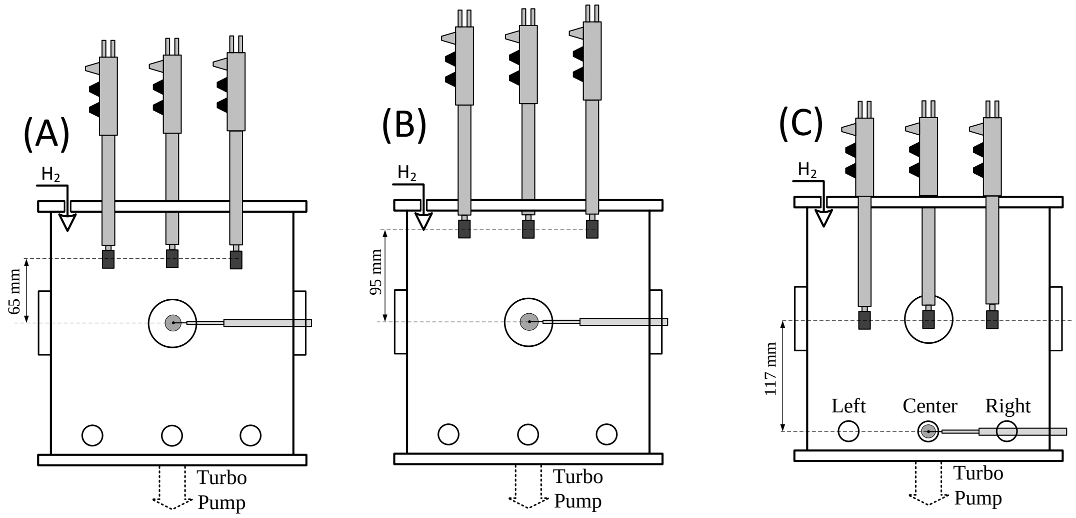

Figure 4.6. The three different configurations that are used for the characterization of the source.

In the configuration A (Figure 4.6A) the mid-plane of the ECR zones is placed 65 mm above the central viewport of the chamber, where diagnostics are performed. Spatially resolved measurements are realized in order to investigate the homogeneity of the plasma. The density of negative ions is measured only in the center of the chamber, with a series of probe and laser photodetachment measurements. Since this configuration is chosen for the studies presented in the next sections, it was also investigated by means of optical emission spectroscopy in the visible range. The gas temperature and the degree of dissociation were determined, using the diagnostic techniques presented in Section 3.1.3.

In configuration B (Figure 4.6B) the ECR zones are moved 30 mm higher and measurements are realized in the same position. In this case the plasma is studied by means of a) spatially resolved probe measurements as well as b) probe and laser photodetachment measurements in the center of the source.

In configuration C (Figure 4.6C) the mid-plane of the ECR zones is positioned 3 mm below the central viewport, while the probe is adapted on the lower part of the chamber. The distance between the mid-plane of the ECR zones and the probe is 117 mm. For this case probe and laser photodetachment measurements are realized in three different positions that correspond to three available viewports. The characterization of the source is summarized in Table 4-1.

Table 4-1. Studies realized in the frame of the source characterization

Configuration	Realized Studies	Page
A	Spatial Characterization (Probe)	71
	H^- Production (Probe + Photodetachment)	76
	OES Study	78
B	Spatial Characterization (Probe)	81
	H^- Production (Probe + Photodetachment)	86
C / Center	H^- Production (Probe + Photodetachment)	88
C / Right	H^- Production (Probe + Photodetachment)	90
C / Left	H^- Production (Probe + Photodetachment)	92

Spatially resolved measurements are realized with the probe scanning the source from side to side as depicted in Figure 4.7a. The magnetic flux density at the position of the probe, due to the magnets of the ECR sources, is presented in Figure 4.7b. This calculation has been realized with ACDC module of the COMSOL Multiphysics suite. The magnetic field for configuration C is quite negligible, since the probe is positioned far from the ECR magnets.

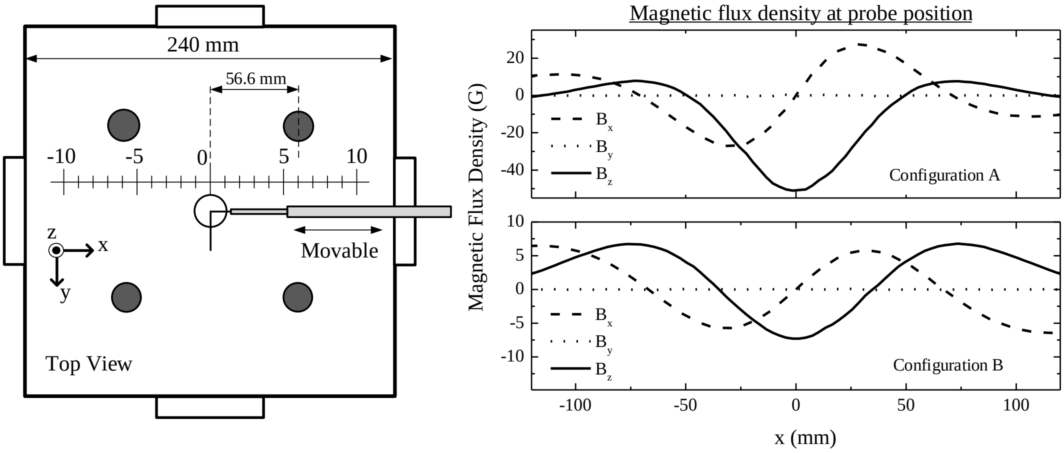

Figure 4.7. (a) Depiction of scanning zone of spatial characterization with electrostatic probes. (b) Magnetic flux density as a function of the position of the probe.

Since the y-component of magnetic flux density, which is parallel to the probe, is always zero, the magnetic field is always perpendicular to the probe. The maximum magnitude of magnetic flux density is found at the center of the chamber for the configuration A and is equal to 51 G. The measured electron temperature for Prometheus I for the entire parametric space, is never lower than 0.5 eV. Consequently, the resulting Larmor radius is always bigger than the radius of the probe, validating the use of non-magnetized probe theory (see Section 3.1.1 for more details).

The results presented in this section are interpreted assuming that negative ion production is mostly attributed to the dissociative attachment of cold electrons to vibrationally excited molecules. This mechanism, is the most widely accepted H^- negative ion formation process in volume sources and its dominance for the source Prometheus I is confirmed in Section 4.3.2.

4.2.1 Characterization of configuration A

4.2.1.1 Spatial characterization

The spatial characterization of the source is realized for three different values of power (60, 120 and 180 W/source) and for three different pressures (4, 8 and 12 mTorr). The obtained results are presented from Figure 4.9 to Figure 4.14. All graphs have the same scale so they can be visually compared. A parameter that is indicative of the effective electron temperature, is the difference between the floating and plasma potential [170]. In order to show this difference, the two potentials are plotted in the same figures. The densities and the temperatures of the hot electron populations are separately plotted.

For the case of 4 mTorr, the values of hot electron density and temperature appears to deviate appreciably outside the central region of the plasma and towards the chamber walls (e.g. Figure 4.10b and d). However, such an important change in temperature, should also be detectable by variations in the floating potential [170]. What actually happens can be explained by taking a closer look on the probe electron current, presented in Figure 4.8a. The deviation of the electron current from a bi-exponential form, invalidates the bi-Maxwellian approach for the EEDF and consequently, it invalidates the hot electron population measurements for 4 mTorr near the chamber walls. The EEDF that is acquired from the second derivative of the probe current, is very sensitive to variations and consequently, in the above case, has a sharp deviation from bi-Maxwellian, as presented in Figure 4.8a. Such deviations are easily detectable and they are used to roughly indicate the regions where the EEDF is accurately described by a bi-Maxwellian function.

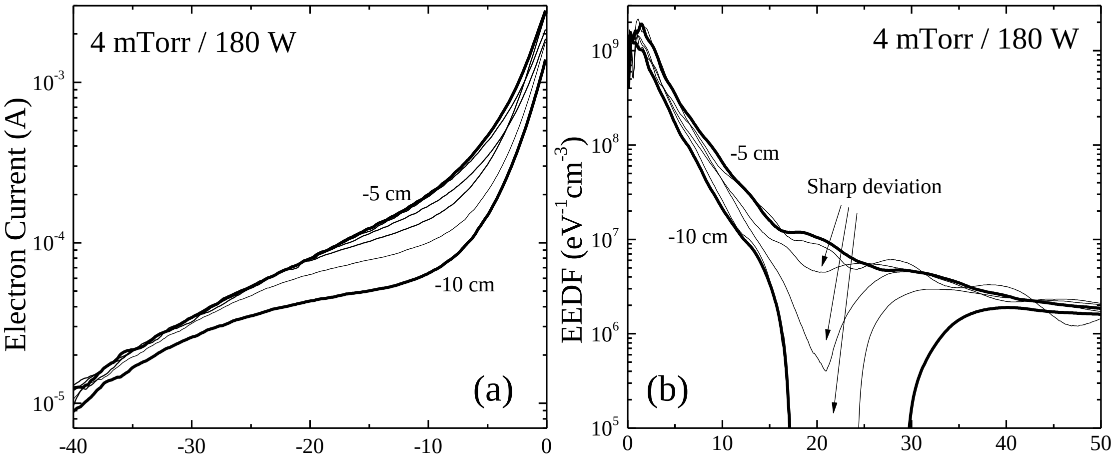

Figure 4.8. Demonstration of deviation from bi-Maxwellian EEDF near the chamber walls. (a) Deviation of the electron current. (b) Deviation of the EEDF that is calculated from the second derivative of the probe current.

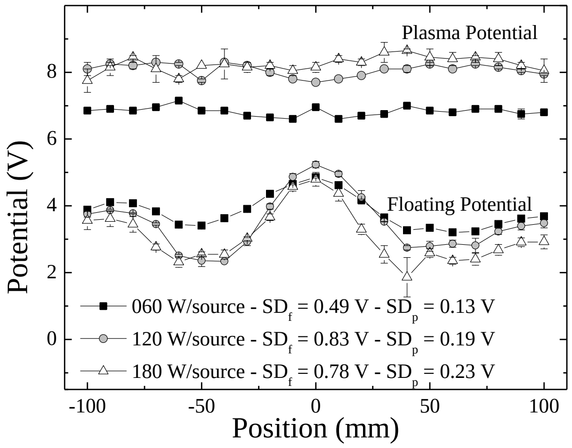

Figure 4.9. Spatial distribution of plasma and floating potential for a power of 4 mTorr. SD$_f$ and SD$_p$ refer to the standard deviation of floating and plasma potential respectively. Error bars are calculated from two series of measurements.

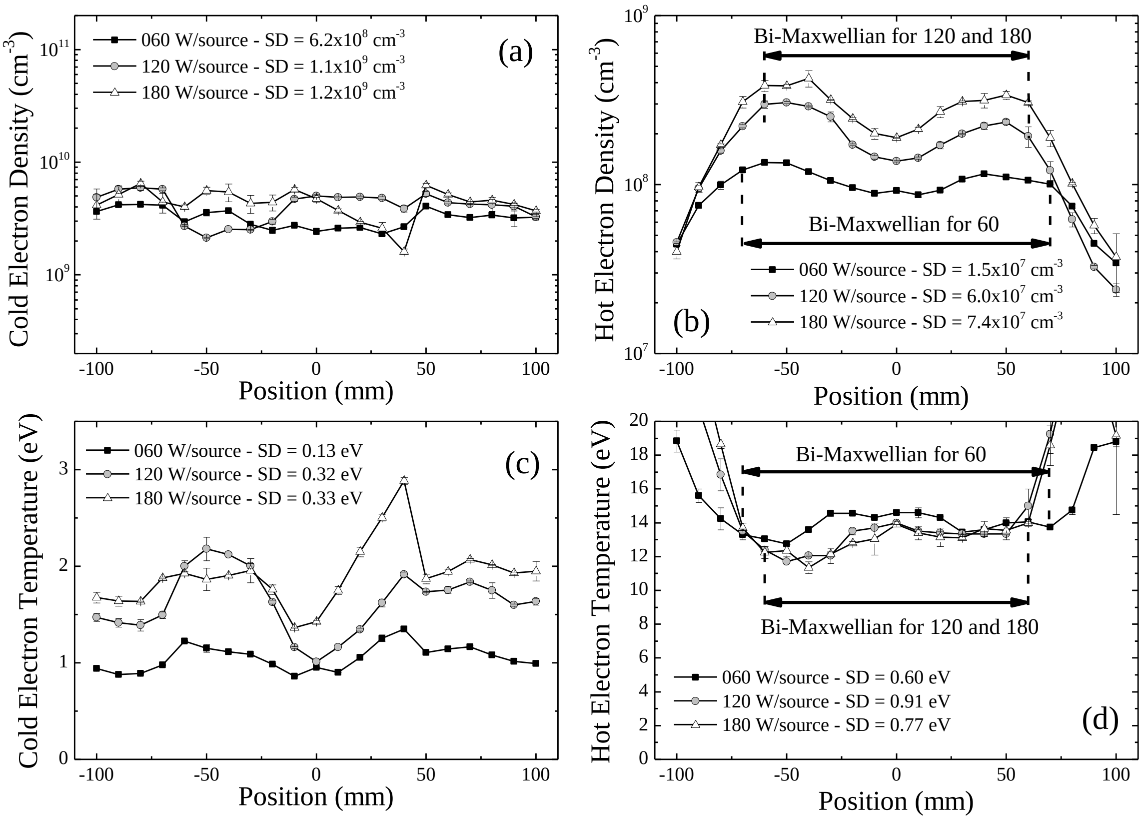

Figure 4.10. Spatial distribution of electron densities and temperatures for a pressure of 4 mTorr. SD refers to the standard deviation of each parameter. For hot electron densities and temperatures, the standard deviations are calculated only for the region where the EEDF is bi-Maxwellian. Error bars are calculated from two series of measurements.

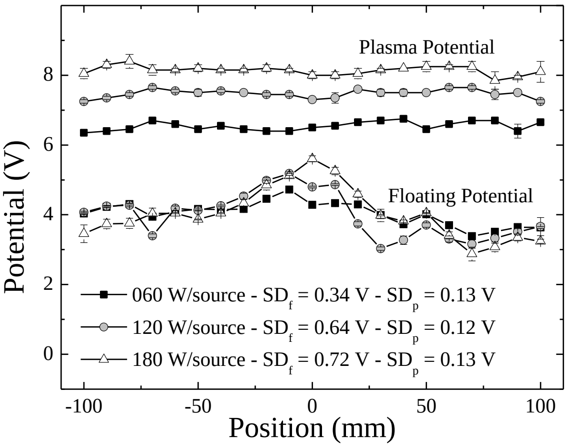

Figure 4.11. Spatial distribution of plasma and floating potential for a power of 8 mTorr. SD$_f$ and SD$_p$ refer to the standard deviation of floating and plasma potential respectively. Error bars are calculated from two series of measurements.

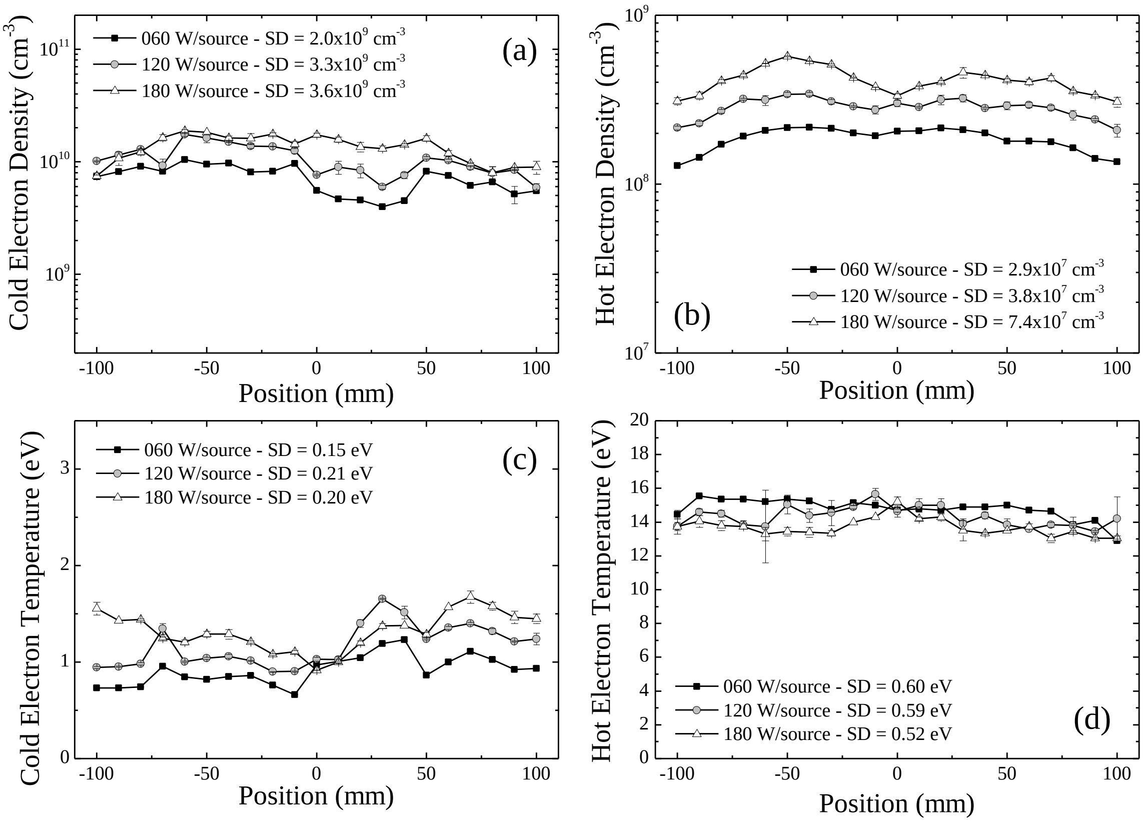

Figure 4.12. Spatial distribution of electron densities and temperatures for a pressure of 8 mTorr. SD refers to the standard deviation of each parameter. Error bars are calculated from two series of measurements.

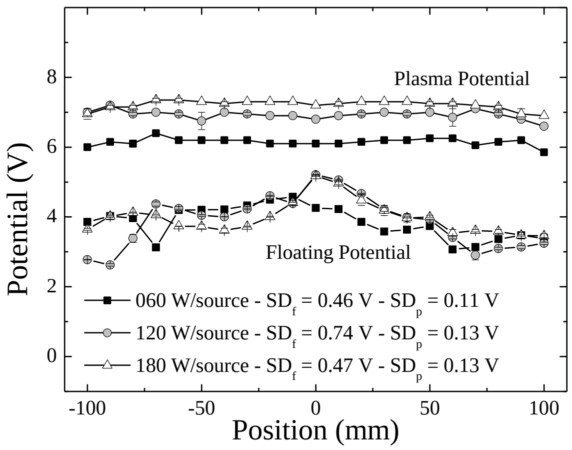

Figure 4.13. Spatial distribution of plasma and floating potential for a power of 12 mTorr. SD_f and SD_p refer to the standard deviation of floating and plasma potential respectively. Error bars are calculated from two series of measurements.

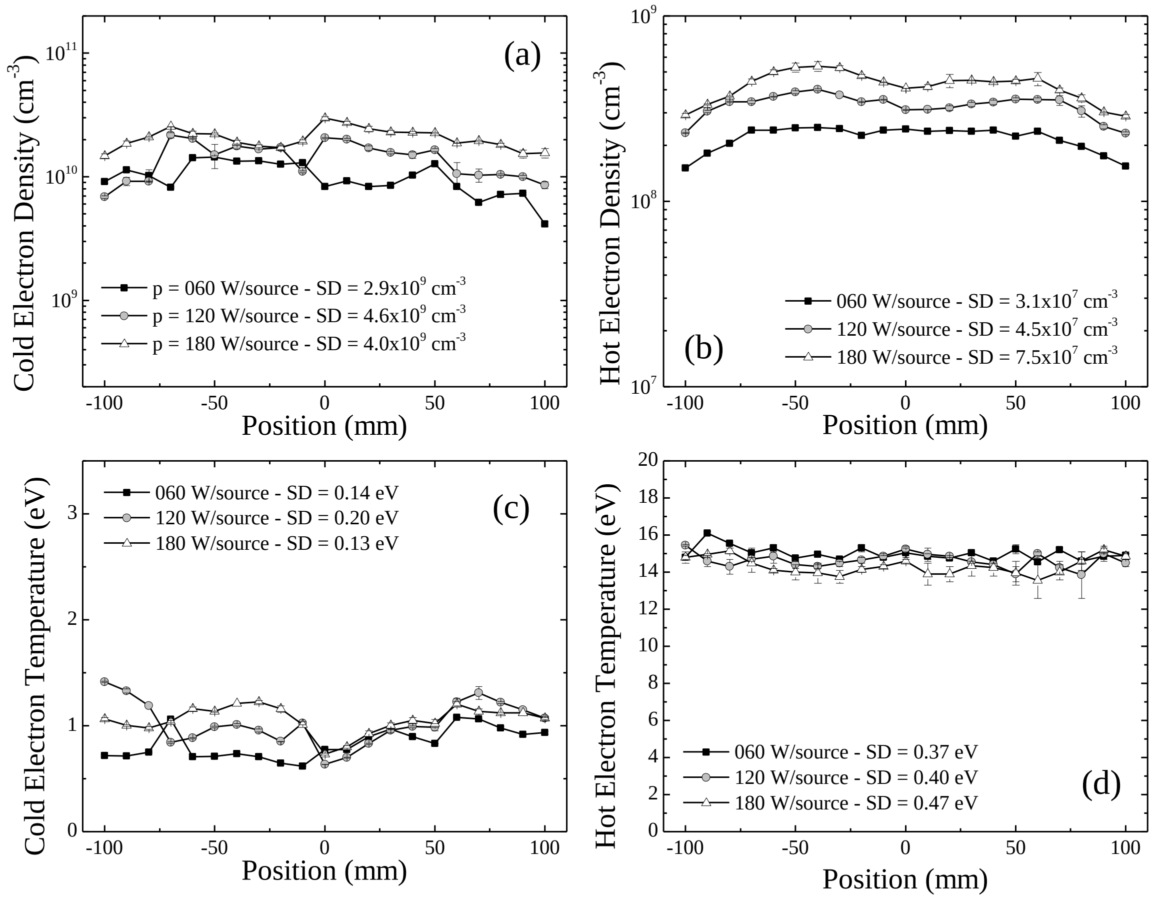

Figure 4.14. Spatial distribution of electron densities and temperatures for a pressure of 12 mTorr. SD refers to the standard deviation of each parameter. Error bars are calculated from two series of measurements.

The average values and the relative standard deviations of the plasma parameters are summarized in the tables below. For the two higher pressures, the plasma seems to be more homogeneous in terms of temperature.

Table 4-2. Average values and relative standard deviations of cold electron density ($n_{e,cold}$) spatial measurements.

Pressure (mTorr)	4 mTorr			8 mTorr			12 mTorr		
Power (W/source)	60	120	180	60	120	180	60	120	180
Average ($x10^{10}$ cm^{-3})	0.32	0.42	0.45	0.75	1.1	1.4	1	1.4	2.1
Standard Deviation (%)	19.2	27.1	26.3	27.6	30.6	26.2	28.6	32.1	19.1

Table 4-3. Average values and relative standard deviations of hot electron density ($n_{e,hot}$) spatial measurements. Only the region where the EEDF is bi-Maxwellian is considered.

Pressure (mTorr)	4 mTorr			8 mTorr			12 mTorr		
Power (W/source)	60	120	180	60	120	180	60	120	180
Average ($x10^{8}$ cm^{-3})	1.1	2.1	3	1.9	2.9	4.1	2.2	3.3	4.2
Standard Deviation (%)	14.3	28.1	24.7	15.4	13.2	18.0	14.1	13.7	17.8

Table 4-4. Average values and relative standard deviations of cold electron temperature ($T_{e,cold}$) spatial measurements.

Pressure (mTorr)	4 mTorr			8 mTorr			12 mTorr		
Power (W/source)	60	120	180	60	120	180	60	120	180
Average (eV)	1.05	1.63	1.90	0.91	1.16	1.32	0.83	1.02	1.05
Standard Deviation (%)	12.6	19.6	17.3	16.6	18.7	15.1	17.1	19.9	11.9

Table 4-5. Average values and relative standard deviations of hot electron temperature ($T_{e,hot}$) spatial measurements. Only the region where the EEDF is bi-Maxwellian is considered.

Pressure (mTorr)	4 mTorr			8 mTorr			12 mTorr		
Power (W/source)	60	120	180	60	120	180	60	120	180
Average (eV)	13.8	13.8	12.9	14.7	14.3	13.6	15.0	14.6	14.3
Standard Deviation (%)	4.2	6.9	5.9	4.0	4.1	3.8	2.4	2.74	3.2

4.2.1.2 H^- Production

For the same configuration a parametric study of negative ion production, by means of electrostatic probes and laser photodetachment, is realized. The probe is positioned at the center of the chamber as presented in Figure 4.6A. The EEDF that is obtained for four indicative pressures and an injected power of 180 W is presented in Figure 4.15. A small deviation from bi-Maxwellian, which increases in severity as the pressure is increased, is observed. However, for most of the energy range, EEDF is very well described by a bi-Maxwellian function.

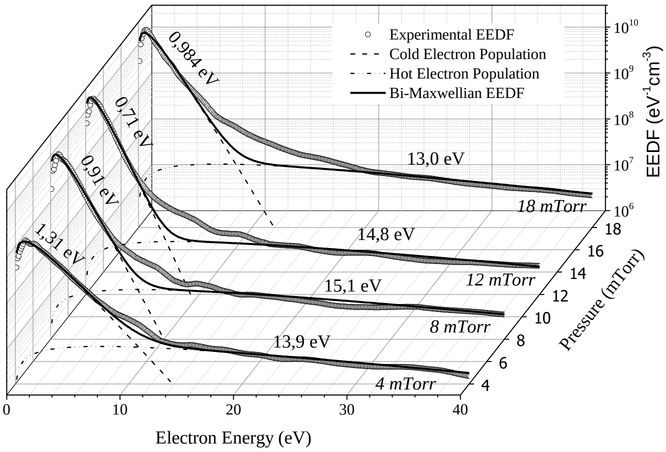

Figure 4.15. Indicative EEDF measurements for nominal power (180 W/source) for the configuration A.

The pressure dependence of cold and hot electron density, cold and hot electron temperature as well as negative ion density and relative negative ion density (n_{H^-}/n_e ratio) is presented in Figure 4.17. Cold electron density is initially increasing with pressure and reaches saturation in the high pressure range. Its maximum value as high as $3x10^{10}$ cm^{-3}. Cold electron temperature on the other hand is reduced as a function of pressure. Both parameters are optimized for negative ion production in the high pressure range. Negative ion density has a similar evolution with the cold electron density and reaches values in the order of $4x10^9$ cm^{-3}. The relative negative ion density ($n_{H^-}/n_{e,cold}$ ratio) is optimized between 5 and 10 mTorr.

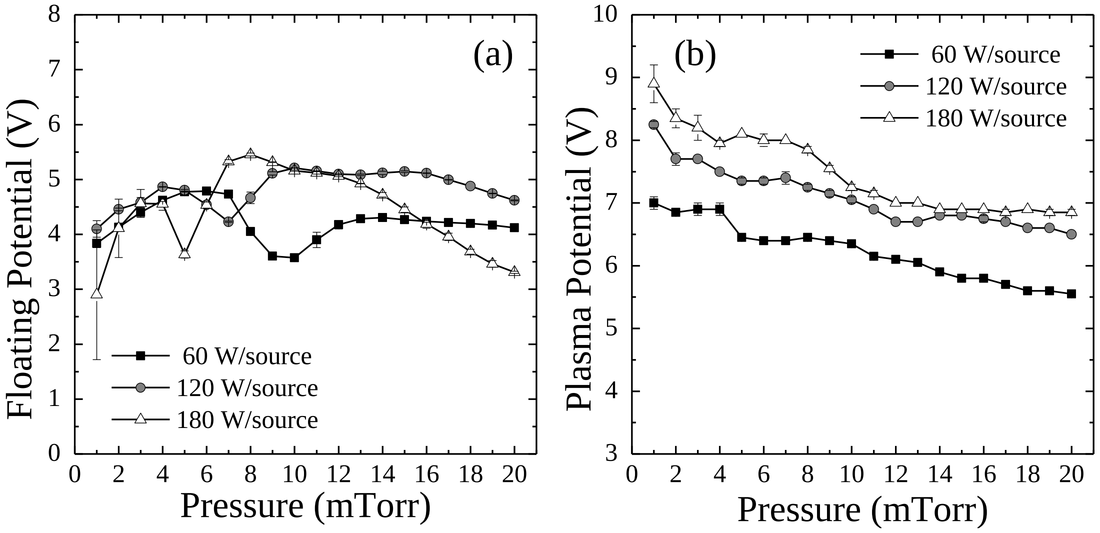

Figure 4.16. Pressure dependence of (a) floating and (b) plasma potential for configuration A. Error bars are calculated from two series of measurements.

For the lowest pressure of 1 mTorr, the signal to noise ratio (SNR) of the probe current and the photodetachment signal were too low for reliable determination of the hot electron temperature and the negative ion density. For this reason this measurements are not included in Figure 4.17d and f. The rest of the parameters can still be determined with a good accuracy.

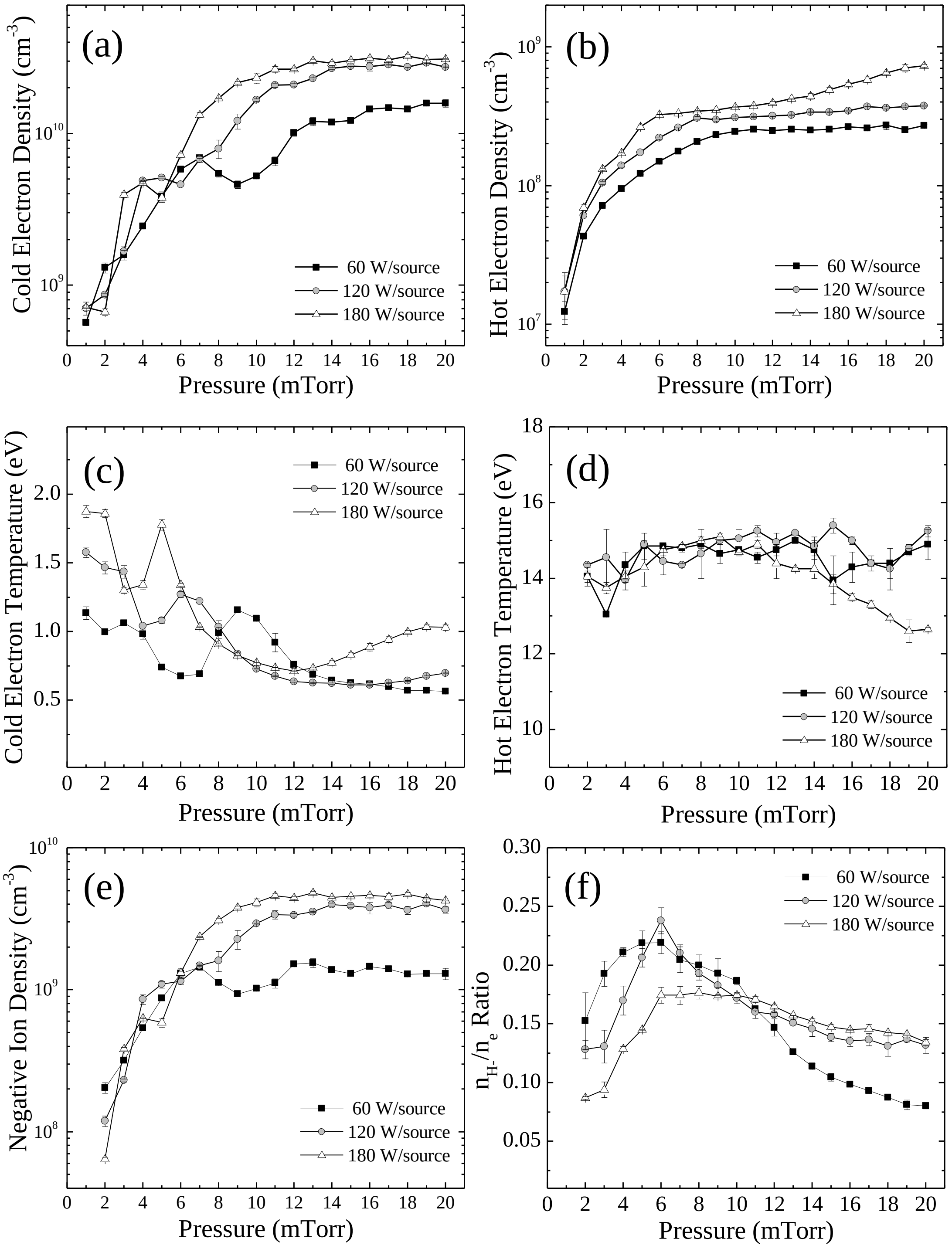

Figure 4.17. Pressure dependence of (a) cold electron density (b) hot electron density, (c) cold electron temperature, (d) hot electron temperature (e) negative ion density and (f) n_{H^-}/n_e ratio. Error bars are calculated from two series of measurements.

4.2.1.3 Optical emission spectroscopy study

The degree of dissociation (D) can be determined by optical emission spectroscopy diagnostics. A detailed presentation of the experimental setup can be found in Section 3.1.3. The method for calculating D on the basis of a collisional-radiative model developed for this purpose [162,163] and the visible emission spectra of Prometheus I, is presented Section 3.1.3.

For the application of the model, the gas temperature is required. This temperature can be derived from the Doppler broadening of spectral lines. The method for the calculation of the atomic translational temperature for the broadening of the Balmer-β is also presented in Section 3.1.3. The atomic translational temperature measured in Prometheus I for nominal power is presented in Figure 4.18. This temperature seems to be between 1400 and 1800 K (or ~0.13-0.15 eV) and to reduce linearly with pressure.

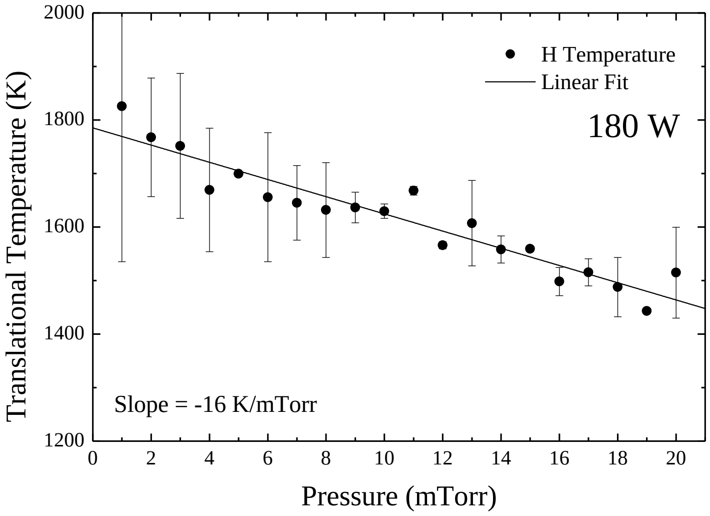

Figure 4.18. Translational temperature of atoms for the nominal power of 180 W/source. Error bars are calculated from two series of measurements.

However, the molecular temperature is not the same as the atomic temperature. Atoms are lighter and gain energy in dissociation processes [157] and thus have a considerably higher translational temperature. The ratio between the two temperatures depends on various parameters including the pressure. For low pressures the H temperature can be about 70% higher than the H_2 temperature ($T_{H2}/T_H = 696$ K/1160 K ≈ 0.6 for 11.2 mTorr [30,36]) while for higher pressures the difference is reduced ($T_{H2}/T_H = 1170$ K/1430 K ≈ 0.8 for 100 mTorr [157]). For the low pressure discharge of Prometheus I, the ratio of $T_{H2}/T_H=0.6$ is adopted and the molecular temperature is assumed to be in the order of 850 - 1100 K (about 0.08 – 0.10 eV).

The power dependence of the translational temperature is not as important as its pressure dependence. For pressures of 4 and 12mTorr this dependence is presented in Figure 4.19. For the entire power range, the temperature appears to change by about 100 K. On the other hand, for the entire pressure range, the temperature presented in Figure 4.18 changes more than 300 K. Since the molecular temperature is already very crudely estimated from the atomic temperature, the gas temperature is assumed to be independent of the injected power.

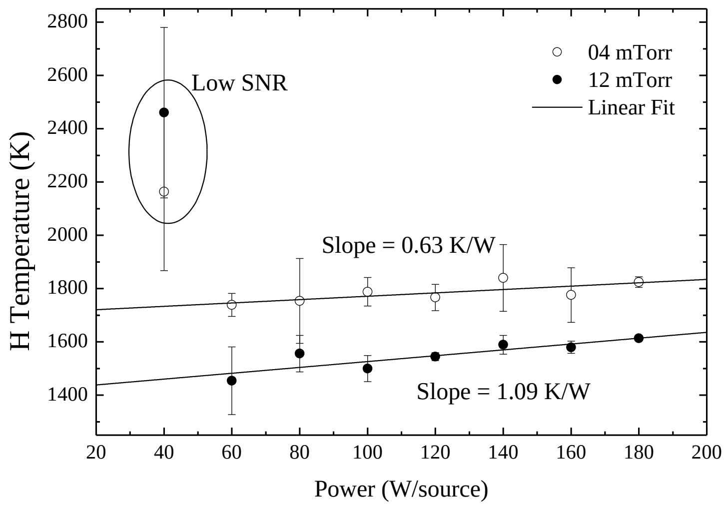

Figure 4.19. Gas temperature dependence on power for pressures of 4 and 12 mTorr. Error bars are calculated from two series of measurements.

By following the procedure in Section 3.1.3 the degree of dissociation as calculated by the ratio of the Balmer-α and Balmer-β atomic lines to the Q1 line of the 2-2 band of the Fulcher-α band system. Some indicative spectra of the used lines are presented in Figure 4.20, while the pressure dependence of the n_H/n_{H2} ratio is presented in Figure 4.21.

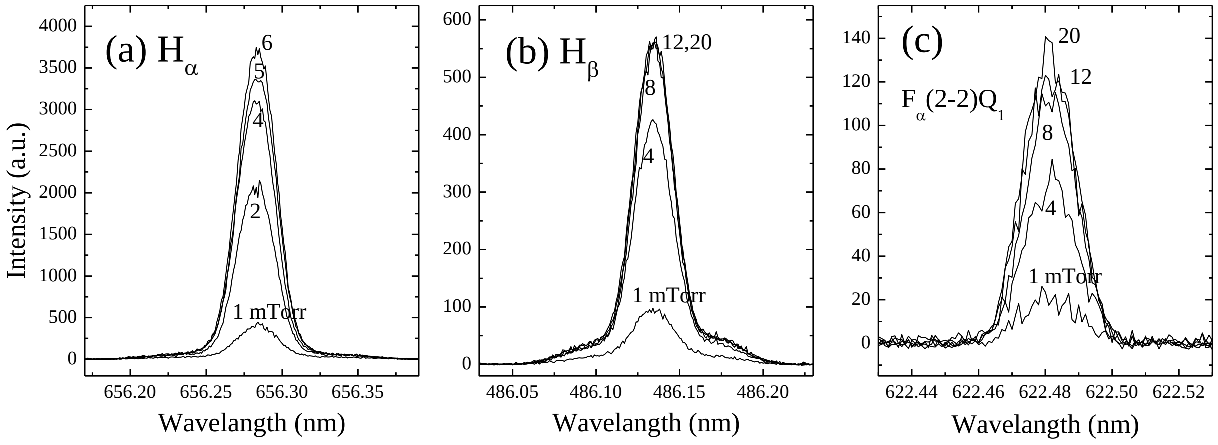

Figure 4.20. Indicative spectral lines used for the determination of the degree of dissociation. Power = 180 W/source.

An important note, concerns the higher degree of dissociation which is observed when calculating the n_H/n_{H2} ratio with the Balmer-α line (Figure 4.20). This spectral line, has an intensity which is proportional to the H(n=3) atomic density, which is also selectively populated by the mutual neutralization reaction (2.4) [171]. The dissociation degree calculated from the Balmer-β line is not affected by this process, making it a much better approximation (Figure 4.21b). The considerably different value for 1 mTorr, might be attributed to the "noisy" Fulcher band spectral line (Figure 4.20c), which does not allow accurate intensity estimation.

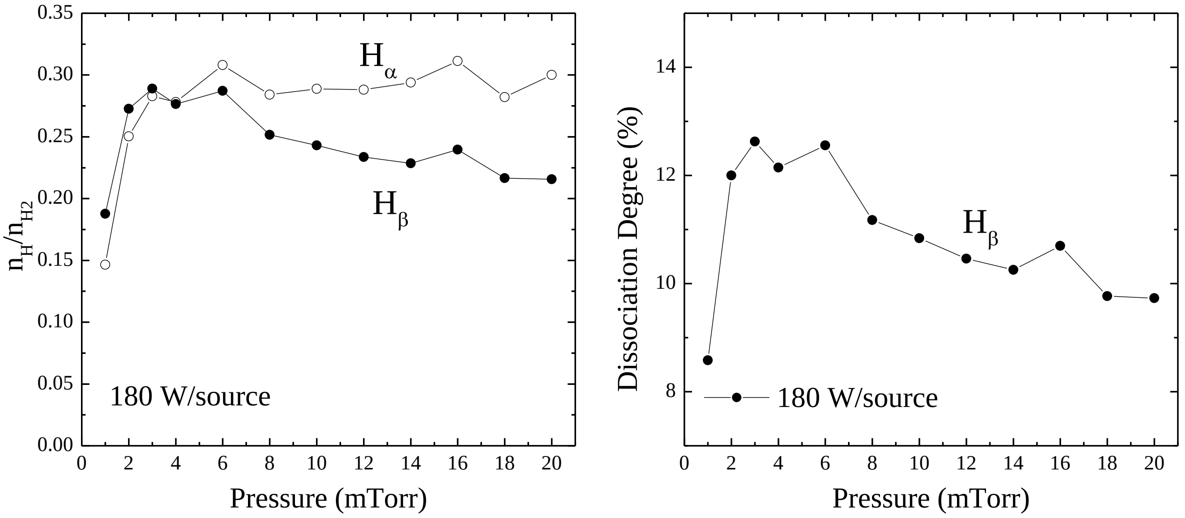

Figure 4.21. (a) Ratio of atomic to molecular density and (b) degree of dissociation. P=180 W.

The power dependence of the n_H/n_{H2} ratio is presented in Figure 4.22. For the three pressures that were studied, the dependence on the discharge power appears to be linear.

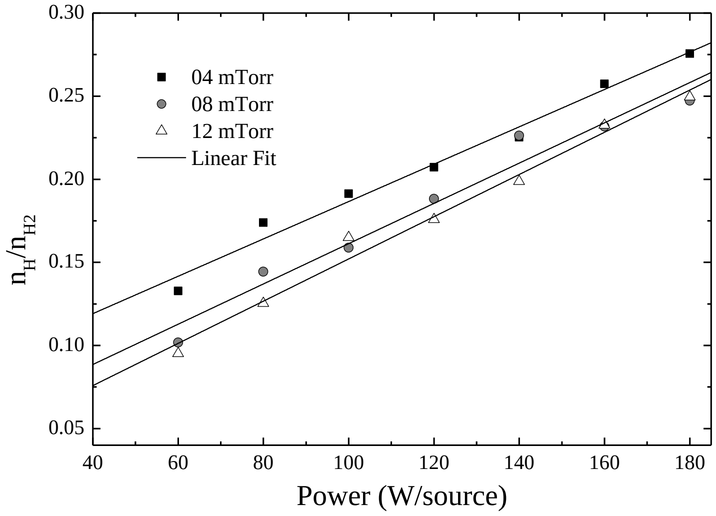

Figure 4.22. Ratio of atomic to molecular density as a function of power.

The n_H/n_{H2} ratio reaches values in the order of 0.25 which is higher than the ratio met in traditional filament sources (~ 0.06) [30,161]. This is a strong indication that in the considered ECR plasmas, the atoms might play an important role that was not observed before for filament H^- ion sources.

4.2.2 Characterization of configuration B

For this configuration the probe is kept at the same height and the ECR zones are moved 30 mm higher. The plasma is studied by means of electrostatic probe and laser photodetachment.

4.2.2.1 Spatial characterization

The same spatial characterization that was realized for configurations A is also performed for configuration B. Spatially resolved measurements of floating and plasma potential, cold and hot electron density as well as cold and hot electron temperature are presented from Figure 4.23 to Figure 4.28.

For this configuration, electron densities and temperatures are in the same order of magnitude with those of configuration A. Cold electrons have densities in the order of 10^{10} cm^{-3} and temperatures in the order of 1 eV. Similarly to configuration A, for the case of 4 mTorr, the plasma becomes less dense (~10^{9} cm^{-3}) and hotter ($T_{e,cold}$ up to 2 eV). These results indicate that in the studied region (65 to 95 mm away from the mid-plane of the ECR zones), the plasma is relatively stable, at least in terms of electron populations.

The main difference with configuration A, is related with the deviation of the EEDF from bi-Maxwellian for the pressure of 4 mTorr. For configuration B this deviation extends well into the plasma. Especially in the case of 180 W/source, the bi-Maxwellian approach is valid only for a region of about 60 mm around the center of the chamber.

Other than that, a general qualitative difference has to do with the floating potential and more specifically with its difference from the nearly stable plasma potential. As mentioned earlier, this difference is an indication of the effective electron temperature [170]. For configuration B, this difference appears to be more homogeneous.

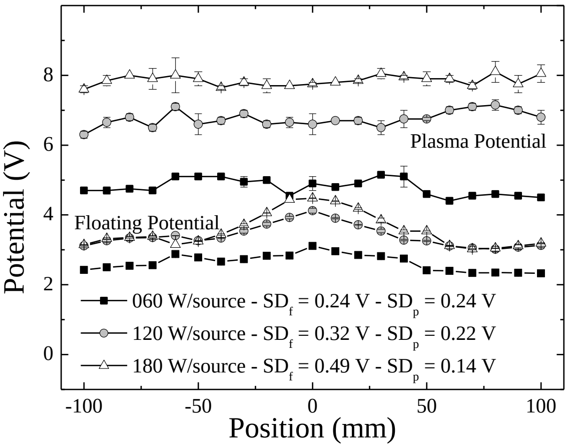

Figure 4.23. Spatial distribution of plasma and floating potential for a power of 4 mTorr. SD$_f$ and SD$_p$ refer to the standard deviation of floating and plasma potential respectively. Error bars are calculated from two series of measurements.

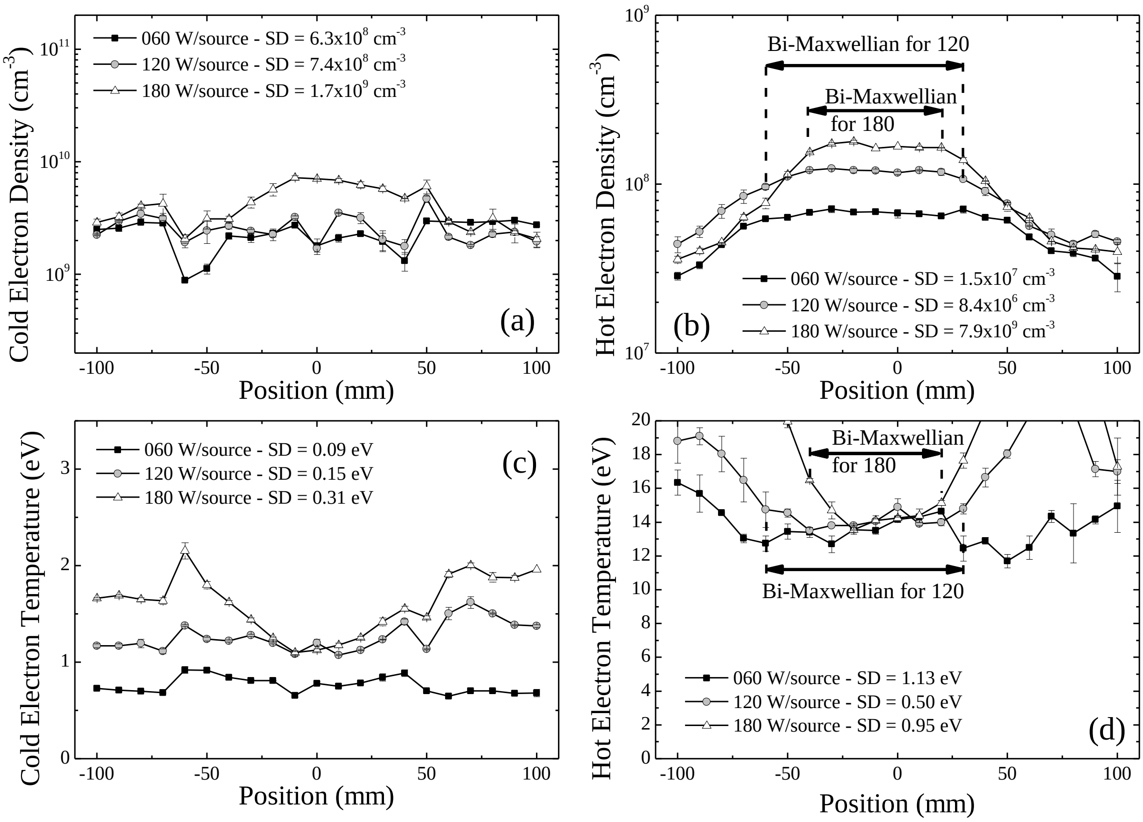

Figure 4.24. Spatial distribution of electron densities and temperatures for a pressure of 4 mTorr. SD refers to the standard deviation of each parameter. For hot electron densities and temperatures, the standard deviations is calculated only for the region where the EEDF remains bi-Maxwellian. Error bars are calculated from two series of measurements.

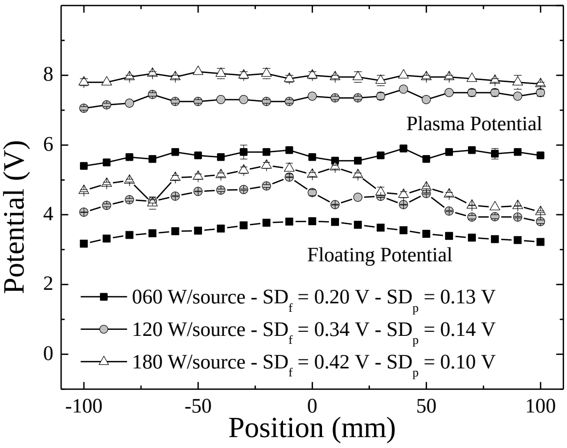

Figure 4.25. Spatial distribution of plasma and floating potential for a power of 8 mTorr. SD$_f$ and SD$_p$ refer to the standard deviation of floating and plasma potential respectively. Error bars are calculated from two series of measurements.

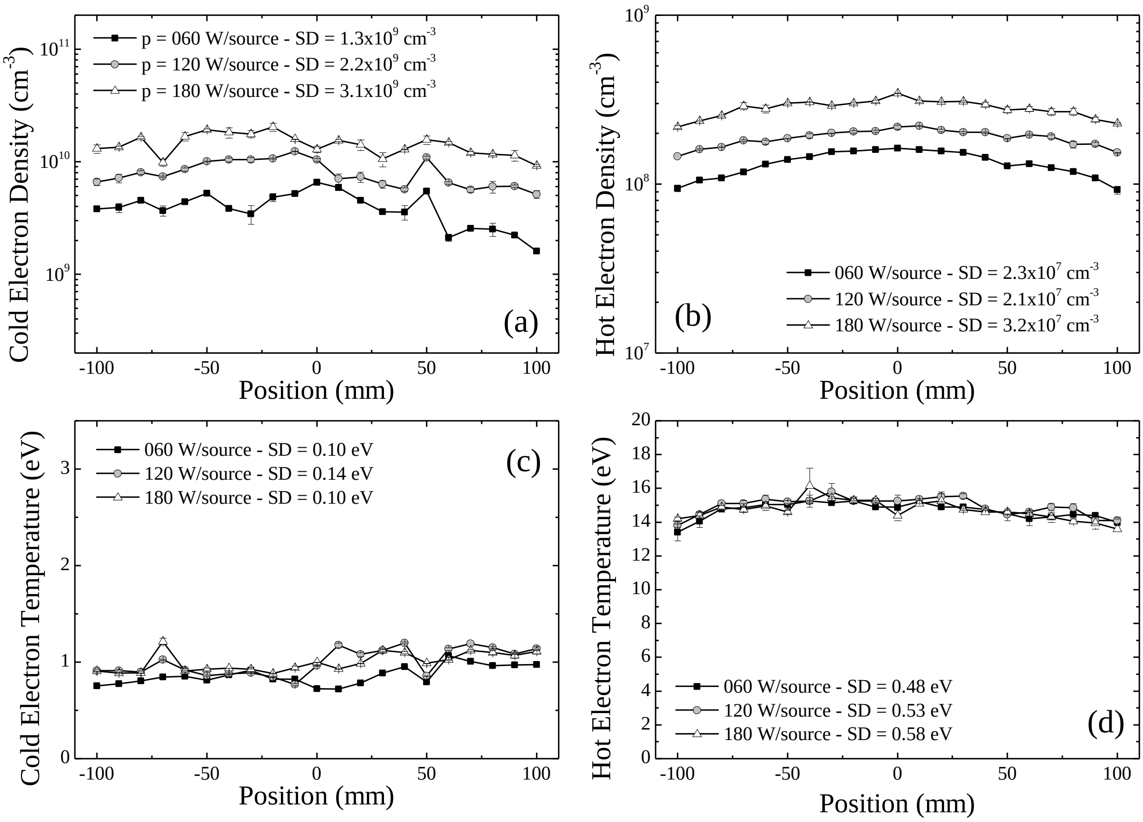

Figure 4.26. Spatial distribution of electron densities and temperatures for a pressure of 8 mTorr. SD refers to the standard deviation of each parameter. Error bars are calculated from two series of measurements.

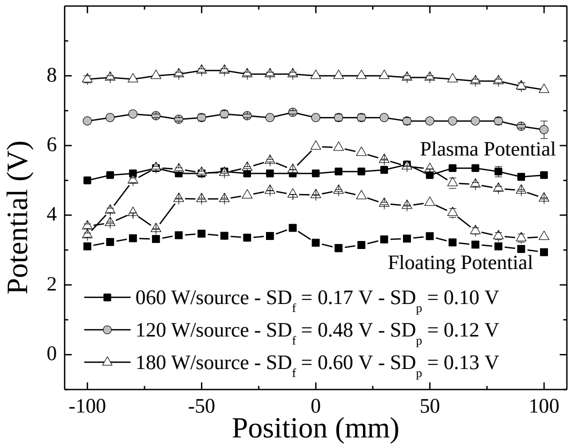

Figure 4.27. Spatial distribution of plasma and floating potential for a power of 12 mTorr. SD$_f$ and SD$_p$ refer to the standard deviation of floating and plasma potential respectively. Error bars are calculated from two series of measurements.

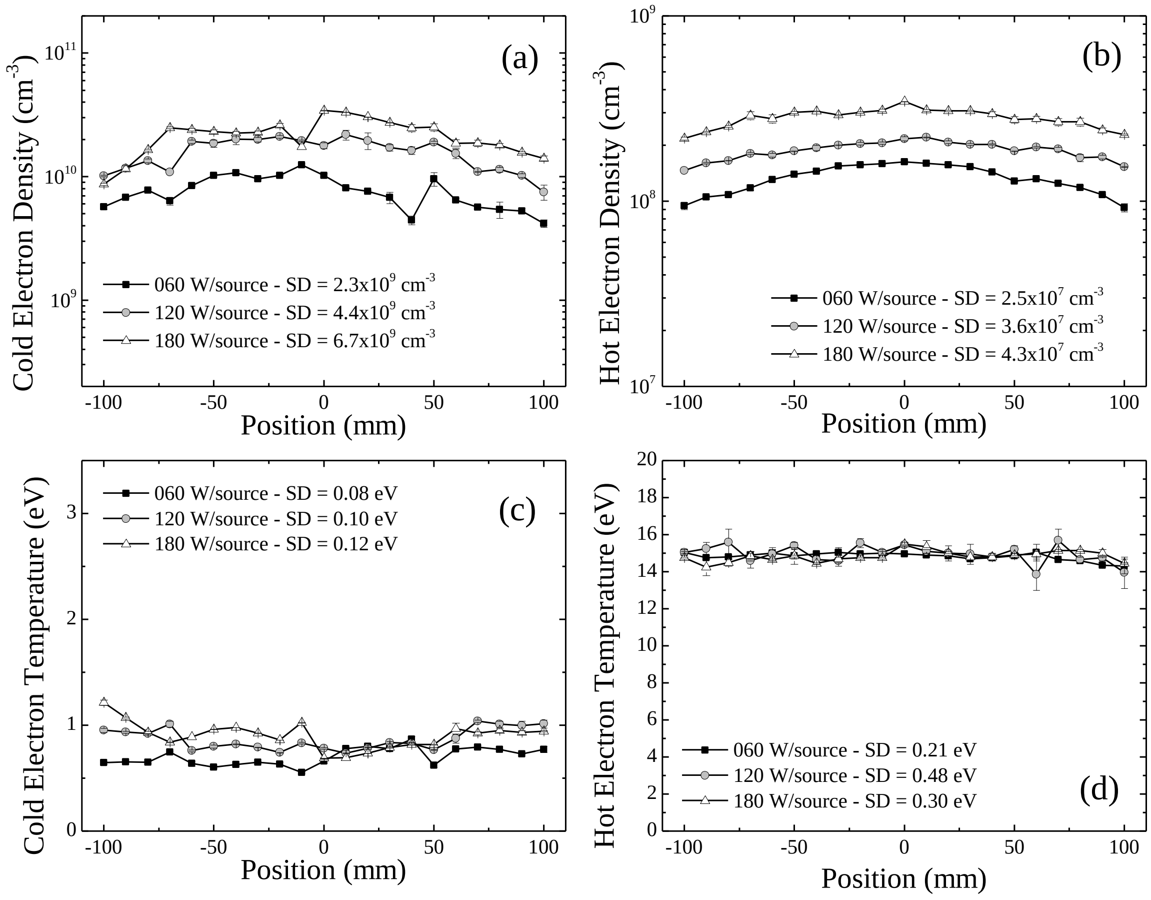

Figure 4.28. Spatial distribution of electron densities and temperatures for a pressure of 12 mTorr. SD refers to the standard deviation of each parameter. Error bars are calculated from two series of measurements.

Average values for electron densities and temperatures as well as the relative standard deviations are summarized in the table below.

Table 4-6. Average values and relative standard deviations of cold electron density ($n_{e,cold}$) spatial measurements.

Pressure (mTorr)	4 mTorr			8 mTorr			12 mTorr		
Power (W/source)	60	120	180	60	120	180	60	120	180
Average ($\times 10^{10}$ cm^{-3})	0.23	0.26	0.43	0.40	0.80	1.40	0.77	1.60	2.20
Standard Deviation (%)	27.1	28.7	40.6	32.9	26.8	21.4	29.9	27.7	30.8

Table 4-7. Average values and relative standard deviations of hot electron density ($n_{e,hot}$) spatial measurements.

Pressure (mTorr)	4 mTorr			8 mTorr			12 mTorr		
Power (W/source)	60	120	180	60	120	180	60	120	180
Average ($\times 10^{8}$ cm^{-3})	0.54	1.15	1.67	1.33	1.88	2.82	1.75	2.80	3.53
Standard Deviation (%)	27.4	7.2	4.7	17.0	10.9	11.3	14.3	12.9	12.1

Table 4-8. Average values and relative standard deviations of cold electron temperature ($T_{e,cold}$) spatial measurements.

Pressure (mTorr)	4 mTorr			8 mTorr			12 mTorr		
Power (W/source)	60	120	180	60	120	180	60	120	180
Average (eV)	0.75	1.26	1.60	0.86	1.00	0.99	0.70	0.86	0.90
Standard Deviation (%)	11.2	12.0	19.1	11.2	13.6	9.8	11.8	11.7	13.8

Table 4-9. Average values and relative standard deviations of hot electron temperature ($T_{e,hot}$) spatial measurements.

Pressure (mTorr)	4 mTorr			8 mTorr			12 mTorr		
Power (W/source)	60	120	180	60	120	180	60	120	180
Average (eV)	13.7	14.2	14.6	14.6	14.9	14.7	14.8	14.9	14.8
Standard Deviation (%)	8.2	3.5	6.4	3.3	3.5	3.9	1.4	3.2	2.0

4.2.2.2 H^- Production

For the same configuration a parametric study of negative ion production, by means of electrostatic probes and laser photodetachment, is realized. The probe is positioned at the center of the chamber as presented in Figure 4.6B. The EEDF that is obtained for four indicative pressures and an injected power of 180 W is presented in Figure 4.29. The same small deviation from bi-Maxwellian (transition region between the two populations) is also observed. However, for this configuration as well, the EEDF is very well described by a bi-Maxwellian function.

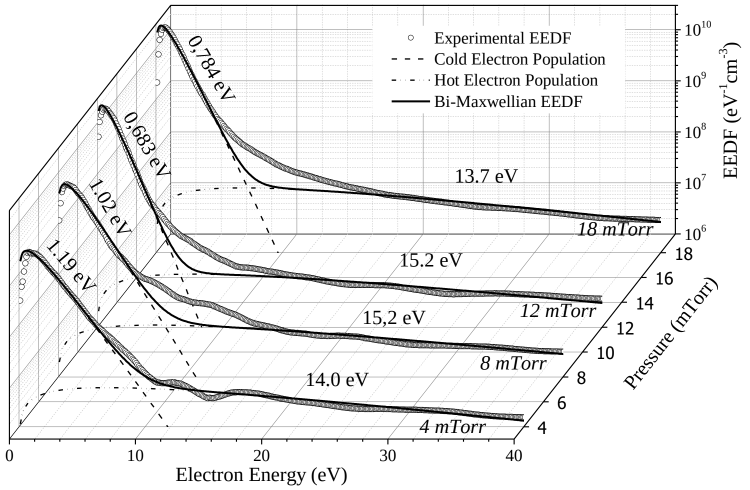

Figure 4.29. Indicative EEDF measurements for nominal power (180 W/source) for the configuration B.

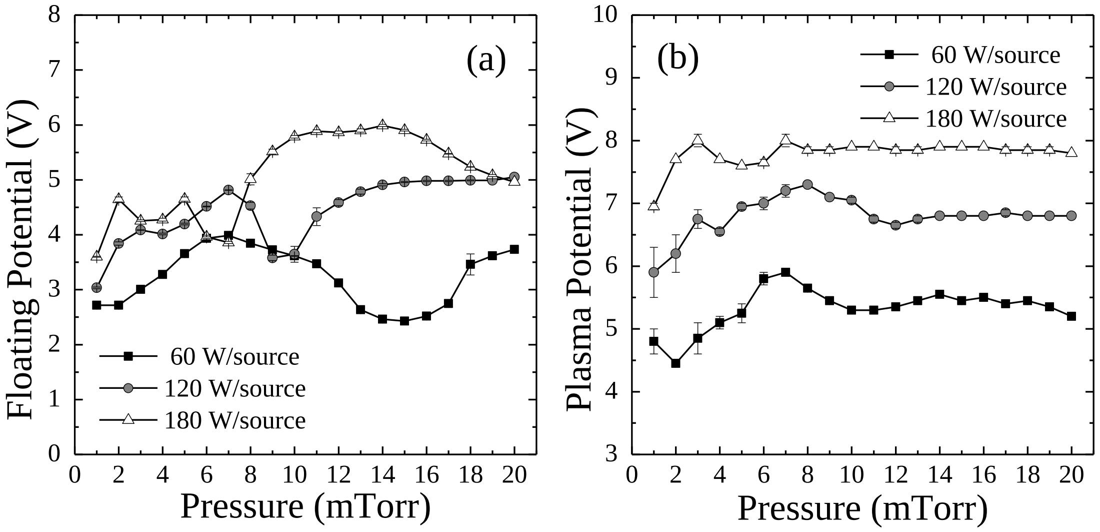

Figure 4.30. Pressure dependence of (a) floating and (b) plasma potential for configuration B. Error bars are calculated from two series of measurements.

The pressure dependence of cold and hot electron density, cold and hot electron temperature as well as negative ion density and relative negative ion density (n_{H^-}/n_e ratio) is presented in Figure 4.31. Cold electron density is initially increasing with pressure and reaches saturation in the high pressure range. Its maximum value is high as $4x10^{10}$ cm^{-3}. Cold electron temperature on the other hand is reduced as a function of pressure. Both parameters are optimized for negative ion production in the high pressure range. Negative ion density has a similar evolution as the cold electron density reaching values of $6x10^9$ cm^{-3}. The $n_{H-}/n_{e,cold}$ ratio is optimized in a region between 4 and 10 mTorr.

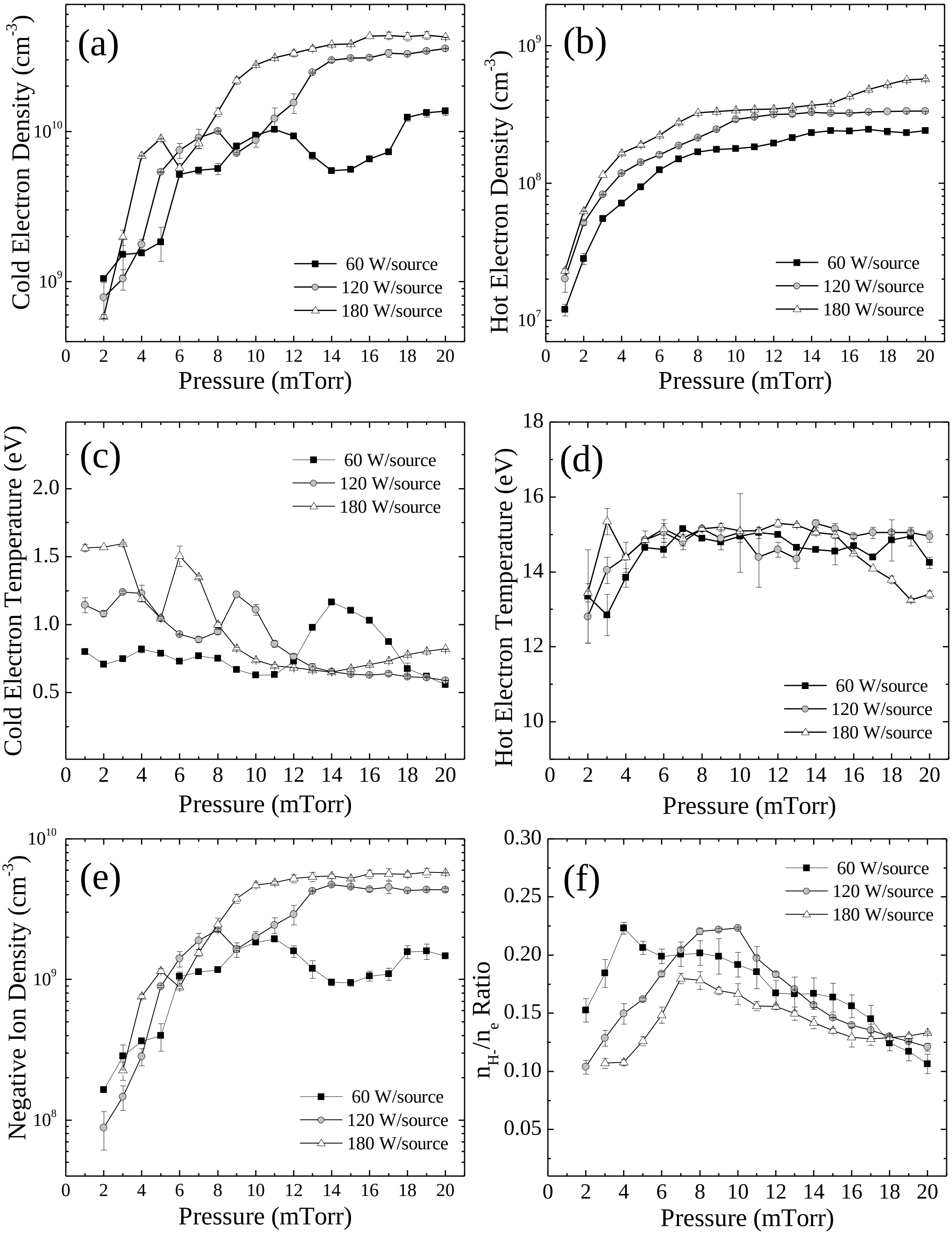

Figure 4.31. Pressure dependence of (a) cold electron density (b) hot electron density, (c) cold electron temperature, (d) hot electron temperature (e) negative ion density and (f) n_{H-}/n_e ratio for the configuration B. Error bars are calculated from two series of measurements.

4.2.3 Characterization of configuration C

With this configuration probe measurements and laser photodetachment are realized in the positions that correspond to the three viewports of the lower part of the chamber (see Figure 4.6C).

4.2.3.1 H^- Production for C (Center)

The EEDF for some indicative pressures and for nominal power (180 W/source) is presented in Figure 4.32.The EEDF remains bi-Maxwellian for all the parameters of this configuration.

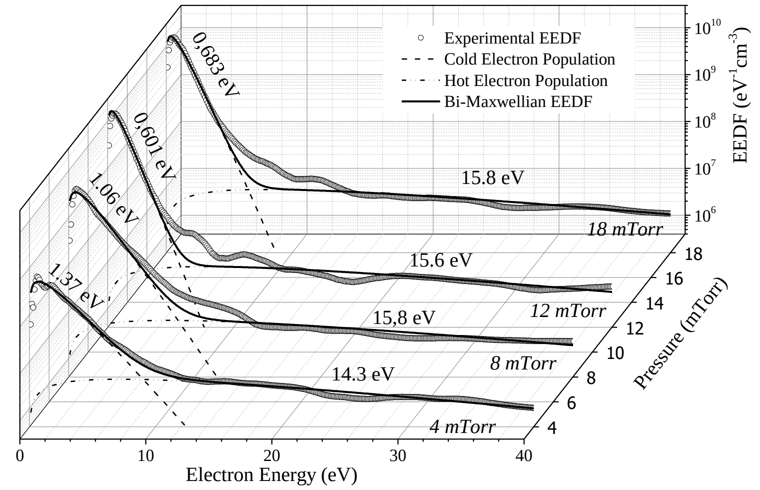

Figure 4.32. Indicative EEDF measurements for nominal power (180 W/source) for the configuration C (Center).

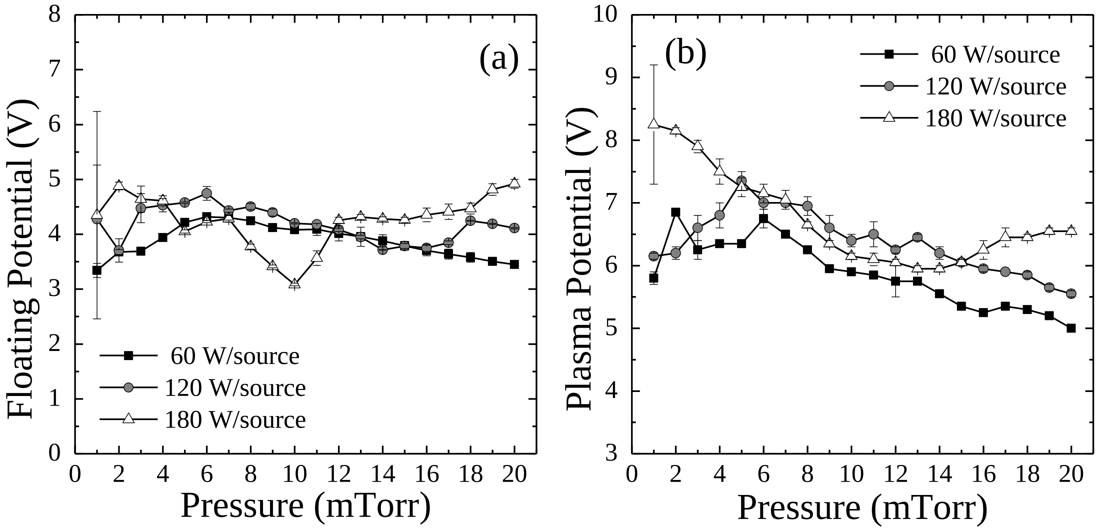

Figure 4.33. Pressure dependence of (a) floating and (b) plasma potential for configuration C (Center). Error bars are calculated from two series of measurements.

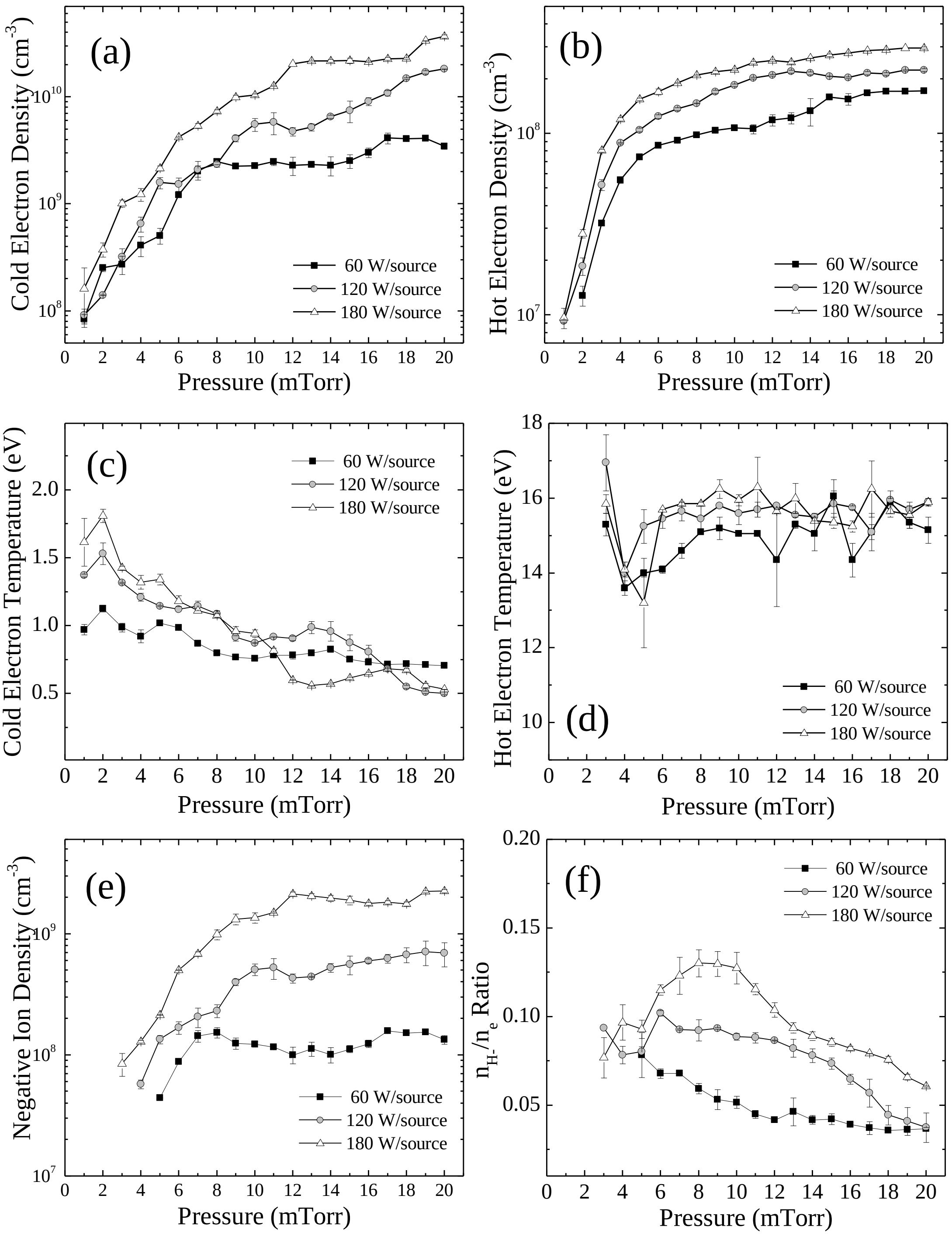

Figure 4.34. Pressure dependence of (a) cold electron density (b) hot electron density, (c) cold electron temperature, (d) hot electron temperature (e) negative ion density and (f) n_{H^-}/n_e ratio for the configuration C(Center). Error bars are calculated from two series of measurements.

4.2.3.2 H^- Production for C (Right)

The EEDF for some indicative pressures and for nominal power are presented in Figure 4.35. Electrostatic probe and laser photodetachment results are presented in Figure 4.36 and Figure 4.37. The sharp decrease of the EEDF for the pressure of 4 mTorr is related with the aforementioned deviation from bi-Maxwellian (see Figure 4.8). For this pressure, the invalid temperature that is measured by the usual fitting procedure, described in Section 3.1.1, is quite high.

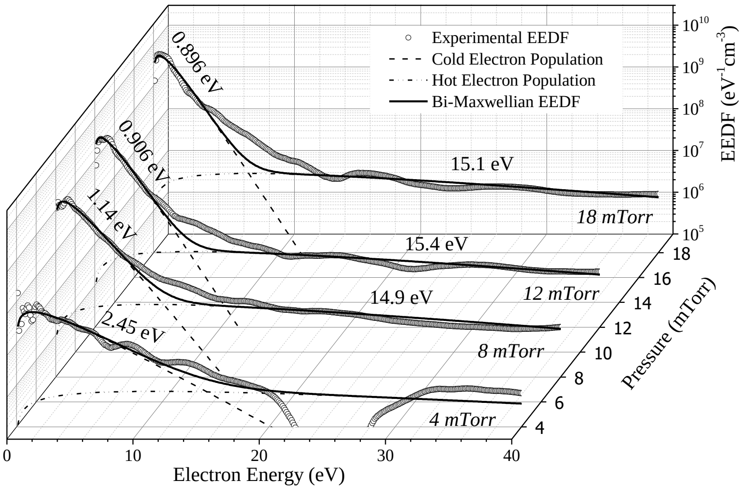

Figure 4.35. Indicative EEDF measurements for nominal power (180 W/source) for the configuration C(Right).

Despite being at the same distance from the ECR zones with Configuration C(Center), the plasma at this position has a slightly lower electron density and a considerably lower negative ion density (one order of magnitude lower). The difference between the two configurations is the presence of the lower chamber wall, which for this cases is located only 18 mm away from the probe position. On the other hand, for configuration C(Center), the probe is located above the opening for the pumping system and has a greater distance from the nearest wall. The n_{H^-}/n_e ratio is even more dramatically decreased, and has values in the order of 0.05 (contrary to ~0.10 for the previous configuration and ~0.20 for configurations A and B).

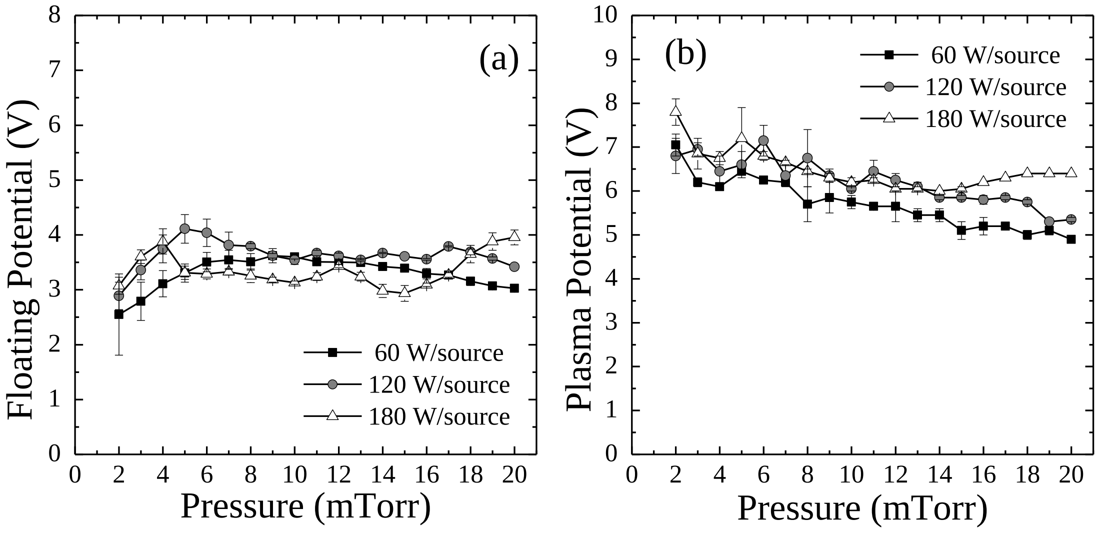

Figure 4.36. Pressure dependence of (a) floating and (b) plasma potential for configuration C (Right). Error bars are calculated from two series of measurements.

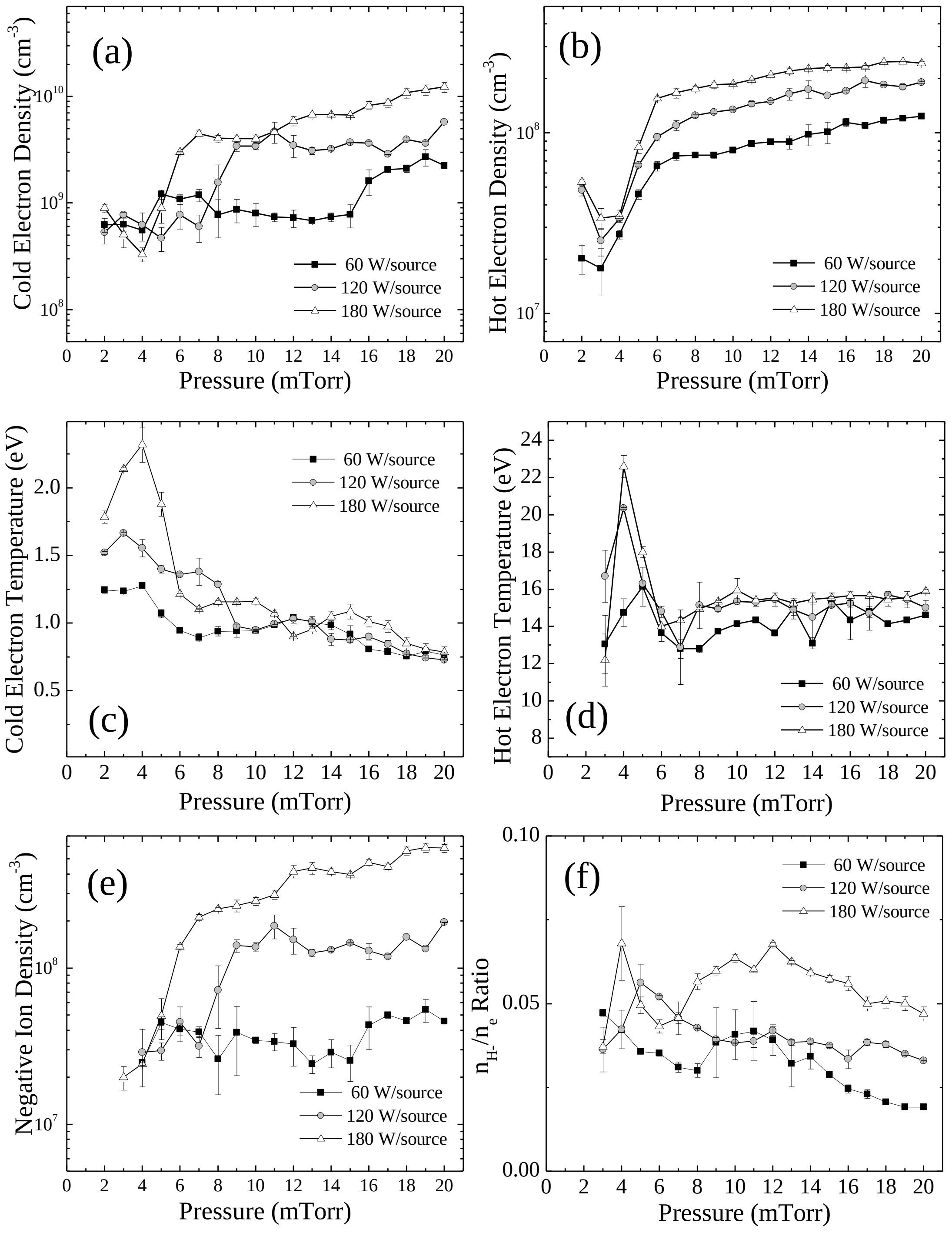

Figure 4.37. Pressure dependence of (a) cold electron density (b) hot electron density, (c) cold electron temperature, (d) hot electron temperature (e) negative ion density and (f) n_{H-}/n_e ratio for the configuration C(Right). Error bars are calculated from two series of measurements.

4.2.3.3 H^- Production for C (Left)

In this last position of the C configuration, electrostatic probe and laser photodetachment measurements are realized form the left lower viewport of the chamber. Like in the symmetrical case (C(Right)), the EEDF that is presented in Figure 4.38 reveals a deviation from bi-Maxwellian for the pressure of 4 mTorr.

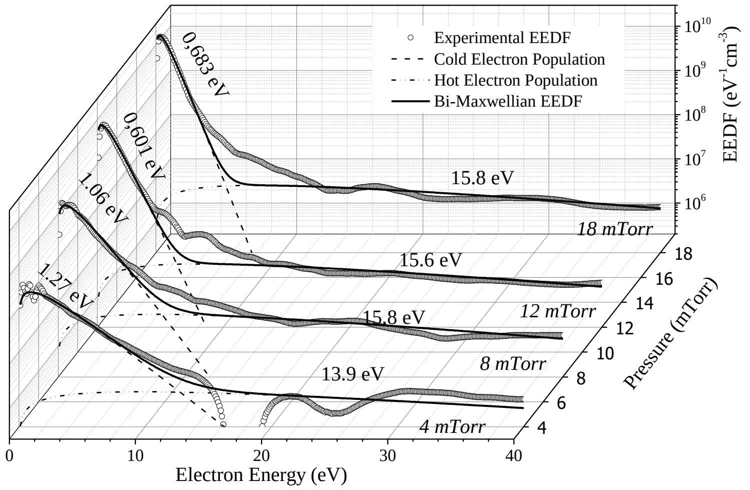

Figure 4.38. Indicative EEDF measurements for nominal power (180 W/source) for the configuration C (Left).

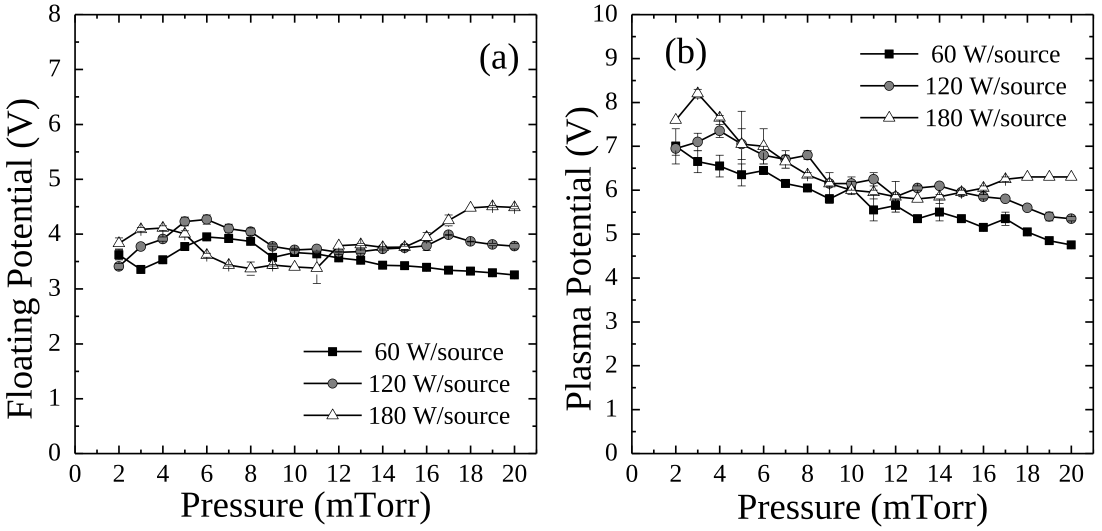

Figure 4.39. Pressure dependence of (a) floating and (b) plasma potential for configuration C (Left). Error bars are calculated from two series of measurements.

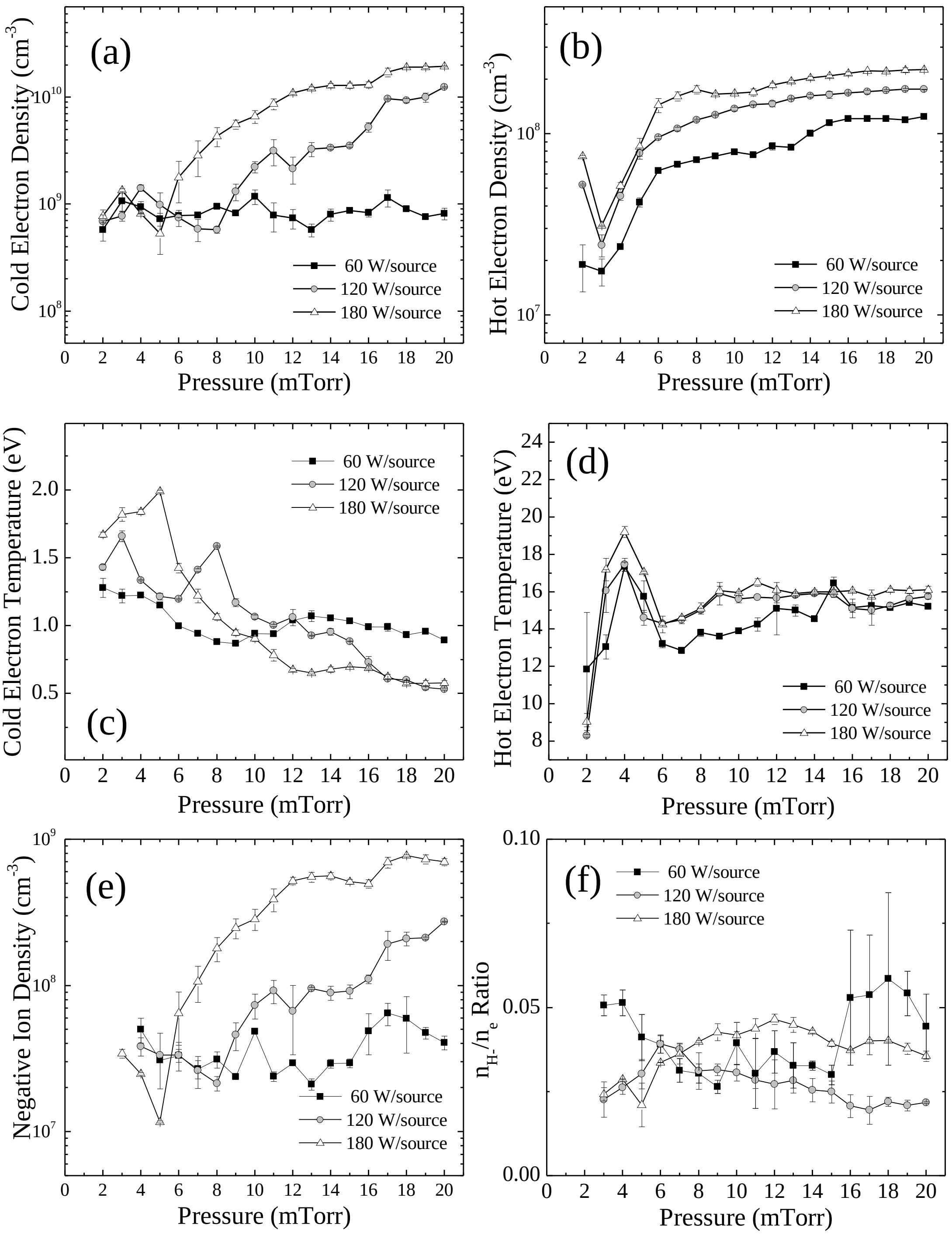

Figure 4.40. Figure 4.32. Pressure dependence of (a) cold electron density (b) hot electron density, (c) cold electron temperature, (d) hot electron temperature (e) negative ion density and (f) $n_{H\text{-}}/n_e$ ratio for the configuration C(Left). Error bars are calculated from two series of measurements.

4.2.4 Summary of characterization

This preliminary study has shown that the source Prometheus I operates more efficiently for higher pressures. On the other hand, the n_{H^-}/n_e ratio is optimized in an intermediate pressure range that depends on the configuration of the source and the injected power. The first two configurations (A and B) have similar negative ion density and n_{H^-}/n_e ratios, while for the configuration C both densities and the ratios are considerably reduced.

While being in the same height, the two outer positions of configuration C, have considerably different negative ion densities and n_{H^-}/n_e ratios than the central one. Their main difference is that the central position being directly over the opening of the turbo pump, has a bigger distance from the chamber walls. When the deviation from bi-Maxwellian was observed in the spatial measurements was also near the chamber walls (see for example Figure 4.10). This indicates that the observed deviation can be caused from the presence of the walls. The exact mechanism, requires further study.

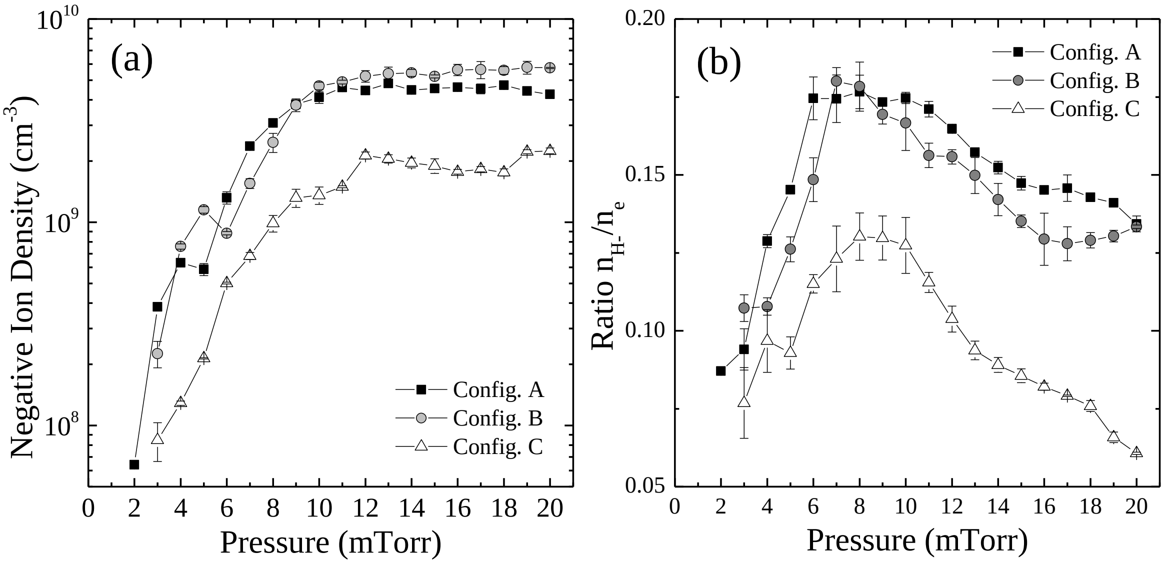

Figure 4.41. Pressure dependence of (a) the negative ion density and (b) its ratio to cold electron density, for the three different positions of the sources. Power = 180 W/source.

The negative ion density for nominal power (180 W/source) is in the order of 5-6x10^9 cm^{-3}. The relative negative ion density (n_{H^-}/n_e) has a maximum in the order of 0.25 but for a lower power (see Sections 4.2.1 and 4.2.2). For nominal power the relative negative ion density (Figure 4.41) can be as high as 0.18. The maximum electron density of the source is about 4x10^{10} cm^{-3}. Plasma densities and the negative ion densities are quite similar for the first two configurations. For the rest of the chapter, the source mainly operates with Configuration A.

4.3 Formation of negative ions

4.3.1 Neutral resonant ionization

Despite the fact that dissociative attachment is considered to be the main production channel for negative ions, there are additional mechanisms that require investigation. A recently proposed mechanism (neutral resonant ionization) involves collisions between H(n=2) excited atoms [68] (also see Section 2.1.1). If this mechanism is indeed important, the source optimization would be on a completely different basis. In order to increase negative ion density, the dissociation degree should be increased. The opposite is required for dissociative attachment based production, which relies on vibrationally excited molecules.

The dominance of DA has been proven for other volume sources [30]. In that case the degree of dissociation was in the order of 3% with a molecular density about $1x10^{14}$ cm^{-3} and an atomic density about $6x10^{12}$ cm^{-3}. However, microwave discharges have in general a greater degree of dissociation [172]. If that is the case for the ECR discharge of Prometheus I, the contribution of this new mechanism has to be evaluated. The dissociation degree has been calculated in Section 4.2.1.3 to be higher than 10%. Since the atomic fraction of the source is relatively higher there is the possibility that the atomic hydrogen might play a more significant role.

Having an important hydrogen density is not the only requirement for neutral resonant ionization to be important. This process concerns collisions between atoms in their first excited state H(n=2) and not in their ground state [87]. A parameter that correlates well with the H(n=2) density is the Lyman-α emission. Despite the intense Lyman-α radiation emitted by hydrogen plasmas, the relation between negative ion output and Lyman-α intensity had never been measured. A recent paper [52] contributed to this topic by including measurements on extracted negative ions and Lyman-α intensity. By combining these data, with the elimination of the power variable, a quadratic relation between negative ions current and Lyman-α intensity was observed [68]. This relation was interpreted as an indication that negative ion formation in this source is attributed to H(n=2) collisions.

Indeed, the presently accepted mechanism for collisional destruction of the H(2s) metastable hydrogen atoms is the Stark effect mixing of the metastable $2s_{1/2}$ with the neighboring $2p_{1/2}$ and $2p_{3/2}$ states of atomic hydrogen, resulting in emission of Lyman-α radiation [173]. However, collisional quenching is not the only source of Lyman-α emission. An additional source is the emission that follows the electron impact excitation of ground state atomic hydrogen. An attribution of the Lyman-α emission to the first process would imply the 2s state of the H(n=2) atoms is dominantly populated. In that case, a quadratic relation between Lyman-α intensity and negative ion production could be interpreted as a quadratic relation between negative ion density and H(n=2) density, which is exactly what should be expected from this newly proposed mechanism.

The data that were borrowed as an indication of this mechanism had two experimental limitations. The first one is related to the radiation measurements that were realized looking axially in the source LISA [52].

With this configuration the radiation from both the driver region and the bulk of the plasma were integrated. The second limitation is related to the use of extracted negative ion currents instead of negative ion densities. While the extracted current is related to the density near the extractor [59], the relation is not necessarily linear and depends on the many parameters of the extraction system.

In order to offer some experimental correlation between Lyman-α emission and negative ion density, and determine if the proposed quadratic relation is confirmed for Prometheus I, both quantities were measured with the experimental setup presented in Section 3.1.

Photodetachment measurements were realized in the bulk plasma of the source Prometheus I. The Lyman-α radiation was measured with filter centered on 122 nm. Details about both techniques can be found in Chapter 3. The results of this experiment are presented in Figure 4.42

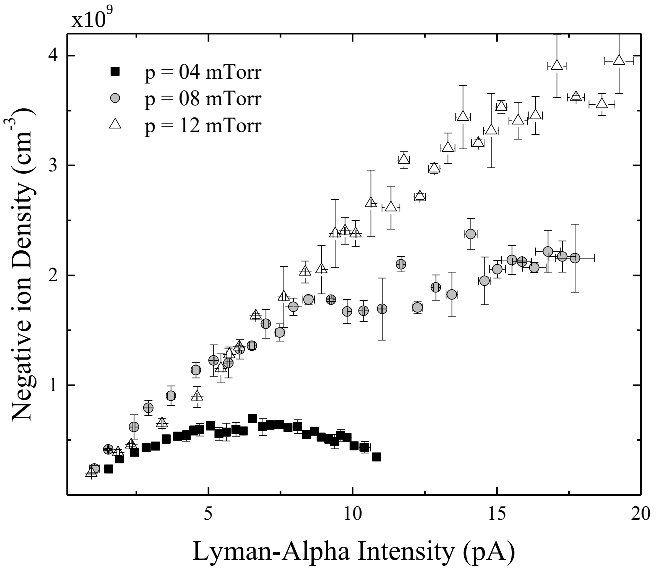

Figure 4.42. Experimentally determined relation between negative ion density and Lyman-α emission.

Evidently a quadratic behavior is not observed. However, it has to be made clear that the distinction between H^- fractions produced through different mechanisms is not feasible based on these experimental data. A better approach would be to combine them with a self-consistent rate equations analysis. However, this analysis would require addition experimental data and cross sections that are not available.

4.3.2 Confirmation of the dominance of dissociative attachment

In order to confirm that dissociative attachment (DA) is the dominant negative ion production channel, a simplified kinetic model is considered. This model includes: a) the DA as the only process that leads to the formation of negative ions and b) the main loss processes which are mutual neutralization, associative detachment, and electron detachment (see Section 2.1.2). This simplified model is described by the rate equation for the negative ion density:

$$\frac{dn_{H^-}}{dt} = \sum_{v=0}^{14} n_{H_2(v)} n_e \left\langle \sigma_{DA}(v), u \right\rangle - k_{MN} n_+ n_{H^-} - k_{AD} n_H n_{H^-} - n_{H^-} n_e \left\langle \sigma_{ED}, u \right\rangle \qquad (4.1)$$

where $n_{H2}(v)$ stands for the vibrationally resolved density of the ground state molecular hydrogen, n_e for the electron density, $\sigma_{DA}(v)$ for the vibrationally resolved cross section of DA presented in Figure 4.43, k_{MN} for the rate coefficient of mutual neutralization, n_+ for the density of positive ions (this loss term includes three components due to H^+, H_2^+ and H_3^+), k_{DA} for the rate coefficient of associative detachment, n_H for the atomic hydrogen density and finally σ_{ED} for the electron detachment cross section.

In principle there should also be a loss term corresponding to the flux of negative ions from the plasma to the chamber walls. However, due to the positive plasma potential (typically +7 V), H^- ions, which have a temperature similar to that of the temperature of the gas (0.1-0.2 eV) are very well confined and this loss term can be ignored. The equilibrium density of negative ions calculated from Equation (4.1) is:

$$n_{H^-} = \frac{\sum_{v=0}^{14} n_{H_2(v)} n_e \left\langle \sigma_{DA}(v), u \right\rangle}{k_{MN} n_+ + k_{AD} n_H + n_e \left\langle \sigma_{ED}, u \right\rangle} \tag{4.2}$$

The nominator of Equation (4.2) represents the formation rate of H^- and is very sensitive to the distribution of vibrational states (VDF). However, this distribution is not available and its measurements is quite complicated. On the other hand, for a realistic calculation, it would be far from accurate to consider equilibrium vibrational kinetics. The vibrational distribution of low-temperature plasma is definitely non-Maxwellian [39,110]. A better approach would be to borrow a vibrational distribution from literature. For this purpose, the VFD provided by Mosbach [30,36] is adopted, due to the similarities of experimental conditions (pressure and power).

The most similar discharge conditions between the two sources, for which the vibrational distribution was accurately given, refer to Prometheus I working with 900 W in 11 mTorr of H_2 and the source of Mosbach [30] working with 1000 W in 11.2 mTorr. The EEDF for these conditions has been measured for Prometheus I with electrostatic probes and can be used for the calculation of the formation rate with the cross section presented in Figure 4.43.

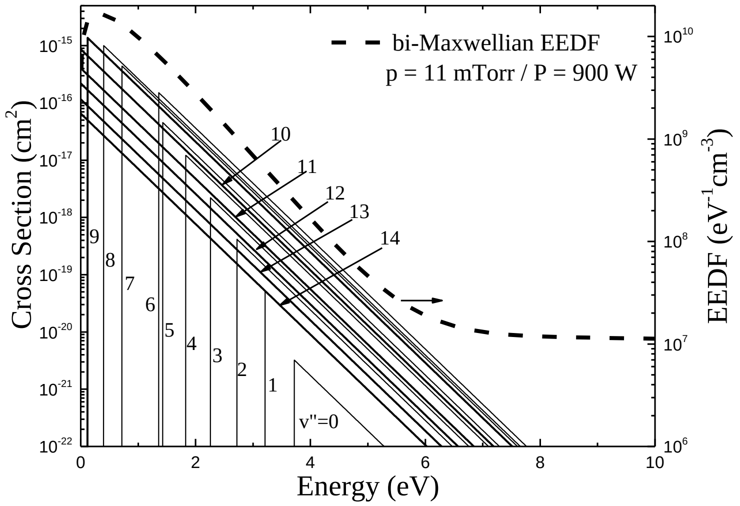

Figure 4.43. Cross sections and EEDF used for the calculation of negative ion formation rate in Prometheus I.

What is essentially adopted, is the shape of the VDF. It would be a huge overestimation to adopt the actual values as well. For a more accurate estimation some correction between the two sources is required.

For this correction, the main production mechanism of high lying vibrational states, which is EV excitation (see Figure 2.9 of Chapter 2), is considered. The excitation rate from the ground state molecule (v=0) to the first two singlet states is calculated for the two sources. The cross sections for electron impact excitations through these states is presented in Figure 4.44. The EEDFs for the two sources are presented in the same figure, as reconstructed from the measured electron densities and temperatures.

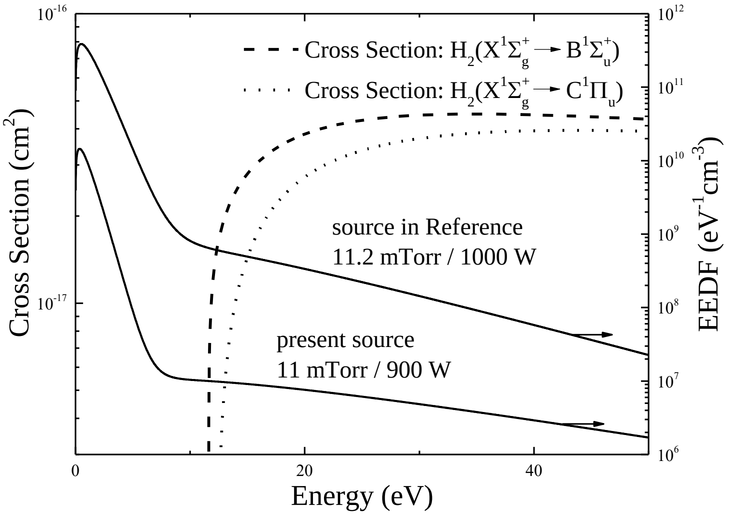

Figure 4.44. Comparison of the EV vibrational excitation for the source Prometheus I and the source in Ref. [30]

This excitation rate for the source of Mosbach [30] is 1.37x10^{16} cm^{-3}s^{-1} while that of Prometheus I is 6.06x10^{14} cm^{-3}s^{-1}. These values account for the different electron densities and temperatures as well as for the difference in the dissociation degree (see section 4.2.1.3). The ratio between them is 22.1, which can be taken as a correction factor to account for the different excitation rates in the two sources. This calculation actually underestimates the density of vibrational states in the source Prometheus I. The reason for this is that in the source of Mosbach [30] the considerably denser electronic population deactivates high vibrational states through the eV process [36] (Reaction (2.2)). The rest of the important vibrational deactivations processes (see Section 2.2.1) should have similar values for two sources of similar volume, working in similar pressures.

The vibrational distributions of the two sources are presented in Figure 4.45. To account for the total molecular gas density, the unexcited molecules were added to the vibrationally unexcited state density (v=0). With this vibrational distribution and the EEDF that is measured by electrostatic probes, the formation rate of negative ions (nominator of Equation (4.2)) is calculated to be 5.2x10^{12} cm^{-3}s^{-1}.

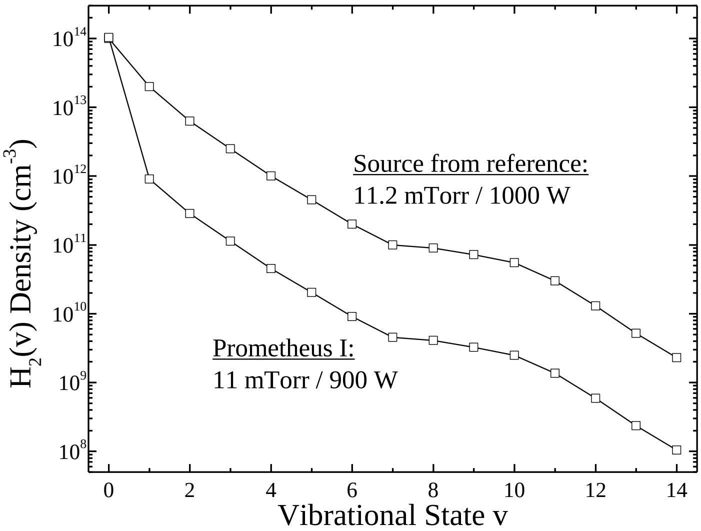

Figure 4.45. Vibrational distribution for the source in Ref. [30] and for Prometheus I.

The denominator of Equation (4.2) represents the loss frequency of negative ions and is dominated by mutual neutralization from H^+ and H_3^+ [30]. The total loss frequency in Ref. [30] has been calculated to be $5x10^4$ s^{-1}. However, in the source Prometheus I the positive ions density is almost 25 times lower ($3.75x10^{10}$ cm^{-3} compared to $9.3x10^{11}$ cm^{-3}). By correcting accordingly, the loss frequency becomes $2x10^3$ s^{-1}.

Another parameter that influences loss frequency is the gas temperature. The dependence follows the $T^{-1/2}$ rule of Reactions (2.3), (2.6) and (2.10). As proposed in [36], the temperature of molecular ions can be considered to be the same with the neutral molecules and the temperature of atomic ions the same with the neutral atoms. As mentioned earlier, the translational temperature of Prometheus I is about 1750 K (0.15 eV) for the atoms and about 1050 K (0.09 eV) for the molecules. The translational temperature for the source of Ref [30] has been mentioned in [36] and is 1160 K (0.1 eV) for the atoms and 696 K (0.06 eV) for the molecules. By correcting accordingly, the total loss frequency becomes $1.63x10^3$ s^{-1}.

By introducing the calculated formation rate and the loss frequency in Equation (4.2) the negative ion density is calculated to be $3.2x10^9$ cm^{-3}. The negative ion density of Prometheus I, measured by photodetachment is $5.3x10^9$ cm^{-3}. Therefore, the value from the crude calculation of H^- density, based solely on formation through the DA process is within the same order of magnitude with the measured density. It appears that the DA process can account for the measured density of negative ions. A more precise calculation of negative ion density would require direct measurement of the vibrational distribution function or its calculation on the basis of a self-consistent model which would be much more complicated.

Since DA is confirmed to be the main source of negative ions, any potential enhancement of negative ions production must rely on enhancing the densities of the DA reactants, i.e. cold electrons and vibrationally excited molecules. The next part of this work relates to the formation of vibrational states.

4.4 Formation of vibrationally excited molecules

4.4.1 Surface atomic recombination

As presented in Figure 4.21 the degree of dissociation of ECR plasmas is considerably higher than that of traditional filament sources. The possibility of the formation of vibrational states from the recombinative desorption of hydrogen atoms has been well established [39] (also see Section 2.2.2). Through this mechanism, the material of the ion source chamber wall may have an important impact on the production of negative ions. In order to assess this impact, a dedicated experiment was realized. The detailed description of the setup and the explanation of the concept on which it was build are presented in Section 3.2.

For the realized studies, five materials were chosen: Pyrex, stainless steel, Highly Oriented Pyrolytic Graphite (HOPG), tantalum and finally Yttrium. Pyrex is used as a reference since its surface recombination factor can be controlled by temperature [165] and be kept in very low levels. Stainless Steel (SS) is very interesting as it is the most common chamber material. Tantalum has been known, as a material that can enhance negative ion production [174]. Finally, yttrium is a material with considerably lower work function (3.1 eV) which might affect the production in different ways (e.g. direct surface ionization).

The source ROSAE III is operated in 5 mTorr of pure hydrogen and is supplied with 1 kW of microwave power, divided into four sources. The measured EEDF is presented in Figure 4.46. While cold electron densities depend on the material that is used, the hot electron temperature which is important for spectroscopy diagnostics is effectively the same for all the used materials (9.51, 9.57, 9.28, and 9.45 for HOPG, SS, tantalum and yttrium respectively).

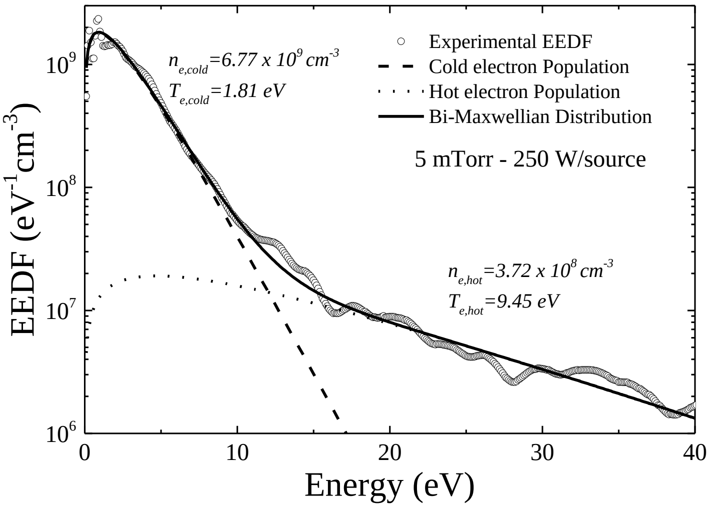

Figure 4.46. EEDF in the source ROSAE III when the chamber is completely covered with Pyrex. Power is 250 W/source and pressure is 5 mTorr.

In order to promote recombinative desorption on the studied material, the surface recombination is suppressed for the rest of the chamber wall, by covering it with Pyrex. This should create an important population of atoms. To confirm this, the method described in Section 3.1.3 is applied for the determination of the degree of dissociation with the hot electron temperature that is measured (Figure 4.47). The temperature of the gas, which was not measured for this study, is assumed to be about 1000 K. In this case the degree of dissociation that is calculated from the ratio of the Balmer-α line to the Fulcher band line is 67.64 while the one calculated by the ratio of the Balmer-β line to the molecular line is 72.57. These dissociation degrees correspond to n_H/n_{H2} ratios of 4.18 and 5.29 respectively. The important difference between the two values, is attributed to the increased sensitivity of the spectral line ratio to the n_H/n_{H2} ratio, when the latter one reaches so high values. Based on this result, the first requirement of this study, which is the presence of an important atomic density that can recombine on the surface, is achieved.

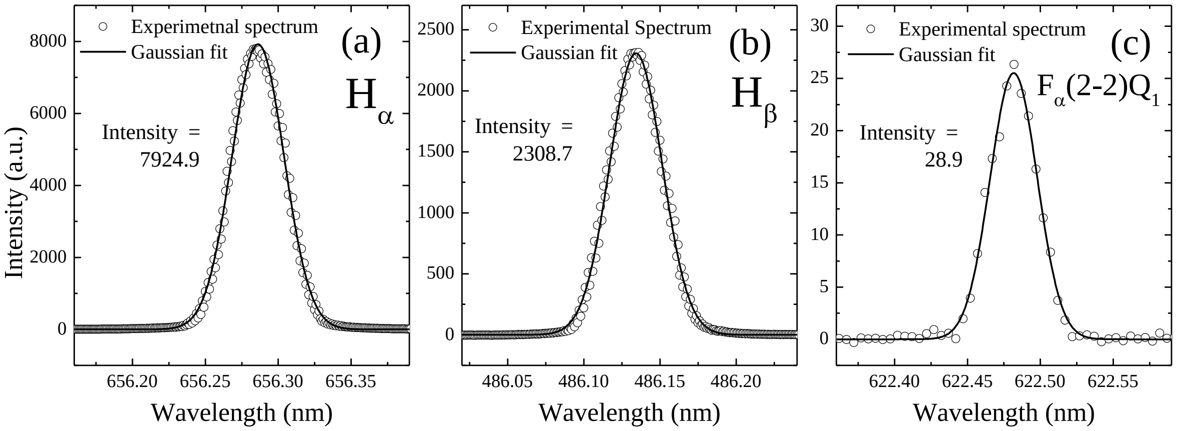

Figure 4.47. Spectral lines used for the determination of the degree of dissociation in ROSAE III.

The measured electron densities and temperatures for different materials are presented in Figure 4.48. The electron temperature seems to be quite stable for all the materials. Electron densities for Pyrex, SS, HOPG and tantalum also have similar values in the range 6-7x10^9 cm^{-3}. On the other hand, the electron density for yttrium is increased above 9x10^9 cm^{-3} which corresponds to an increase of about 2.5x10^9 cm^{-3} or 38% relative to the average of all the other densities. The work function of yttrium (3.1 eV), which is considerably lower than that of common metals like steel (~4.5 eV) allows the attribution of this increase to secondary electron emission (e.g. photoelectric effect from the intense VUV emission [175]).

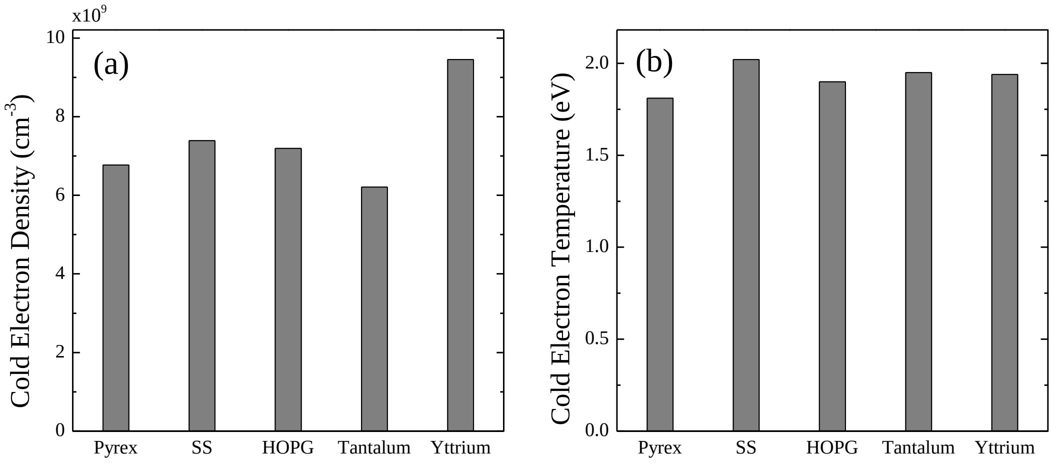

Figure 4.48. Cold (bulk) electron densities (a) and temperatures (b) for the different materials that were used

The negative ion densities and the n_{H-}/n_e ratio are presented in Figure 4.49. The negative ion density does not differentiate appreciably for the first four materials. On the other hand, the yttrium sample leads to a negative ions density which is $1.2\text{x}10^8$ cm^{-3} or 68% higher than the other materials. However, the n_{H-}/n_e ratio is not similarly increased. The extra negative ions can be attributed to the electrons that are emitted from the material (Figure 4.48).

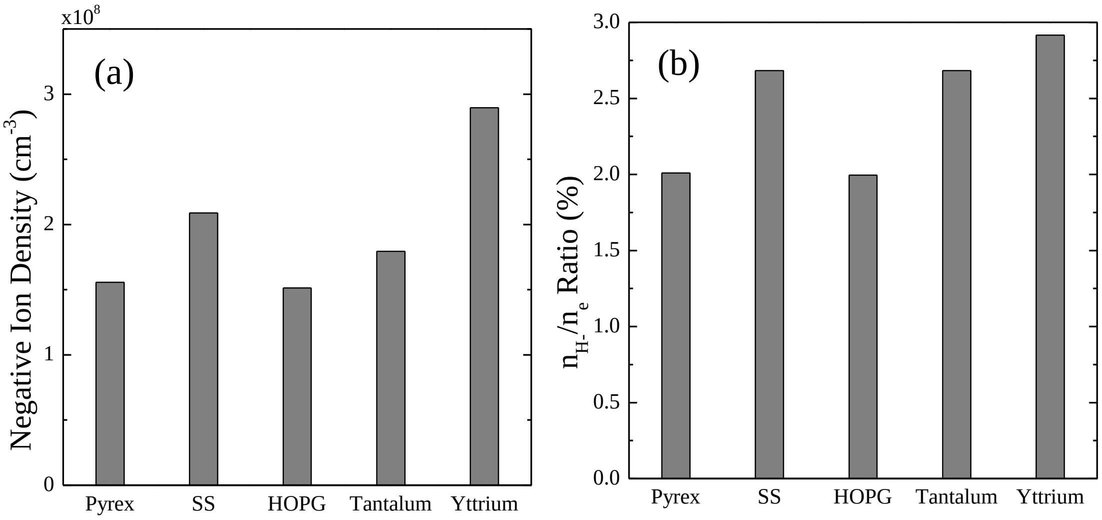

Figure 4.49. (a) Negative ion density and (b) n_{H-}/n_e ratio for the various materials that are used.

The similarity of negative ion measurements, is an indication that recombinative desorption, is not the dominant vibrational excitation process in the plasma under study. Either its contribution is intrinsically small for these experimental conditions, or there is another mechanism that is still dominating vibrational excitation (most likely EV excitation). A second important note is related with the increase which is observed in the negative ions density when the electron density is increased from secondary electrons from the yttrium sample. It appears that secondary electrons may play an important role in the production of negative ions. A more consistent approach, studying the impact of secondary electrons, and more specifically photoelectrons is presented in the Annex.

To determine whether recombinative desorption is masked by another vibrational state formation mechanism or is simply not important, its study has to be separated from the ECR discharges. A convenient way to achieve this, is to study the recombinative desorption in an unexcited atomic gas, without the presence of a plasma, limiting the production of vibrational states solely to recombinative desorption. For this purpose, the source SCHEME, has been designed and installed in the DESIRS beamline of Synchrotron Soleil. A detailed presentation of the source can be found in Section 3.3, along with the installed diagnostics of absorption and induced fluorescence spectroscopy using synchrotron radiation.

Similarly to ROSAE III, in order to study recombinative desorption, the presence of atomic hydrogen needs to be confirmed. The detection of atoms may be achieved by using monochromatic radiation centered in the Lyman-α transition at 10.196 eV (121.566 nm). Despite the use of a light collecting system and the lock-in amplifier, the fluorescence signal was not observed. However, the absorption line of H atoms in their ground state has been successfully obtained. This measurement confirms, as expected, that molecules are dissociated on hot filaments[167]. These atoms that are detected, are the reactants of recombinative desorption on surfaces which is the phenomenon under study. The Lyman-α absorption line is presented in Figure 4.50a while Figure 4.50b presents the pressure dependence of the Lyman-α absorbance.

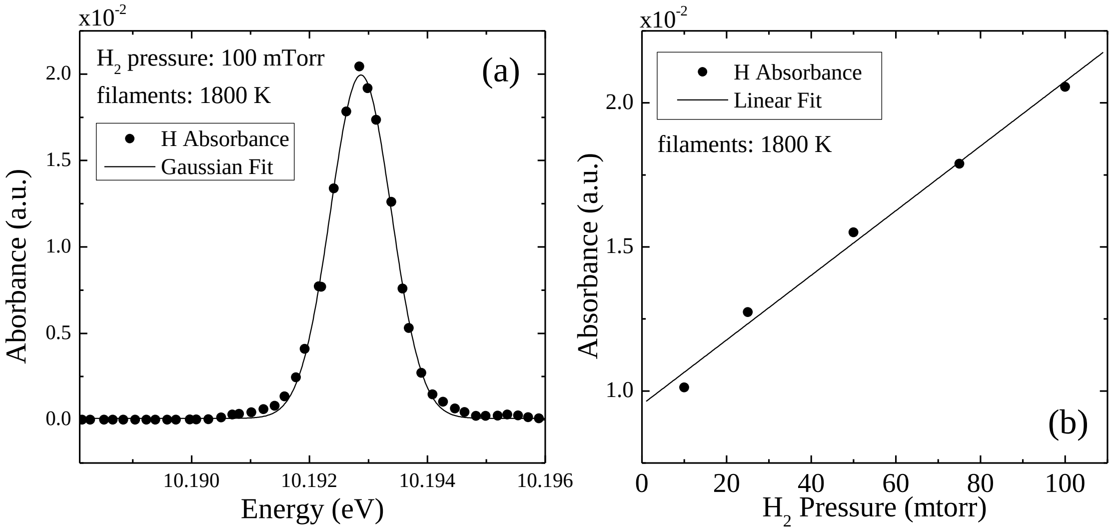

Figure 4.50. (a) Lyman-α absorption line. The pressure of H_2 is 100 mTorr and the temperature of the filaments is 1800 K. (b) Dependence of the Lyman-α absorbance on the H_2 pressure.

Figure 4.51 presents the absorption spectrum of the ground state vibrationally excited molecule $H_2\left(X^1\Sigma_g^+,v=2,J\right)$ which is around 10.419 eV. At the end of the run, filaments running previously at 1800 K were heated up to 2000 K. The increase of the absorption spectrum also presented in Figure 4.51 confirms that the density of ro-vibrationally excited molecules depends on the density of atomic hydrogen.

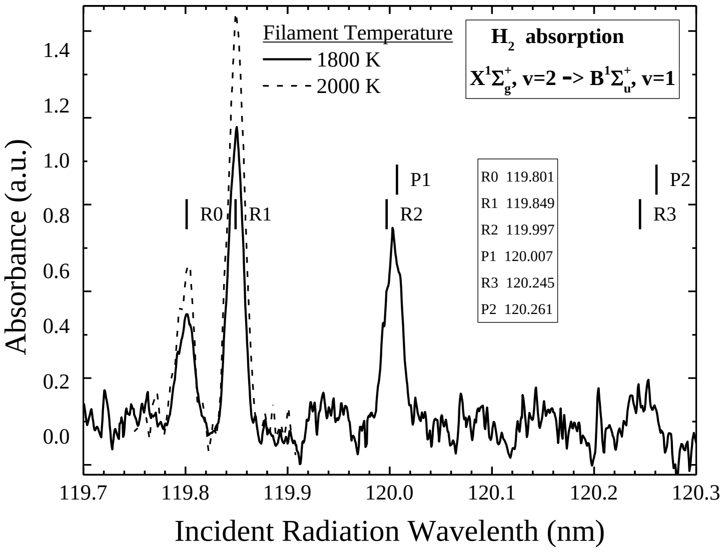

Figure 4.51. Absorption spectroscopy of vibrationally excited molecules. The pressure is 100 mTorr, the filaments have a temperature of 1800 K and the stainless steel temperature substrate has a temperature of 300 K.

More absorption measurements (chosen on the basis of favorable Franck-Condon factors[108]) have been also performed on higher excited states (v=3-5) with lower SNR due to the visible stray light of the filaments. Due to time limitations of synchrotron availability, a comparative study of various material was not realized. However, the these preliminary measurements prove a) the possibility of using synchrotron radiation for absorption diagnostics of low-pressure hydrogen plasmas and b) the presence of the mechanism of vibrational excitation through recombinative desorption in conditions relevant for negative ions production. While, further work to this direction is expected, there are always limitations related to synchrotron availability. This makes the investigations with the sources SCHEME an inherently long term project.

4.4.2 Volume production of vibrational states: EV excitation

Since no material that can enhance vibrational excitation was identified in the previous investigation, VUV emission diagnostics were employed to study the formation of vibrational states in the volume of the ECR plasma under study and its relevance to negative ion production.

For the VUV measurements the irradiance meter is used, with a filter for the Lyman band that emits around 160 nm and a filter for the molecular continuum emission which is around 180 nm. Due to the low intensity of VUV light emitted from the bulk of the plasma, the irradiance meter, which has a higher signal to noise ratio, was chosen instead of the monochromator (see Section 3.1.4). The Lyman band emission corresponds to optically allowed transitions from the first electronically excited singlet state ($B^1\Sigma_u^+$) to the ground state ($X^1\Sigma_g^+$) of the hydrogen molecule. As explained in Section 2.2.1, this processes is considered to be, together with the Werner band ($C^1\Sigma_u^+ \rightarrow X^1\Sigma_g^+$), the main production channel for vibrationally excited states. On the other hand, molecular continuum emission results in dissociation via the repulsive $b^3\Sigma_u^+$ triplet state.

These measurements are combined with electrostatic probe measurements, photodetachment and optical emission spectroscopy in order to study the negative ion production in correlation with VUV emission. For a detailed description of the used experimental setups and diagnostic techniques, the reader is referred to Section 3.1.

An important note is that due to the VUV irradiance meter that was adapted on the source, the base pressure was increased to ~10^{-6} Torr, which is about one order of magnitude higher than the usually achieved base pressure (~10^{-7} Torr). For this reason, all the electrostatic probe and laser photodetachment measurements that are presented here, were realized again, at the same time as the VUV measurements. Some small deviations in comparison to the previous values (Section 4.2), could be attributed to this difference in base pressure.

While measurements were realized in the pressure range 1-20 mTorr, here only measurements between 3 and 18 mTorr are presented. For the two lower pressures the probe curve and the photodetachment signal have a relatively low signal to noise ratio, while for the two higher the source makes a transition that was not observed before. The EEDF in this case (Figure 4.52) shows the electrons are depleted in the energy range of 3-4 eV. The underlying mechanism that is responsible for this phenomenon is not identified yet. However, it is worth mentioning that the threshold of the electron impact ionization of the H(2s) metastable is in the same energy range [78]. This is perhaps an indication of higher H(2s) densities.

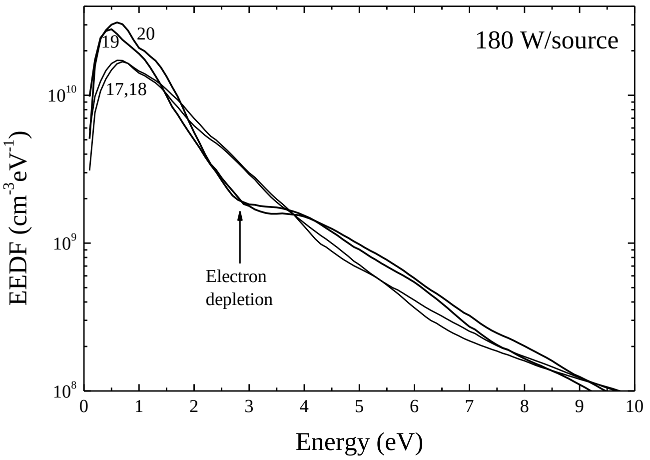

Figure 4.52. Observed EEDF for the high pressure limit of the source Prometheus I.

The first part of the study involves the operation of the source in nominal power (180 W/source) and the variation of pressure. Electrostatic probe measurements are presented in Figure 4.53. Regarding solely the DA process, the parameters of the cold electron population (Figure 4.53a and c) are optimized for 11 mTorr. Around this pressure, cold electron temperatures (Figure 4.53c) have a minimum below 0.8 eV and their density (Figure 4.53a) is near the maximum where it almost saturates. At higher pressures, the hot electron temperature is reduced and the cold electron temperature is increased. This can be attributed to an increased frequency of inelastic electron collisions that "steals" energy from hot electrons [103].

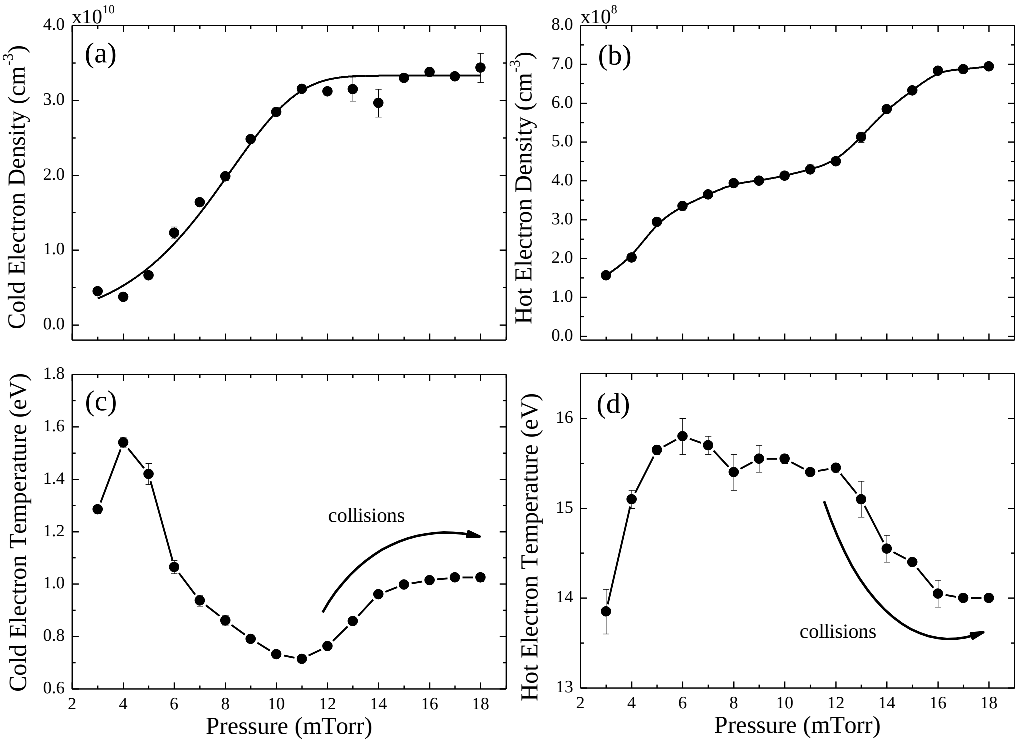

Figure 4.53. Pressure dependence of electron density and temperature. P = 180 W/source. (a) Cold electron density (b) Hot electron density, (c) Cold electron temperature and (d) Hot electron temperature.

Lyman-band and molecular continuum emissions are presented in Figure 4.54. Both emissions seem to initially saturate for pressures higher than 6 mTorr. However, at 12 mTorr they start increasing again reaching a higher saturation level. This behavior is quite consistent with the evolution of hot electron density of Figure 4.53b, indicating that it is mostly hot electrons that lead to the emission of Lyman band and molecular continuum through electron impact excitation processes.

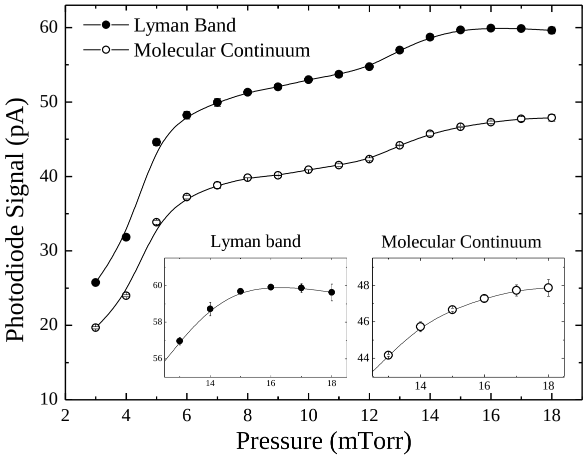

Figure 4.54. Pressure dependence of Lyman-band and molecular continuum emission.

The pressure dependence of negative ion density is presented in Figure 4.55. At about 11 mTorr, negative ions saturates, similarly to the cold electron density of Figure 4.53. Lyman band emission which corresponds to vibrational excitation, also saturates but not as sharply.

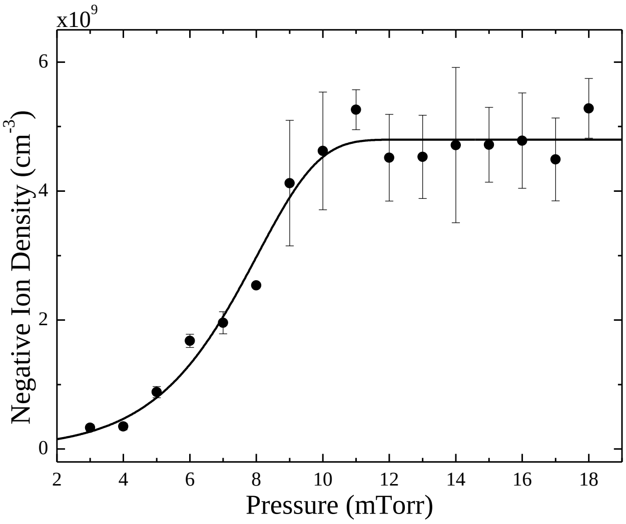

Figure 4.55. Pressure dependence of negative ion density.

For the next part of this study the pressure was kept constant (4, 8 and 12 mTorr) and the power was varied. This will demonstrate the way in which the injected power is partitioned in the various processes that relate to negative ion production. The power dependence of electron densities and temperatures are presented in Figure 4.56. Cold electron population evolves as a function of power, in a significantly different way in the case of the low pressure (4 mTorr). For higher pressures, cold electron density monotonically increases, providing more and more cold electrons for DA, while in the case of 4 mTorr, a maximum is observed around 100-120 W. At the same time, for 4 mTorr, cold electron temperature increases linearly above 90 W and reaches values above 1 eV, while, for higher pressures, it stays below 1 eV in the entire power span. Both phenomena observed for 4 mTorr are related with low DA reaction rates. On the other hand, the hot electron population behaves quite differently. For all three pressures, hot electron temperature (Figure 4.56d) is independent of both pressure and power while hot electron density increases monotonically for the entire power range (Figure 4.56b).

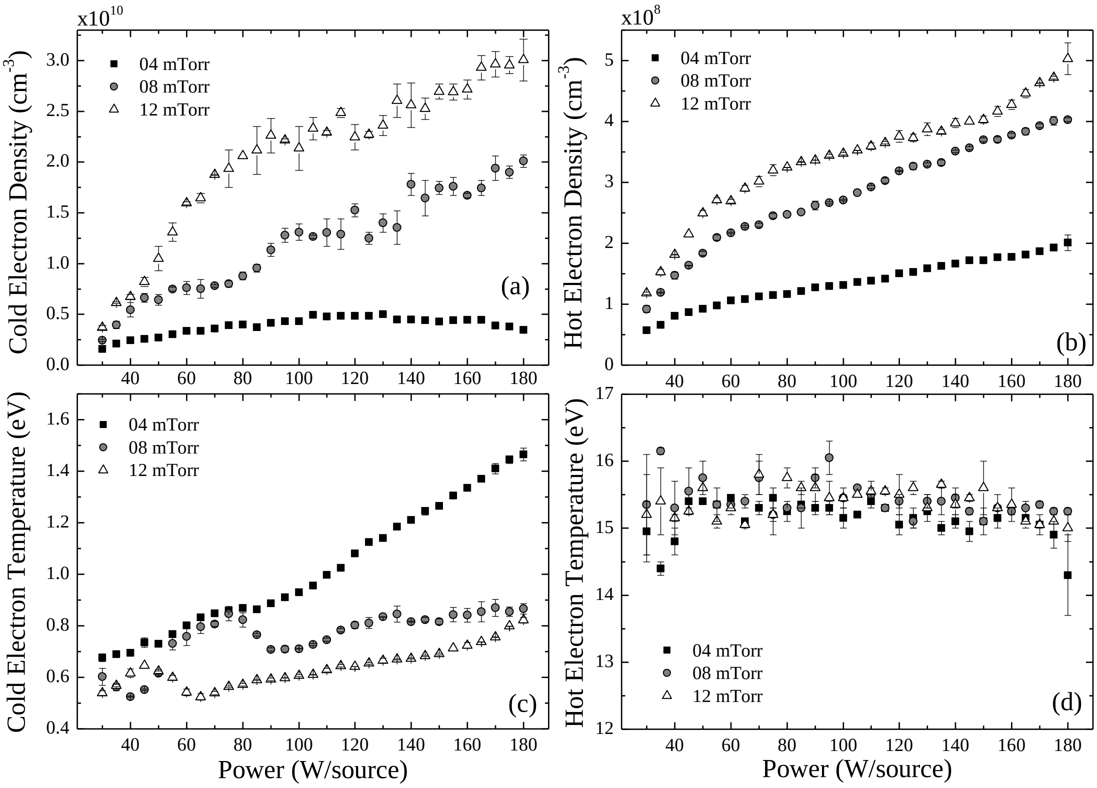

Figure 4.56. Power dependence of electron densities and temperatures. (a) Cold electron density, (b) Hot electron density, (c) Cold electron temperature and (d) Hot electron temperature.

The power dependence of Lyman-band and molecular continuum emissions is presented in Figure 4.57. Both emissions seem to increase almost linearly with no indication of saturation. For 8 and 12 mTorr and for powers up to 50-60 W, both emissions increase somewhat more abruptly. This behavior correlates well with the abrupt increase of hot electron density up to the same power (Figure 4.56b).

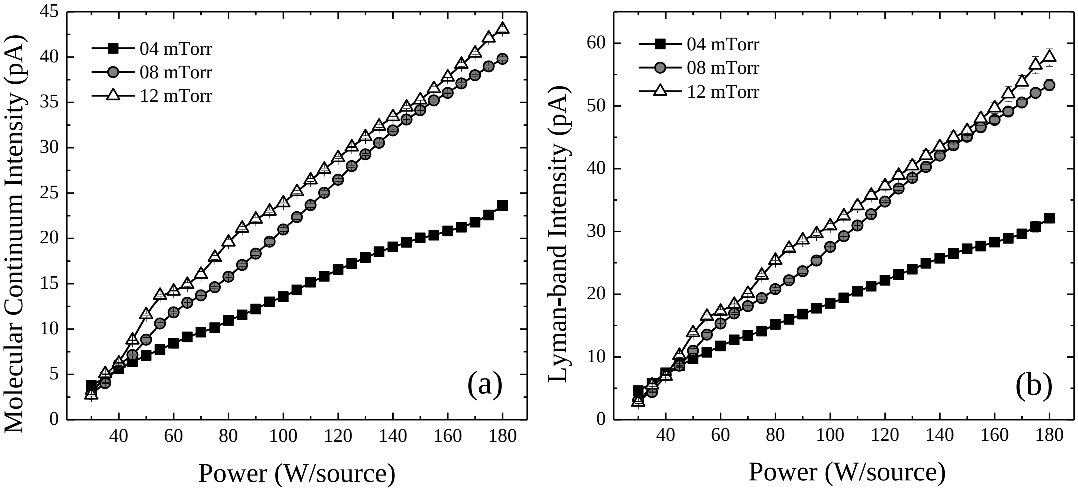

Figure 4.57. Power dependence of (a) molecular continuum and (b) Lyman band emission.

The measured negative ion density is presented in Figure 4.58a. For all three pressures, the negative ion density saturates in a manner quite similar with that of electron density (Figure 4.56a). At the same time the Lyman band emission, which is related with the formation of vibrational states, shows no sign of saturation. This is a strong indication that the negative ion density is limited by the electron density. The relative negative ion density is presented in Figure 4.58b.

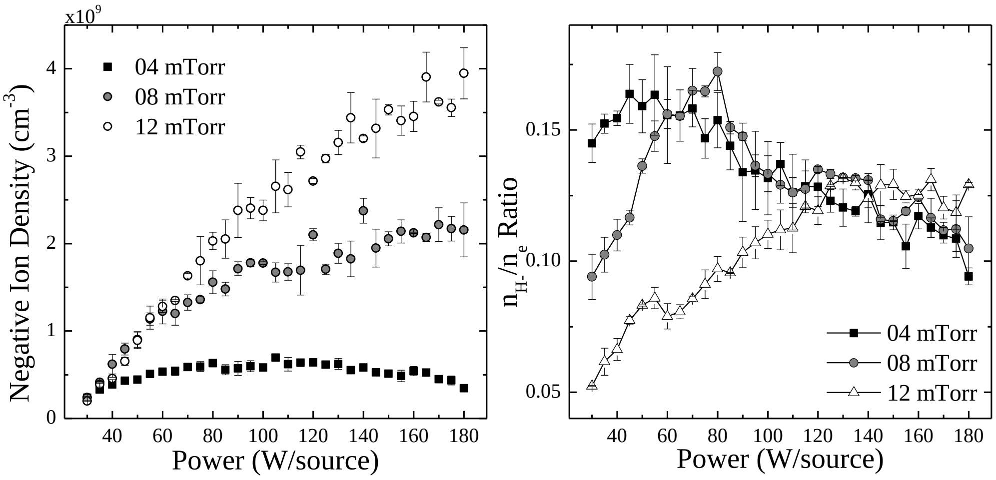

Figure 4.58. Power dependence of (a) negative ions density and (b) relative negative ion density (n_{H-}/n_e ratio).

From the results that are presented above, there are two parameters which are of particular importance for the production of negative ions. The first one is cold electrons, which is the first reactant of the DA process (Reaction (2.1)). This parameter is directly measured and is presented in Figure 4.56a. In principle, the DA rate depends also on the cold electron temperature. However, for the source parameters studied here this temperature is not reaching values higher than 1.5 eV. For typical effective vibrational temperatures (e.g. 5000-10000 K) the DA rate coefficient is not expected to change considerably for such small changes of the electron temperature (see Figure 2.5).

The other important parameter is Lyman-band emission intensity. As mentioned earlier this emission is related with the formation of vibrational states which is the other reactant of the DA process. However, Lyman band emission, depends on many plasma parameters. Transitions from the $B^1\Sigma_u^+$ singlet states to the ground state molecule are optically allowed and have very short lifetimes in the order of nanoseconds [176]. Thus, the Lyman-band emission rate is directly proportional to the electron impact excitation rate to the $B^1\Sigma_u^+$ singlet. The latter can be derived from the vibrationally resolved excitation cross sections of ground state molecules [78,164]:

$$I_{LB} \propto \sum_{v=0}^{14} n_{H_2(v)} n_e \left\langle \sigma_{XB}(v) u \right\rangle = K\left(T_{vib}, T_e\right) n_{H_2} n_e = K\left(T_{vib}\right) n_{H_2} n_{e,hot} \qquad (4.3)$$

where $n_{H2(v)}$ is the density of each vibrational state, n_e the density of electrons, σ_{XB} (v) the vibrationally resolved cross section of the $B^1\Sigma_u^+$ singlet excitation and u the velocity of electrons. $K(T_{vib},T_e)$ is a rate coefficient that depends on the effective vibrational temperature and the electron temperature, n_{H2} the total molecular density and $n_{e,hot}$ the hot electron density.

Due to the high energy threshold of the singlet excitation only the hot electron population contributes to this process. Since the temperature of the hot electron population is almost constant (Figure 4.56d), the excitation rate is equal to the right hand side of Equation (4.3). The rate coefficient K(T_{vib}) is calculated with cross sections from [78], by assuming Maxwellian VDF and an electron temperature of 15 eV (see Figure 4.56d). The calculated rate coefficient as a function of vibrational temperature is presented in Figure 4.59.

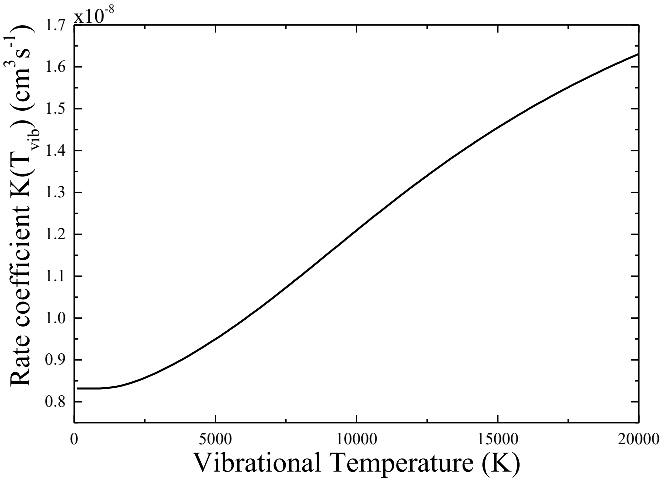

Figure 4.59. Dependence of $B^1\Sigma_u^+$ singlet excitation rate coefficient on vibrational temperature.

In a wide range of vibrational temperatures (5000-15000 K), which are relevant for low temperature plasmas [164], the rate coefficient of the $B^1\Sigma_u^+$ singlet excitation rate depends almost linearly to the vibrational temperature. If the rate coefficient can be experimentally determined, its value could be related with the vibrational temperature. However, in order to calculate this rate coefficient K(T_{vib}), the molecular and the hot electron density should be eliminated from Equation (4.3). The hot electron density is measured with the probe (Figure 4.56b). On the other hand, the density of molecular hydrogen is somewhat more complicated to calculate.

The degree of ionization is very low (~0.01%) so charged particles have negligible densities. For a completely molecular gas, the density can be calculated from the ideal gas law, knowing the pressure and the temperature. Both parameters are measured for Prometheus I. However, due to relatively intense presence of atoms (Figure 4.21), the dissociation degree needs to be considered as well. Using the diagnostic technique that is described in detail in Section 3.1.3, the ratio n_H/n_{H2} is calculated as a function of the injected power. These results are presented in Figure 4.22. Knowing the dissociation degree, the molecular gas density can be calculated from the simple relation:

$$n_{H_2} + \frac{n_H}{2} = n_g \Rightarrow n_{H_2} = n_g \left(1 + \frac{\left[{}^{n_H}\!/\!{}_{n_{H_2}} \right]}{2} \right)^{-1} \tag{4.4}$$

where n_g is the gas density determined by the ideal gas law using the gas temperature and measured pressure. Since the gas is mainly molecular (80% molecules), the gas temperatures is considered to be the estimated molecular translational temperature. The ratio between the atomic and the molecular density has been measured during the characterization of the source (see Figure 4.22). The molecular gas density is presented in Figure 4.60.

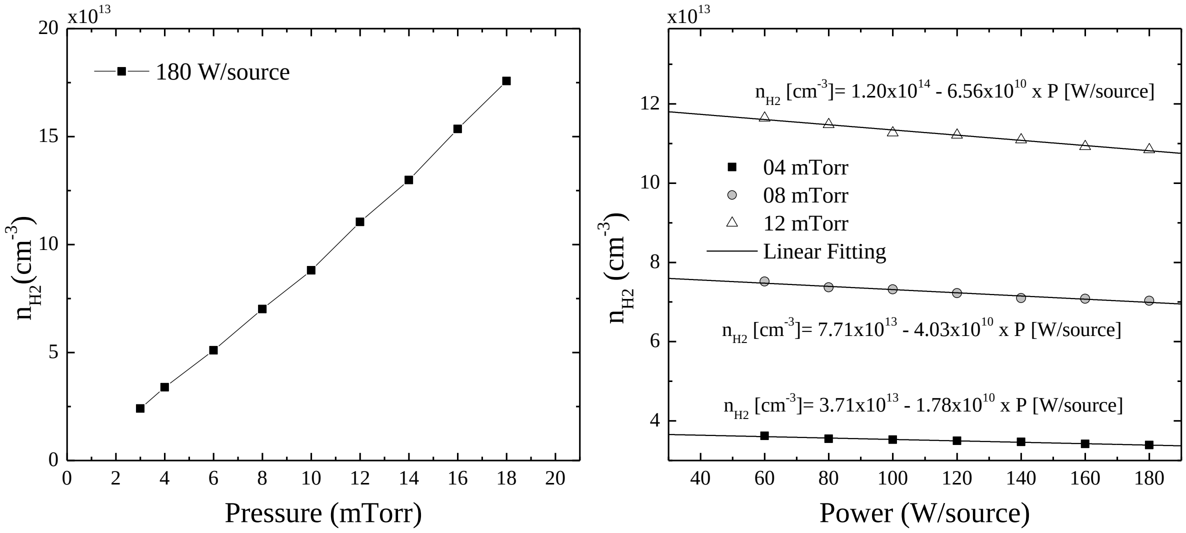

Figure 4.60. Pressure and power dependence of molecular density.

Using the density of molecules, the density of hot electron and the measured Lyman band emission, a quantity proportional to the excitation rate K(T$_{vib}$) can be calculated form equation (4.3):

$$\frac{I_{LB}}{n_{H_2} n_{e,hot}} \propto K\left(T_{vib}\right) \qquad (4.5)$$

This excitation rate coefficient can also be correlated with the vibrational temperature (Figure 4.59). The pressure and power dependence of K(T$_{vib}$) are presented in Figure 4.61. These results show that for low pressures, the excitation rate coefficient K(T$_{vib}$) and consequently the vibrational temperature are considerably higher.

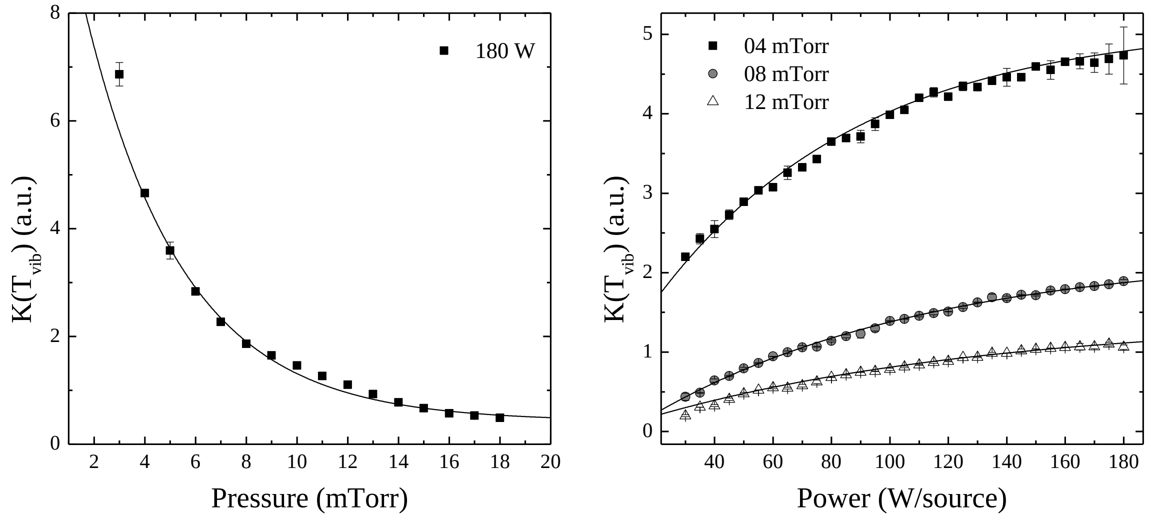

Figure 4.61. Pressure and power dependence of excitation rate to the B singlet.

Both ionization (which provides cold electrons) and singlet excitation (which leads to higher vibrational temperatures) are high energy electron impact processes [78], involving mainly the hot electron population. By plotting on an electron density - K(T$_{vib}$) plane, as presented in Figure 4.62, one can visualize on which of the two processes the hot electron population chooses to deposit its energy. Furthermore, in

Figure 4.62, each point is color-mapped according to the negative ion density, as explained in the color legend. For higher pressures, the cold electron energy is increased. Negative ions density, being limited by cold electron density is also increased (accumulated darker points in Figure 4.62). In the case of low pressures, vibrational heating seems to be dominating the hot electron energy dissipation. However, due to the lack of electrons, the higher vibrational temperatures cannot be exploited. Contrary, to what was initially expected, in the source Prometheus I, higher vibrational temperatures are not necessarily beneficial. Negative ion production, being limited by electron density is optimized for higher pressures, where the vibrational temperature is considerably reduced. For optimizing negative ion production, a balance is required between vibrational heating and ionization. For Prometheus I, increasing the density of cold electrons seems to be more beneficial than increasing the vibrational temperature.

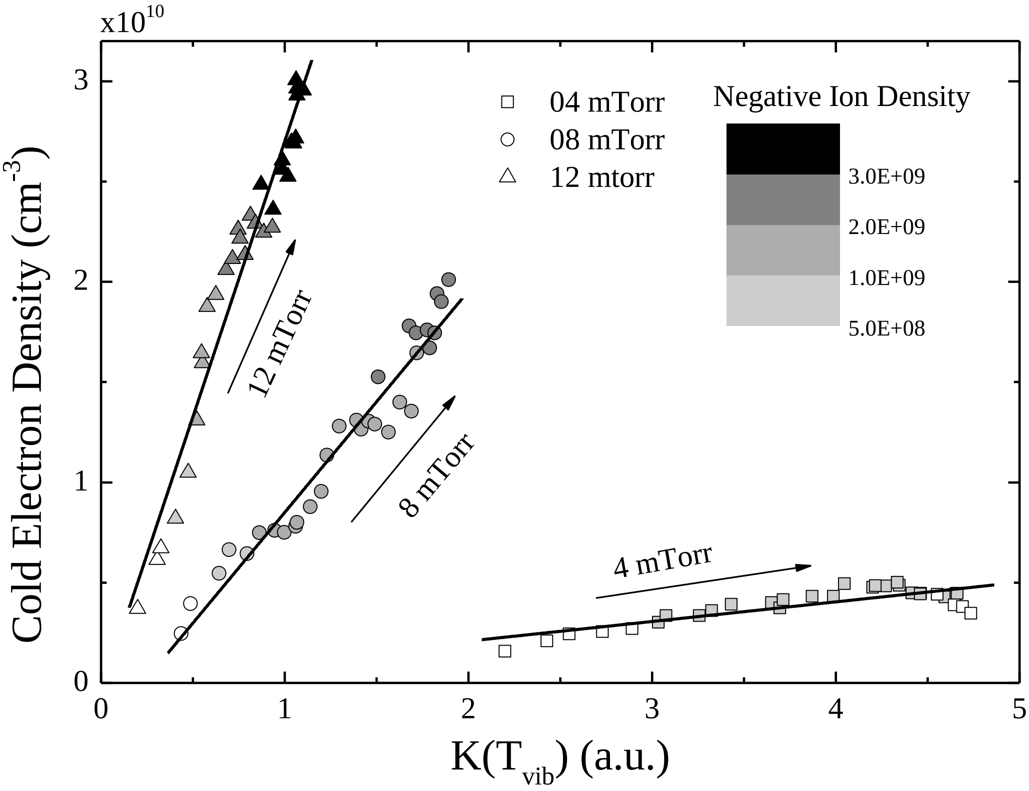

Figure 4.62. Negative ion density color-mapped on the electron density vibrational temperature plane. Instead of the actual vibrational temperature, the rate coefficient $K(T_{vib})$ is used (see Figure 4.59)

To better understand this phenomenon, the processes of ionization and singlet excitation must be considered. The main ionization channel is non-dissociative ionization [78]. Vibrationally resolved cross section of the process are found in [78]. For this qualitative calculation, the threshold of the ionization process has been considered to be the threshold for the first vibrational level (15.42 eV) reduced by the difference in vibrational energy between the considered levels. For the singlet excitation, the transitions through the $B^1\Sigma_u^+$ and $C^1\Pi_u$ singlets are considered. These transitions account for about 80% of the EV excitations [109], which is the main production channel of high vibrational states. Both processes are attributed to collisions of hot electrons with hydrogen molecules, so the excitation rate coefficients can be compared directly. In Figure 4.63 the two rate coefficients as well as the ratio between them are presented for hot electron temperature of 15 and 30 eV.

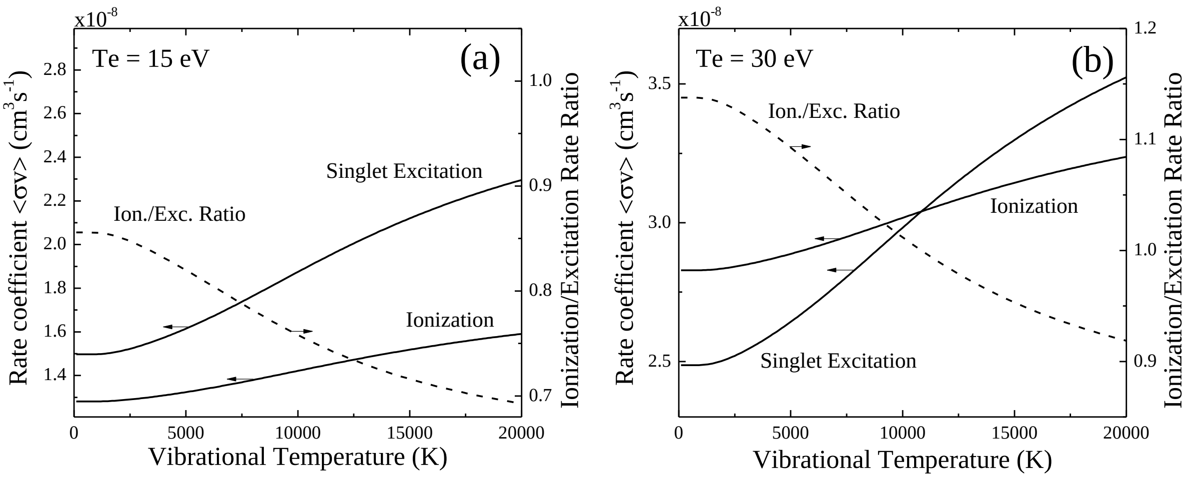

Figure 4.63. Rate coefficients of singlet excitation and ionization, as well as their ratio for electron temperatures of (a) 15 eV and (b) 30 eV. Cross sections are from [78].

Obviously, vibration temperature enhances both processes. However, singlet excitation seems to be the process that better exploits the vibrational heating. As the vibrational temperature is increased, vibrational heating is increasingly favored. For the temperature of 15 eV, which is constant for Prometheus I, this "cascade" phenomenon will always promote vibrational heating instead of ionization (Figure 4.63a). This explains why the B singlet excitation rate coefficient of Figure 4.61 increases monotonically, while the cold electron density (Figure 4.56a) is saturated or even decreased as a function of power.

For an electron temperature of 30 eV (Figure 4.63b) the ionization is favored for lower vibrational temperatures. However, once the gas is vibrationally heated the singlet excitation dominates electron impact processes. The ratio of ionization to excitation for this case is considerably increased.

The hot electron temperature appears to be a parameter that can control which of the two processes is favored. One implication of this, is that inside the ECR region, where electron heating is more efficient, this behavior might be reversed. However, in order to promote ionization, a value considerably higher than 15 eV, should be observed.

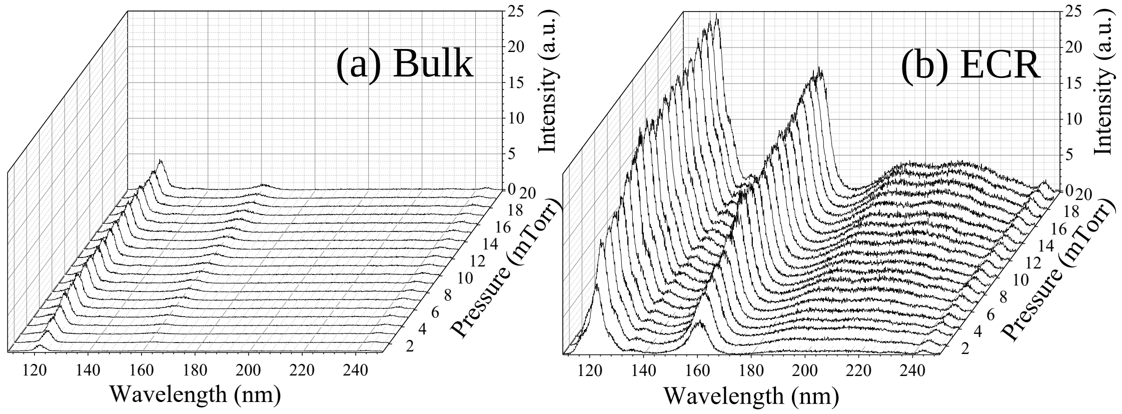

Figure 4.64. VUV emission spectra from (a) the bulk of the plasma and (b) the ECR zone.

Figure 4.64 is a comparison between the VUV spectra that is emitted from the bulk of the plasma (65 mm bellow the ECR zone midplane), and the ECR zone (3 mm above the midplane). These spectra are acquired with the experimental setup presented in Figure 3.17 (Section 3.1.4). The VUV spectrum from the

ECR zone has a significantly increased intensity. Hot electrons in this region, excite molecules to the $B^1\Sigma_u^+$ and $C^1\Pi_u$ singlet states which then decay emitting the intense molecular bands indicated in Figure 4.64. Evidently, this is the region where the majority of the high energy electron impact processes is taking place.

For an estimation of the electron temperature in the ECR zone, specially designed thin probes that can reliably measure the EEDF in the presence of strong magnetic fields are required. Such measurements have not been conducted in Prometheus I. Only as an indication, probe measurements were realized in an experimental setup that has been designed to study the electron heating scheme of the elementary ECR sources (also used in Prometheus I). This setup, which is installed in LPSC (Grenoble), consists of a single elementary dipolar source in the middle of the considerably larger chamber. The purpose of this design is to avoid any disturbance of the ECR zone. The source operates with Argon at a pressure of 2 mTorr and the injected power is 28 W. A relatively small electrostatic probe is inserted in the ECR region. The probe is 0.1 mm in diameter and 2.6 mm in length and is always perpendicular in the magnetic field.

The probe measurements inside the ECR region are presented in Figure 4.65. A single population, with a temperature of 16.8 eV, is observed (Figure 4.65b). This temperature is in agreement with other measurements realized in other ECR discharges [177]. For the measured temperature and the magnetic field of 875 G, the Larmor radius is 0.11 mm, which is not smaller than the probe radius, validates the use of the Druyvesteyn method [148].

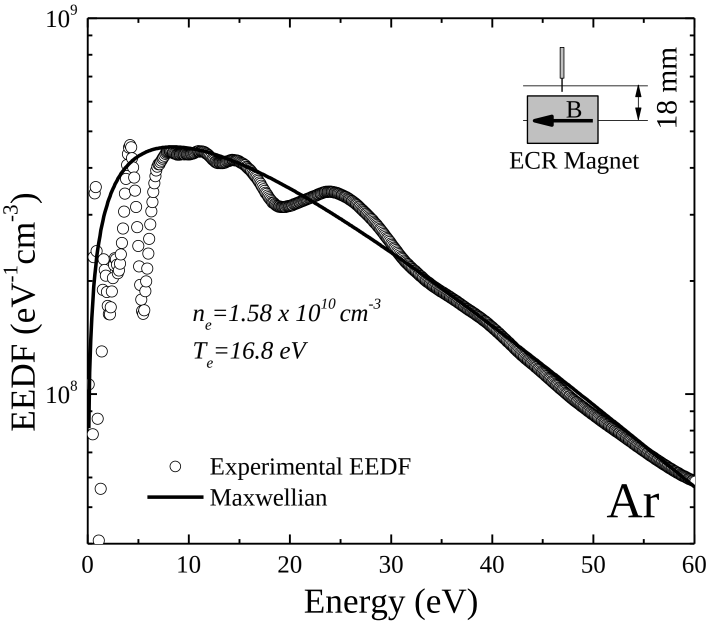

Figure 4.65. EEDF measurements inside the ECR zone of an argon discharge. The discharge power is 28 W and the pressure is 2 mTorr.

It appears that the hot electron population inside the ECR zones is denser, but not considerably hotter. Naturally, using a discharge in a different gas, might lead to some deviation. However, for a significant change in the ionization/excitation balance the temperature would be required to increase higher values, in the order of 30 eV (Figure 4.63). Consequently, it is safe to conclude that the temperature in the ECR zone is not high enough to promote ionization instead of singlet excitation.

If the electron temperature could be controlled, it could be used to optimize this sensitive balance between ionization and excitation. However, from the electrostatic probe measurements that where realized in Prometheus I (Figure 4.56), it appears that this parameter is practically constant. It seems that in the source Prometheus I, hot electron energy dissipation favors singlet excitation instead of ionization. The same conclusion was recently reached for another ECR hydrogen discharge [51]. This is perhaps an indication, that the lack of cold electrons is more universal for wave heated sources and not limited to the source that is studied here. However, this conclusion is contradicted by measurements realized in the ECR source Camembert III [56]. In that work, the electron density is increased as a function of pressure, while the negative ion production has a maximum at about 5 mTorr. It becomes evident, that this behavior of ECR plasmas requires further investigation.

In the frame of this work, this behavior explains many of the phenomena that were previously observed. Firstly it explains why the negative ions density of the source, which is measured for a wide range of parameters (Section 4.2) has a very similar evolution with the cold electron density and is optimized for high pressures. If the main limitation of negative ion production stems from limitations in the cold electron density, it will be this parameter that will effectively control negative ions density. Secondly it explains why there was no significant difference in the negative ion density when the different materials where used for the recombinative desorption study. Indeed, if the negative ion production is limited by the electron density, increasing the density of vibration states will not greatly benefit the production of negative ions. Thirdly, is explains why yttrium, a material with low work function may affect the negative ion density in such a significant manner as presented in Section 4.4. If the used ECR sources have promoted the production of vibrational states and suppressed the ionization rate, it makes sense that the negative ion density will be increased by the addition of a few electrons from the chamber walls.

However, by increasing the pressure in order to reduce the vibrational temperature, one treats the high vibrational temperatures as defect of the ion source. To turn this limitation into an advantage it necessary to increase the density of cold electrons in different way. One solution is indicated by the increased electron and negative ion density observed when a low work function material was introduced in the plasma (Figure 4.48 and Figure 4.49). A second solution would be to somehow increase the ionization rate of the source. A possible way to achieve this, is inspired by the paradoxical behavior that plasmas have, according to which the injection of hot electrons in a weakly ionized discharge plasma is cooling the main body of electron and increases their density [178]. Similar behavior has been observed in plasmas when electrons were independently injected in discharge with an energy well above the ionization threshold [179]. The injection of highly energetic electrons in the source Prometheus I, could potentially overcome this lack of cold electrons, and should most likely be one of the future perspectives.

Chapter 5. Conclusions

The ECR driven negative ion source Prometheus I was designed, fabricated and installed in the High Voltage Laboratory of the University of Patras. The diagnostics of the experimental setup include: electrostatic probes, laser photodetachment as well as optical emission spectroscopy in the visible and the vacuum ultraviolet (VUV) spectral range.

After four years of experiments, the source Prometheus I appears to have a very stable operation which provides results with good reproducibility. The same is true for the custom probe system that was developed in the frame of this work and the laser photodetachment setup.

The 2D network of dipolar ECR sources, creates a relatively homogeneous plasma which, despite some local variations, has standard deviations of plasma densities in the order of 20-30%. The negative ion density, which is optimized for higher pressures, can be as high as $5\text{x}10^{9}$ cm^{-3}. Electron densities reach the order of $3\text{-}4\text{x}10^{10}$ cm^{-3}. The relative negative ions density (n_{H-}/n_e) has a maximum of about 0.18 for nominal power (180 W/source), while it can be as high as 0.25 for lower power. The cold electron temperature mostly remains lower than 2 eV and in the high pressure range, it becomes as low as 0.5 eV. These values are quite relevant for negative ions production.

The plasma of Prometheus I was also investigated with optical emission spectroscopy in the visible spectral range (360-660 nm). This investigation revealed a relatively high degree of dissociation (>10%), which indicates that processes involving atoms might play an important role in the operation of the source. Also using OES the temperature of the atomic gas was found to be in the order of 1400-1800 K and on this basis, the temperature of the molecular gas was assumed to be in the order of 850-1100 K.

The experimental correlation of negative ion density and Lyman-α emission, was motivated by a recently proposed negative ion production mechanism (neutral resonant ionization). The observed relation between those two quantities did not indicate the importance of this mechanism for the source Prometheus I. However, a comparison of the measured negative ion density with a crude calculation of the equilibrium density of negative ions, demonstrated the dominance of the widely accepted negative on volume production channel, which is dissociative attachment of cold electrons to vibrationally excited molecules.

The formation of vibrationally excited molecules through two different channels was investigated, in correlation to negative ion production. The first channel is the recombinative desorption of atoms on the surfaces that face the plasma and the second is the radiative decay of singlet states, excited by collisions of ground state molecules with energetic electrons (EV excitation).

For the first formation process, two specially designed sources where used. The first one (ROSAE III) was used to investigate the impact of recombinative desorption from various materials, on the production of negative ions in ECR plasmas. However, this investigation was not conclusive, most likely due to another mechanism which is still dominating vibrational excitation. This motivated the conception of the source SCHEME which is used to independently investigate the recombinative desorption process using synchrotron radiation for absorption and induced fluorescence spectroscopy. During the first experimental run in Synchrotron Soleil, the concept of the source and the contribution of recombinative desorption to the production of ro-vibrational states was proved. Also, the possibility of using synchrotron radiation to detect vibrational states was demonstrated.

The second formation process (excitation to singlet states) was investigated in Prometheus I, by means of VUV emission spectroscopy. VUV measurements were correlated with electrostatic probe and laser photodetachment diagnostics. This investigation revealed and excess of vibrational states and demonstrated that negative ion production in Prometheus I is limited by cold electron density. The underlying reasons for this limitation and the possibility of this being a universal phenomenon for wave-heated discharges is discussed.

Quite typically, many of the ideas that were motivated from the realized experiments were not implemented due to time limitations. The most important one, would be the injection of high energy electrons in the ECR plasmas. This is proposed as a way to enhance the limited ionization rate of Prometheus I when working in low pressures and to overcome the limitation which is imposed by the lack of cold electrons.

Another perspective, from the practical point of view, is the extraction of the produced negative ions and the generation of a negative ion beam. The current state of the art for the modeling and the fabrication of such extraction systems has already been investigated by our group and their implementation is expected in the near future.

An extended study of the available literature on the production of negative ions has been realized and an extensive list of relevant references is provided.

References

[1] Tsuji H, Arai N, Gotoh N, Minotani T, Ishibashi T, Okumine T, Adachi K, Kotaki H, Gotoh Y and Ishikawa J 2006 Negative-ion implantation into thin SiO_2 layer for defined nanoparticle formation *Rev. Sci. Instrum.* **77** 03A510

[2] Economou D J 2007 Fundamentals and applications of ion-ion plasmas *Appl. Surf. Sci.* **253** 6672–80

[3] Aanesland A, Meige A and Chabert P 2009 Electric propulsion using ion-ion plasmas *J. Phys. Conf. Ser.* **162** 012009

[4] Alvarez L W 1951 Energy doubling in DC accelerators *Rev. Sci. Instrum.* **22** 705

[5] Budker G I and Dimov G I 1963 On the charge exchange injection of protons into ring accelerators *International Conference on High Energy Accelerators* pp 1372–7

[6] Ehlers K W 1965 Design considerations for high-intensity negative ion sources *Nucl. Instruments Methods* **32** 309–16

[7] Dimov G I 1996 Use of hydrogen negative ions in particle accelerators *Rev. Sci. Instrum.* **67** 3393

[8] Bacal M and Wada M 2015 Negative hydrogen ion production mechanisms *Appl. Phys. Rev.* **2** 021305

[9] Ehlers K W and Leung K N 1980 Multicusp negative ion source *Rev. Sci. Instrum.* **51** 721

[10] Belchenko Y 1993 Surface negative ion production in ion sources *Rev. Sci. Instrum.* **64** 1385

[11] Nicolopoulou E, Bacal M and Doucet H J 1977 Equilibrium density of H^- in a low pressure hydrogen plasma *J. Phys.* **38** 1399–404

[12] Bacal M, Nicolopoulou E and Doucet H J 1977 *Production of negative hydrogen ions in low pressure hydrogen plasmas* (Upton, N.Y. (USA))

[13] Bacal M and Hamilton G W 1979 H^- and D^- Production in Plasmas *Phys. Rev. Lett.* **42** 1538–40

[14] Anon EUROfusion

[15] McAdams R 2014 Beyond ITER: Neutral beams for a demonstration fusion reactor (DEMO) (invited) *Rev. Sci. Instrum.* **85** 02B319

[16] Stix T H 1972 Heating of toroidal plasmas by neutral injection *Plasma Phys.* **14** 367–84

[17] Franzen P and Fantz U 2014 On the NBI system for substantial current drive in a fusion power plant: Status and R&D needs for ion source and laser neutralizer *Fusion Eng. Des.* **89** 2594–605

[18] Hemsworth R, Decamps H, Graceffa J, Schunke B, Tanaka M, Dremel M, Tanga A, De Esch H P L, Geli F, Milnes J, Inoue T, Marcuzzi D, Sonato P and Zaccaria P 2009 Status of the ITER heating neutral beam system *Nucl. Fusion* **49** 045006

[19] Hemsworth R S and Inoue T 2005 Positive and negative ion sources for magnetic fusion *IEEE Trans. Plasma Sci.* **33** 1799–813

[20] Inoue T, Hanada M, Kashiwagi M, Nishio S, Sakamoto K, Sato M, Taniguchi M, Tobita K and Watanabe K 2006 Design study of a neutral beam injector for fusion DEMO plant at JAERI *Fusion Eng. Des.* **81** 1291–7

[21] Chaibi W, Blondel C, Cabaret L, Delsart C, Drag C, Simonin A, Surrey E and Simonin A 2009 Photo-neutralization of Negative Ion Beam for Future Fusion Reactor *AIP Conf. Proc.* **1097** 385–94

[22] Kovari M and Crowley B 2010 Laser photodetachment neutraliser for negative ion beams *Fusion Eng. Des.* **85** 745–51

[23] Simonin A, Christin L, de Esch H, Garibaldi P, Grand C, Villecroze F, Blondel C, Delsart C, Drag C, Vandevraye M, Brillet A, Chaibi W, Takeiri Y and Tsumori K 2011 SIPHORE: Conceptual Study of a High Efficiency Neutral Beam Injector Based on Photo-detachment for Future Fusion Reactors *AIP Conference Proceedings* vol 1390 pp 494–504

[24] Simonin A, Achard J, Achkasov K, Bechu S, Baudouin C, Baulaigue O, Blondel C, Boeuf J P, Bresteau D, Cartry G, Chaibi W, Drag C, de Esch H P L, Fiorucci D, Fubiani G, Furno I, Futtersack R, Garibaldi P, Gicquel A, Grand C, Guittienne P, Hagelaar G, Howling A, Jacquier R, Kirkpatrick M J, Lemoine D, Lepetit B, Minea T, Odic E, Revel A, Soliman B A and Teste P 2015 R&D around a photoneutralizer-based NBI system (Siphore) in view of a DEMO Tokamak steady state fusion reactor *Nucl. Fusion* **55** 123020

[25] Franzen P, Fantz U, Wünderlich D, Heinemann B, Riedl R, Kraus W, Fröschle M, Ruf B and Nocentini R 2015 Progress of the ELISE test facility: results of caesium operation with low RF

power *Nucl. Fusion* **55** 053005

[26] Antoni V, Agostinetti P, Aprile D, Cavenago M, Chitarin G, Fonnesu N, Marconato N, Pilan N, Sartori E, Serianni G and Veltri P 2014 Physics design of the injector source for ITER neutral beam injector (invited) *Rev. Sci. Instrum.* **85** 02B128

[27] Kashiwagi M, Umeda N, Tobari H, Kojima A, Yoshida M, Taniguchi M, Dairaku M, Maejima T, Yamanaka H, Watanabe K, Inoue T and Hanada M 2014 Development of negative ion extractor in the high-power and long-pulse negative ion source for fusion application *Rev. Sci. Instrum.* **85** 02B320

[28] Umeda N, Kashiwagi M, Taniguchi M, Tobari H, Watanabe K, Dairaku M, Yamanaka H, Inoue T, Kojima A and Hanada M 2014 Long-pulse beam acceleration of MeV-class H^- ion beams for ITER NB accelerator *Rev. Sci. Instrum.* **85** 02B304

[29] Takeiri Y, Tsumori K, Osakabe M, Ikeda K, Nagaoka K, Nakano H, Kisaki M, Kaneko O, Asano E, Kondo T, Sato M, Shibuya M, Komada S and Sekiguchi H 2013 Development of intense hydrogen-negative-ion source for neutral beam injectors at NIFS *AIP Conf. Proc.* **1515** 139–48

[30] Mosbach T 2005 Population dynamics of molecular hydrogen and formation of negative hydrogen ions in a magnetically confined low temperature plasma *Plasma Sources Sci. Technol.* **14** 610–22

[31] Gobin R, Auvray P, Bacal M, Breton J, Delferrière O, Harrault F, Ivanov A A, Svarnas P and Tuske O 2006 Two approaches for H^- ion production with 2.45 GHz ion sources *Nucl. Fusion* **46** S281

[32] Speth E, Falter H D, Franzen P, Fantz U, Bandyopadhyay M, Christ S, Encheva A, Froschle M, Holtum D, Heinemann B, Kraus W, Lorenz A, Martens C, McNeely P, Obermayer S, Riedl R, Suss R, Tanga A, Wilhelm R and Wunderlich D 2006 Overview of the RF source development programme at IPP Garching *Nucl. Fusion* **46** S220–38

[33] Santoso J, Manoharan R, O'Byrne S and Corr C S 2015 Negative hydrogen ion production in a helicon plasma source *Phys. Plasmas* **22** 093513

[34] Fukumasa O 1989 Numerical studies on the optimisation of volume-produced H^- ions in the single-chamber system *J. Phys. D. Appl. Phys.* **22** 1668–79

[35] Berlemont P, Skinner D A and Bacal M 1993 Negative ion volume production model: State of the experimental confirmation *Rev. Sci. Instrum.* **64** 2721

[36] Pagano D, Gorse C and Capitelli M 2007 Modeling Multicusp Negative-Ion Sources *IEEE Trans. Plasma Sci.* **35** 1247

[37] Averkin S N, Gatsonis N A and Olson L 2015 A Global Enhanced Vibrational Kinetic Model for High-Pressure Hydrogen RF Discharges *IEEE Trans. Plasma Sci.* **43** 1926–43

[38] Huh S-R, Kim N-K, Jung B-K, Chung K-J, Hwang Y-S and Kim G-H 2015 Global model analysis of negative ion generation in low-pressure inductively coupled hydrogen plasmas with bi-Maxwellian electron energy distributions *Phys. Plasmas* **22** 033506

[39] Capitelli M, Colonna G and D'Angola A 2016 *Fundamental Aspects of Plasma Chemical Physics - Kinetics* (New York: Springer)

[40] Bacal M 1989 Volume production of hydrogen negative ions *Nucl. Instruments Methods Phys. Res.* **B37/38** 28–32

[41] Hemsworth R S, Tanga A and Antoni V 2008 Status of the ITER neutral beam injection system (invited) *Rev. Sci. Instrum.* **79** 02C109

[42] Hanada M, Kojima A, Tobari H, Nishikiori R, Hiratsuka J, Kashiwagi M, Umeda N, Yoshida M, Ichikawa M, Watanabe K, Yamano Y and Grisham L R 2016 Development of the negative ion beams relevant to ITER and JT-60SA at Japan Atomic Energy Agency *Rev. Sci. Instrum.* **87** 02B322

[43] Hellblom G and Jacquot C 1986 Extraction of volume produced H^- ions from a mirror electron cyclotron resonance source *Nucl. Instruments Methods Phys. Res.* **A243** 255–9

[44] Bacal M, Ivanov A A, Rouillé C, Béchu S and Pelletier J 2004 ECR-driven multicusp volume H^- ion source *10th International Symposium of Production and Neutralization of NegativeIon Beams*

[45] Ivanov A A, Rouillé C, Bacal M, Arnal Y, Béchu S and Pelletier J 2004 H^- ion production in electron cyclotron resonance driven multicusp volume source *Rev. Sci. Instrum.* **75** 1750

[46] Schneider P J, Berkner K H, Graham W G, Pyle R V. and Stearns J W 1981 H^- and D^- production by backscattering from alkali-metal targets *Phys. Rev. B* **23** 941–8

[47] Kalvas T, Tarvainen O, Komppula J, Koivisto H, Tuunanen J, Potkins D, Stewart T and Dehnel M P 2015 A CW radiofrequency ion source for production of negative hydrogen ion beams for cyclotrons *AIP Conf. Proc.* **1655** 030015

[48] Abdrashitov G, Belchenko Y, Ivanov A S, Gusev I, Senkov D, Sanin A, Shikhovtsev I, Sotnikov O and Kondakov A 2015 Operation of RF driven negative ion source in a pure-hydrogen mode *AIP*

Conf. Proc. **1655** 040009

[49] Peng S X, Ren H T, Xu Y, Zhang T, Zhang a. L, Zhang J F, Zhao J, Guo Z Y and Chen J E 2015 CW/Pulsed H^- ion beam generation with PKU Cs-free 2.45 GHz microwave driven ion source *AIP Conf. Proc.* **1655** 070005

[50] Tamura R, Ichikawa T, Kasuya T, Nishiura M, Shimozuma T and Wada M 2015 VUV emission spectroscopy diagnostics of a 14 GHz ECR negative hydrogen ion source *AIP Conf. Proc.* **1655** 070008

[51] Komppula J, Tarvainen O, Kalvas T, Koivisto H, Kronholm R, Laulainen J and Myllyperkiö P 2015 VUV irradiance measurement of a 2.45 GHz microwave-driven hydrogen discharge *J. Phys. D. Appl. Phys.* **48** 365201

[52] Komppula J, Tarvainen O, Lätti S, Kalvas T, Koivisto H, Toivanen V and Myllyperkiö P 2013 VUV-diagnostics of a filament-driven arc discharge H^- ion source *AIP Conf. Proc.* **1515** 66–73

[53] Etoh H, Onai M, Aoki Y, Mitsubori H, Arakawa Y, Sakuraba J, Kato T, Mitsumoto T, Hiasa T, Yajima S, Shibata T, Hatayama A and Okumura Y 2016 High current DC negative ion source for cyclotron *Rev. Sci. Instrum.* **87** 02B135

[54] Christ-Koch S, Fantz U and Berger M 2009 Laser photodetachment on a high power, low pressure rf-driven negative hydrogen ion source *Plasma Sources Sci. Technol.* **18** 025003

[55] Courteille C, Bruneteau A M and Bacal M 1995 Investigation of a large volume negative hydrogen ion source *Rev. Sci. Instrum.* **66** 2533

[56] Svarnas P, Breton J, Bacal M and Mosbach T 2006 Pressure optimization for H^- ion production in an electron cyclotron resonance-driven and a filamented source *Rev. Sci. Instrum.* **77** 03A532

[57] Leung K N, Ehlers K W and Bacal M 1983 Extraction of volume-produced H^- ions from a multicusp source *Rev. Sci. Instrum.* **54** 56–61

[58] Bacal M, Sasao M, Wada M and McAdams R 2015 Roles of a plasma grid in a negative hydrogen ion source *AIP Conf. Proc.* **1655** 020001

[59] Svarnas P, Breton J, Bacal M and Faulkner R 2007 Plasma Electrode Bias Effect on the H^- Negative-Ion Density in an Electron Cyclotron Resonance Volume Source *IEEE Trans. Plasma Sci.* **35** 1156–62

[60] Bacal M, Svarnas P, Bechu S and Pelletier J 2009 Study of the plasma near the plasma electrode by probes and photodetachment in ECR-driven negative ion source *AIP Conf. Proc.* **1097** 47–54

[61] Svarnas P, Annaratone B M, Béchu S, Pelletier J and Bacal M 2009 Study of hydrogen plasma in the negative-ion extraction region *Plasma Sources Sci. Technol.* **18** 045010

[62] Kalvas T 2013 *Development and use of computational tools for modelling negative hydrogen ion source extraction systems* (University of Jyvaskyla)

[63] Wadehra J M 1984 Dissociative attachment to rovibrationally excited H_2 *Phys. Rev. A* **29** 106–10

[64] Chung K-J, Jung B-K, An Y, Dang J-J and Hwang Y S 2014 Effects of discharge chamber length on the negative ion generation in volume-produced negative hydrogen ion source. *Rev. Sci. Instrum.* **85** 02B119

[65] Boeuf J P, Chaudhury B and Garrigues L 2012 Physics of a magnetic filter for negative ion sources. I. Collisional transport across the filter in an ideal, 1D filter *Phys. Plasmas* **19** 113509

[66] Boeuf J P, Claustre J, Chaudhury B and Fubiani G 2012 Physics of a magnetic filter for negative ion sources. II. E × B drift through the filter in a real geometry *Phys. Plasmas* **19** 113510

[67] Lacoste A, Lagarde T, Béchu S, Arnal Y and Pelletier J 2002 Multi-dipolar plasmas for uniform processing: physics, design and performance *Plasma Sources Sci. Technol.* **11** 407–12

[68] Vogel J S 2015 H^- Formation by Neutral Resonant Ionization of H(n=2) Atoms *AIP Conf. Proc.* **1655** 020015

[69] Huashun Zhang *Ion Sources*

[70] Prelec K 1973 Formation of Negative Hydrogen Ions in Direct Extraction Sources *Rev. Sci. Instrum.* **44** 1451

[71] Bardsley J N 1968 Configuration interaction in the continuum states of molecules *J. Phys. B At. Mol. Phys.* **1** 303

[72] O'Malley T F 1966 Theory of Dissociative Attachment *Phys. Rev.* **150** 14–29

[73] Schulz G J 1973 Resonances in Electron Impact on Diatomic Molecules *Rev. Mod. Phys.* **45** 423–86

[74] Wadehra J M and Bardsley J N 1978 Vibrational- and Rotational-State Dependence of Dissociative Attachment in e-H_2 Collisions *Phys. Rev. Lett.* **41** 1795–8

[75] Bardsley J N and Wadehra J M 1979 Dissociative attachment and vibrational excitation in low-energy collisions of electrons with H_2 and D_2 *Phys. Rev. A* **20** 1398

[76] Allan M and Wong S F 1978 Effect of Vibrational and Rotational Excitation on Dissociative Attachment in Hydrogen *Phys. Rev. Lett.* **41** 1791

[77] Celiberto R, Janev R K, Laricchiuta A, Capitelli M, Wadehra J M and Atems D E 2001 Cross Section Data for Electron-Impact Inelastic Processes of Vibrationally Excited Molecules of Hydrogen and Its Isotopes *At. Data Nucl. Data Tables* **77** 161–213

[78] Janev R K, Reiter D and Samm U 2003 *Collision Processes in Low-Temperature Hydrogen Plasmas* (Forschungszentrum Jülich Report Jül-4105)

[79] Gauyacq H P 1985 Dissociative attachment in e^--H_2 collisions *J. Phys. B At. Mol. Phys.* **18** 1859–72

[80] Cízek M, Horácek J and Domcke W 1998 Nuclear dynamics of the H_2- collision complex beyond the local approximation: associative detachment and dissociative attachment to rotationally and vibrationally excited molecules *J. Phys. B At. Mol. Opt. Phys.* **31** 2571–83

[81] Horáček J, Čížek M, Houfek K, Kolorenč P and Domcke W 2004 Dissociative electron attachment and vibrational excitation of H_2 by low-energy electrons: Calculations based on an improved nonlocal resonance model *Phys. Rev. A* **70** 052712

[82] Vankan P 2005 *Molecules and atoms in a hydrogen plasma expansion* (Eindhoven University of Technology)

[83] Bottcher C and Buckley B D 1979 Dissociative electron attachment to the metastable $c^3\Pi_u$ state of molecular hydrogen *J. Phys. B At. Mol. Phys.* **12** L497–500

[84] Hassouni K, Gicquel A and Capitelli M 1998 The role of dissociative attachment from Rydberg states in enhancing H^- concentration in moderate- and low-pressure H_2 plasma sources *Chem. Phys. Lett.* **290** 502–8

[85] Hiskes J R 1996 Molecular Rydberg states in hydrogen negative ion discharges *Appl. Phys. Lett.* **69** 755

[86] Behringer K and Fantz U 2000 The influence of opacity on hydrogen excited-state population and applications to low-temperature plasmas *New J. Phys.* **2** 23

[87] Vogel J S 2016 Neutral resonant ionization in a H^- plasma source: Potential of doubly excited **H^- *Rev. Sci. Instrum.* **87** 02A503

[88] Fite W L, Brackmann R T, Hummer D G and Stebbings R F 1959 Lifetime of the 2S State of Atomic Hydrogen *Phys. Rev.* **116** 363–7

[89] Drake G W F 1970 Second bound state for the hydrogen negative ion *Phys. Rev. Lett.* **24** 126–7

[90] Woodcock K S 1931 The Emission of Negative Ions under the Bombardment of Positive Ions *Phys. Rev.* **38** 1696–703

[91] Belchenko Y I, Dimov G I and Dudnikov V G 1974 A powerful injector of neutrals with a surface-plasma source of negative ions *Nucl. Fusion* **14** 113

[92] van Os C F A, Granneman E H A and van Amersfoort P W 1987 The role of cesium-ion bombardment in the formation of negative hydrogen ions on a converter surface *J. Appl. Phys.* **61** 5000

[93] van Os C F A, Kunkel W B, Leguijt C and Los J 1991 Modeling of H^- surface conversion sources; binary (H-Ba) and ternary (H-Cs/W) converter arrangements *J. Appl. Phys.* **70** 2575

[94] Schiesko L, Carrère M, Layet J-M and Cartry G 2010 A comparative study of H^- and D^- production on graphite surfaces in H_2 and D_2 plasmas *Plasma Sources Sci. Technol.* **19** 045016

[95] Schiesko L, Carrère M, Cartry G and Layet J M 2008 H^- production on a graphite surface in a hydrogen plasma *Plasma Sources Sci. Technol.* **17** 035023

[96] Kumar P, Ahmad A, Pardanaud C, Carrère M, Layet J M, Cartry G, Silva F, Gicquel A and Engeln R 2011 Enhanced negative ion yields on diamond surfaces at elevated temperatures *J. Phys. D. Appl. Phys.* **44** 372002

[97] Hopman H J, Zeijlemaker H and Verhoeven J 2001 Secondary electron emission data of cesiated oxygen free high conductivity copper(II) *Appl. Surf. Sci.* **171** 197–206

[98] Laulainen J, Kalvas T, Koivisto H, Komppula J, Kronholm R and Tarvainen O 2016 Photoelectron emission from metal surfaces induced by radiation emitted by a 14 GHz electron cyclotron resonance ion source *Rev. Sci. Instrum.* **87** 02A506

[99] Steen P G and Graham W G 1999 Negative ion enhancement in caesium-seeded hydrogen discharges—a volume or surface effect? *Appl. Phys. Lett.* **75** 2737

[100] Matveyev A A and Silakov V P 1995 Kinetic processes in a highly-ionized non-equilibrium

hydrogen plasma *Plasma Sources Sci. Technol.* **4** 606–17

[101] Hjartarson A T, Thorsteinsson E G and Gudmundsson J T 2010 Low pressure hydrogen discharges diluted with argon explored using a global model *Plasma Sources Sci. Technol.* **19** 065008

[102] Eerden M J J, van de Sanden M C M, Otorbaev D K and Schram D C 1995 Cross section for the mutual neutralization reaction H^{2+}+H^-, calculated in a multiple-crossing Landau-Zener approximation *Phys. Rev. A* **51** 3362–5

[103] Hopkins M B, Bacal M and Graham W G 1991 Electron energy distribution functions and negative ion concentrations in tandem and hybrid multicusp negative hydrogen ion sources *J. Phys. D. Appl. Phys.* **24** 268–76

[104] Ivanov A A 2004 Two negative ion groups in volume H^- sources *Rev. Sci. Instrum.* **75** 1754

[105] Capitelli M, Celiberto R, Esposito F, Laricchiuta A, Hassouni K and Longo S 2002 Elementary processes and kinetics of H_2 plasmas for different technological applications *Plasma Sources Sci. Technol.* **11** A7–25

[106] Yoon J, Song M, Han J, Hwang S H, Chang W and Lee B 2008 Cross Sections for Electron Collisions with Hydrogen Molecules *J. Phys. Chem. Ref. Data* **37** 913–31

[107] Capitelli M, Cacciatore M, Celiberto R, Pascale O De, Diomede P, Esposito F, Gicquel A, Gorse C, Hassouni K, Laricchiuta A, Longo S, Pagano D and Rutigliano M 2006 Vibrational kinetics, electron dynamics and elementary processes in H_2 and D_2 plasmas for negative ion production: modelling aspects *Nucl. Fusion* **46** S260–74

[108] Fantz U and Wünderlich D 2006 Franck-Condon factors, transition probabilities, and radiative lifetimes for hydrogen molecules and their isotopomeres *At. Data Nucl. Data Tables* **92** 853–973

[109] Hiskes J R 1991 Cross sections for the vibrational excitation of the H_2 $X^1\Sigma_g^+(v)$ levels generated by electron collisional excitation of the higher singlet states *J. Appl. Phys.* **70** 3409

[110] Mosbach T, Katsch H and Döbele H F 2000 In situ Diagnostics in Plasmas of Electronic-Ground-State Hydrogen Molecules in High Vibrational and Rotational States by Laser-Induced Fluorescence with Vacuum-Ultraviolet Radiation *Phys. Rev. Lett.* **85** 3420

[111] Gorse C, Capitelli M, Bacal M, Bretagne J and Lagana A 1987 Progress in the non-equilibrium vibrational kinetics of hydrogen in magnetic multicusp H^- ion sources *Chem. Phys.* **117** 177–95

[112] Ichihara A, Iwamoto O and Janev R K 2000 Cross sections for the reaction H^++H_2(v=0-14) →H + H_2^+ at low collision energies *J. Phys. B At. Mol. Opt. Phys.* **33** 4747–58

[113] Hiskes J R and Karo A M 1989 Analysis of the H_2 vibrational distribution in a hydrogen discharge *Appl. Phys. Lett.* **54** 508

[114] Bacal M 2006 Physics aspects of negative ion sources *Nucl. Fusion* **46** S250–9

[115] Muiño R D and Busnengo H F 2013 *Dynamics of Gas-Surface Interactions: Atomic-level Understanding of Scattering Processes at Surfaces* (Berlin, Heidelberg: Springer-Verlag)

[116] Harris J and Kasemo B 1981 On precursor mechanisms for surface reactions *Surf. Sci. Lett.* **105** L281–7

[117] Billing G D 1982 On a semiclassical approach to energy transfer by atom/molecule-surface collisions *Chem. Phys.* **70** 223–39

[118] Billing G D 1990 The dynamics of molecule-surface interaction *Comput. Phys. Reports* **12** 383–450

[119] Čadež I, Markelj S, Rupnik Z and Pelicon P 2008 Processes with neutral hydrogen and deuterium molecules relevant to edge plasma in tokamaks *J. Phys. Conf. Ser.* **133** 012029

[120] Rutigliano M and Cacciatore M 2011 Eley–Rideal recombination of hydrogen atoms on a tungsten surface *Phys. Chem. Chem. Phys.* **13** 7475

[121] Latimer E R, Islam F and Price S D 2008 Studies of HD formed in excited vibrational states from atomic recombination on cold graphite surfaces *Chem. Phys. Lett.* **455** 174–7

[122] Le Bourlot J, Le Petit F, Pinto C, Roueff E and Roy F 2012 Surface chemistry in the interstellar medium - I. H_2 formation by Langmuir-Hinshelwood and Eley-Rideal mechanisms *Astron. Astrophys.* **541** A76

[123] Popov O A 1994 Electron Cyclotron Resonance Plasma Sources and Their Use in Plasma-Assisted Chemical Vapor Deposition of Thin Films *Physics of Thin Films - Volume 18: Plasma Sources for Thin Film Deposition and Etching* ed M H Francombe and J L Vossen (San Diego: Academic Press, Inc) pp 121–233

[124] Béchu S, Soum-Glaude A, Bès A, Lacoste A, Svarnas P, Aleiferis S, Ivanov A A and Bacal M 2013 Multi-dipolar microwave plasmas and their application to negative ion production *Phys. Plasmas*

20 101601

[125] Lax B, Allis W P and Brown S C 1950 The Effect of Magnetic Field on the Breakdown of Gases at Microwave Frequencies *J. Appl. Phys.* **21** 1297

[126] Kelly D C, Margenau H and Brown S C 1957 Cyclotron Resonance: Method for Determining Collision Cross Sections for Low-Energy Electrons *Phys. Rev.* **108** 1367–71

[127] Brown S C 1959 The Interaction of Microwaves with Gas-Discharge Plasmas *IEEE Trans. Microw. Theory Tech.* **7** 69–72

[128] Ericson M, Ward C S, Brown S C and Buchsbaum S J 1962 Containment of Plasmas by High-Frequency Electric Fields *J. Appl. Phys.* **33** 2429

[129] Musil J and Zacek F 1971 Penetration of a strong electromagnetic wave in an inhomogeneous plasma generated by ECR using a magnetic beach *Plasma Phys.* **13** 471–6

[130] Tamagawa H, Okamoto Y and Akutagawa C 1972 A Proposal on Multiply Charged Ion Source *Jpn. J. Appl. Phys.* **11** 1226–7

[131] Suzuki K, Okudaira S, Sakudo N and Kanomata I 1977 Microwave Plasma Etching *Jpn. J. Appl. Phys.* **16** 1979–84

[132] Maekawa T, Kobayashi T, Yamaguchi S, Yoshinaga K, Igami H, Uchida M, Tanaka H, Asakawa M and Terumichi Y 2001 Doppler-Shifted Cyclotron Absorption of Electron Bernstein Waves via N∥-Upshift in a Tokamak Plasma *Phys. Rev. Lett.* **86** 3783–6

[133] Boswell R W 1984 Very efficient plasma generation by whistler waves near the lower hybrid frequency *Plasma Phys. Control. Fusion* **26** 1147–62

[134] Musil J and Žáček F 1972 *Absorption of Microwave Energy in Magnetoactive Plasma* (Prague)

[135] Tsai C C 1990 Potential applications of an electron cyclotron resonance multicusp plasma source *J. Vac. Sci. Technol. A Vacuum, Surfaces, Film.* **8** 2900

[136] Stix T H *Waves in Plasmas*

[137] Motley R W, Bernabei S, Hooke W M and Jassby D L 1975 Electrostatically driven overdense rf plasma source *J. Appl. Phys.* **46** 3286

[138] Messiaen A M and Vandenplas P E 1962 Comparison of experiments with the theoretical scattering behaviour of a cold plasma cylinder (or anisotropic dielectric rod) with a magnetically induced anisotropy and inhomogeneity *Phys. Lett.* **2** 193–6

[139] Lichtenberg A J, Schwartz M J and Tuma D T 1969 Non-adiabatic and stochastic mechanisms for cyclotron resonance trapping and heating in mirror geometries *Plasma Phys.* **11** 101–16

[140] Golant V E and Piliya A D 1972 Linear Transformation and Absorption of Waves in a Plasma *Sov. Phys. Uspekhi* **14** 413–37

[141] Lieberman M A and Lichteberg A J *Principles of Plasma Discharges and Materials Processing*

[142] Jacques P 1996 Distributed ECR Plasma Sources *High Density Plasma Sources: Design Physics and Performance* ed O A Popov pp 380–425

[143] Latrasse L, Lacoste A, Sirou J and Pelletier J 2007 High density distributed microwave plasma sources in a matrix configuration: concept, design and performance *Plasma Sources Sci. Technol.* **16** 7–12

[144] Hagelaar G J M, Makasheva K, Garrigues L and Boeuf J-P 2009 Modelling of a dipolar microwave plasma sustained by electron cyclotron resonance *J. Phys. D. Appl. Phys.* **42** 194019

[145] Bacal M 2000 Photodetachment diagnostic techniques for measuring negative ion densities and temperatures in plasmas *Rev. Sci. Instrum.* **71** 3981

[146] Aleiferis S and Svarnas P 2014 Automated electrostatic probe device of high resolution and accuracy *Rev. Sci. Instrum.* **85** 123504

[147] Aanesland A, Bredin J, Chabert P and Godyak V 2012 Electron energy distribution function and plasma parameters across magnetic filters *Appl. Phys. Lett.* **100** 044102

[148] Godyak V A and Demidov V I 2011 Probe measurements of electron-energy distributions in plasmas: what can we measure and how can we achieve reliable results? *J. Phys. D. Appl. Phys.* **44** 233001

[149] Hershkowitz N 1989 How Langmuir Probes Work *Plasma Diagnostics: Volume 1, Discharge Parameters and Chemistry* ed O Auciello and D Flamm (San Diego: Academic Press) p 113

[150] Druyvesteyn M J 1930 Der Niedervoltbogen *Zeitschrift für Phys.* **64** 781–98

[151] Savitzky A and Golay M J E 1964 Smoothing and Differentiation fo Data by Simplified Least Squares Procedures *Anal. Chem.* **36** 1627–39

[152] Hopkins M B and Graham W G 1987 Electron energy distribution function measurements in a magnetic multipole plasma *J. Phys. D. Appl. Phys.* **20** 838–43

[153] Bryant P M and Bradley J W 2013 Optimum circuit design for the detection of laser photodetachment signals *Plasma Sources Sci. Technol.* **22** 015014

[154] Dodd R, You S-D, Bryant P M and Bradley J W 2010 Negative ion density measurements in a reactive dc magnetron using the eclipse photodetachment method *Plasma Sources Sci. Technol.* **19** 015021

[155] Fantz U and Heger B 1998 Spectroscopic diagnostics of the vibrational population in the ground state of molecules *Plasma Phys. Control. Fusion* **40** 2023–32

[156] Fantz U, Falter H, Franzen P, Wunderlich D, Berger M, Lorenz A, Kraus W, Mcneely P, Riedl R and Speth E 2006 Spectroscopy — a powerful diagnostic tool in source development *Nucl. Fusion* **46** S297

[157] Tomasini L, Rousseau A, Gousset G and Leprince P 1999 Spectroscopic temperature measurements in a H_2 microwave discharge *J. Phys. D. Appl. Phys.* **29** 1006–13

[158] Kasap S O 2006 *Principles of electronic materials and devices* (New York: McGraw-Hill)

[159] Tatarova E, Felizardo E, Dias F M, Lino da Silva M, Ferreira C M and Gordiets B 2009 Hot and super-hot hydrogen atoms in microwave plasma *Appl. Phys. Lett.* **95** 181503

[160] Péalat M, Taran J-P E, Bacal M and Hillion F 1985 Rovibrational molecular populations, atoms, and negative ions in H_2 and D_2 magnetic multicusp discharges *J. Chem. Phys.* **82** 4943

[161] Bruneteau A M, Hollos G, Bacal M and Bretagne J 1990 Temperature and relative density of atomic hydrogen in a multicusp H^- volume source *J. Appl. Phys.* **67** 7254

[162] Lavrov B P, Lang N, Pipa A V and Röpcke J 2006 On determination of the degree of dissociation of hydrogen in non-equilibrium plasmas by means of emission spectroscopy: II. Experimental verification *Plasma Sources Sci. Technol.* **15** 147–55

[163] Lavrov B P, Pipa A V and Röpcke J 2006 On determination of the degree of dissociation of hydrogen in non-equilibrium plasmas by means of emission spectroscopy: I. The collision-radiative model and numerical experiments *Plasma Sources Sci. Technol.* **15** 135–46

[164] Komppula J and Tarvainen O 2015 VUV diagnostics of electron impact processes in low temperature molecular hydrogen plasma *Plasma Sources Sci. Technol.* **24** 045008

[165] Wise H and Wood B J 1967 Reactive collisions between gas and surface atoms *Advances in Atomic and Molecular Physics - Volume 3* ed D R Bates and I Estermann (Academic Press) p 291

[166] Nahon L, de Oliveira N, Garcia G A, Gil J-F, Pilette B, Marcouillé O, Lagarde B and Polack F 2012 DESIRS: a state-of-the-art VUV beamline featuring high resolution and variable polarization for spectroscopy and dichroism at SOLEIL *J. Synchrotron Radiat.* **19** 508–20

[167] Livshits A I, Balghiti F E and Bacal M 1994 Dissociation of hydrogen molecules on metal filaments in H^- ion sources *Plasma Sources Sci. Technol.* **3** 465–72

[168] Mosbach T 2005 Effects of foreign gases on H^- formation in a magnetic multipole hydrogen plasma source *Plasma Sources Sci. Technol.* **14** 351–62

[169] Popov O A 1994 Electron Cyclotron Resonance Plasma Sources and Their Use in Plasma-Assisted Chemical Vapor Deposition of Thin Films *Physics of Thin Films - Volume 18: Plasma Sources for Thin Film Deposition and Etching* ed M H Francombe and J L Vossen (San Diego: Academic Press) pp 121–233

[170] Chen F F 2003 *Lecture Notes on Langmuir Probe Diagnostics*

[171] Fantz U and Wünderlich D 2006 A novel diagnostic technique for H^- (D^-) densities in negative hydrogen ion sources *New J. Phys.* **8** 301–301

[172] Rousseau A, Tomasini L, Gousset G, Boisse-Laporte C and Leprince P 1994 Pulsed microwave discharge: a very efficient H atom source *J. Phys. D. Appl. Phys.* **27** 2439–41

[173] Dose V and Richard A 1981 Collision induced Lyman-alpha emission from metastable hydrogen *J. Phys. B At. Mol. Phys.* **14** 63–72

[174] Bacal M, Ivanov A A, Glass-Maujean M, Matsumoto Y, Nishiura M, Sasao M and Wada M 2004 Contribution of wall material to the vibrational excitation and negative ion formation in hydrogen negative ion sources (invited) *Rev. Sci. Instrum.* **75** 1699

[175] Komppula J 2015 *VUV-Diagnostics of Low Temperature Hydrogen Plasmas* (University of Jyvaskyla)

[176] Astashkevich S A and Lavrov B P 2002 Lifetimes of the electronic-vibrational-rotational states of hydrogen molecule (Review) *Opt. Spectrosc.* **92** 818–50

[177] Lagarde T, Arnal Y, Lacoste A and Pelletier J 2001 Determination of the EEDF by Langmuir probe diagnostics in a plasma excited at ECR above a multipolar magnetic field *Plasma Sources Sci.*

Technol. **10** 181

[178] Godyak V A 2006 Nonequilibrium EEDF in gas discharge plasmas *IEEE Trans. Plasma Sci.* **34** 755–66

[179] Haas F A, Goodyear A and Braithwaite N S J 1999 Tailoring of electron energy distributions in low temperature plasmas *Plasma Sources Sci. Technol.* **7** 471–7

[180] Laulainen J, Kalvas T, Koivisto H, Komppula J and Tarvainen O 2015 Photoelectron emission from metal surfaces induced by VUV-emission of filament driven hydrogen arc discharge plasma *AIP Conf. Proc.* **1655** 020007

List of current publications

Peer-Reviewed Scientific Journals

1. Multi-dipolar microwave plasmas and their application to negative ion production
   Physics of Plasmas **20** (2013) 101601.
   S. Béchu, A. Soum-Glaude, A. Bès, A. Lacoste, P. Svarnas, **S. Aleiferis**, A. A. Ivanov Jr. and M. Bacal

2. H^- Negative Ion Production from a 2D-Network of ECR Dipolar Plasma Sources
   IEEE Transactions on Plasma Science **42** (2014) 2828
   S. Aleiferis, P. Svarnas, I. Tsiroudis, S. Béchu, M. Bacal and A. Lacoste

3. Automated electrostatic probe device of high resolution and accuracy
   Review of Scientific Instruments **85** (2014) 123504
   S. Aleiferis and P. Svarnas

4. Experimental investigation of the relation between H^- negative ion density and Lyman-α emission intensity in a microwave discharge
   Journal of Physics D: Applied Physics **49** (2016) 095203
   S. Aleiferis, O. Tarvainen, P. Svarnas, M. Bacal, S. Béchu

5. Hydrogen negative ion (H^-) production in an electron cyclotron resonance volume source: investigating the efficiency of dissociative attachment
   Plasma Sources Science and Technology (to be submitted)
   S. Aleiferis, P. Svarnas, O. Tarvainen, S. Béchu, M. Bacal

Conferences

1. Laser photo-detachment measurements in the ECR driven H- negative ion source Prometheus I
   39th IEEE International Conference on Plasma Science
   (9-12 July 2012, Edinburgh, France) p. 3P-50-3P-50
   S. Aleiferis, P. Svarnas, S. Béchu, M. Bacal, A. Lacoste

2. Etude expérimentale de la production et extraction des ions négatifs H- par une source multi dipolaire ECR, applicable à la fusion thermonucléaire (Poster presentation)
   Journées du réseau Plasmas Froids
   (9-12 October 2012, Ecully - Lyon, France)
   S. Aleiferis, P. Svarnas, S. Béchu

3. First experimental results on the Cybele ion source (Oral Presentation)
   Meeting of the Coordinating Committee on Neutral Beams
   (13-15 November 2012, Toulouse, France)
   S. Béchu, **S. Aleiferis**, S. Simonin, A. Bès, L. Bonny, A. Lacoste.

4. Electrostatic probe and laser photodetachment measurements in the hydrogen negative ion (H-) source Prometheus I (Oral presentation)
   20th International conference on gas discharges and their applications
   (6-11 July 2014, Orléans, France) E4 p. 494
   S. Aleiferis, P. Svarnas, I. Tsiroudis, S. Béchu, A. Lacoste, M. Bacal

5. Designing a high resolution microcontroller-based electrostatic probe system for plasma characterization (Oral presentation)
   20th International Conference on Gas Discharges and their Applications
   (6-11 July 2014, Orléans, France) M1 p.714
   S. Aleiferis, P. Svarnas

6. Study of the rovibrational levels of ground state hydrogen molecules by laser photodetachment and emission spectroscopy.
   22nd International Symposium on Plasma Chemistry
   (05-10 July 2015, Antwerp, Belgium) P-I-1-2
   S. Béchu, **S. Aleiferis**, P. Svarnas, V. A. Shakhatov, Yu. A. Lebedev, A. Lacoste

7. VUV emission spectroscopy in combined with H^- production measurements in the ion source Prometheus I.
   5th International Symposium on Negative Ions, Beams and Sources
   (12-16 September 2016, Oxford, UK) (Submitted)
   S. Aleiferis, J. Laulainen, P. Svarnas, O. Tarvainen, M. Bacal and S. Béchu

8. Experimental study of H atom recombination on different surfaces in relation to H^- negative ion production.
   5th International Symposium on Negative Ions, Beams and Sources
   (12-16 September 2016, Oxford, UK) (Submitted)
   S. Aleiferis, J. Bentounes, S. Béchu, P. Svarnas, A. Bés, A. Lacoste, L. Gavilan, J. L. Lemaire

9. Photoelectron emission experiments with ECR-driven multi-dipolar negative ion plasma source
   5th International Symposium on Negative Ions, Beams and Sources
   (12-16 September 2016, Oxford, UK) (Submitted)
   J. Laulainen, T. Kalvas, H. Koivisto, O. Tarvainen, **S. Aleiferis**, P. Svarnas

Annex: Photoelectron emission experiments

The relatively higher electron and negative ion density, which was obtained with the yttrium sample in Section 4.4, indicates that under certain conditions, the surface can be an important sources of electrons. Due to the low work function of yttrium (3.1 eV), one of the possible mechanisms, through which the surface may contribute, is the photoelectric effect. As an addition to the results presented in Chapter 4, the contribution of the photoelectric effect was experimentally investigated.

For this purpose the photoelectron meter described in [98] is employed. The experimental setup is presented in Figure A1. The source is used in two configurations. In the first, the photoelectron meter is looking in the bulk plasma of the source, 65 mm bellow the midplane of the ECR magnets (Configuration A of Figure 4.6). In the second, the meter is looking in the ECR zones, 3 mm above the midplane of the ECR magnets (Configuration C of Figure 4.6). The difference in the VUV emission intensity between the two mechanisms is quite dramatic (Figure 4.64).

The photoelectron meter is described in detail in [180]. Its construction is similar with the irradiance meters used for the VUV studies (see Section 3.1.4). A cross section of its design is presented in Figure A1. It briefly consists of two rotating disks. On the first disk facing the plasma a 2 mm collimator is adapted to limit the light that is used for the photoelectron measurements. The light that passes from the collimator illuminates the sample (photocathode) which is grounded through a pico-ammeter, measuring the photoelectron current. The sample is placed 120 mm away from the chamber wall or 240 mm away from the center of the ECR zone. In front of the photocathode there is a positively polarized anode ring (+150 V) which collects the emitted electrons. An aluminium plate, adapted on the first rotating disk, protects the sample from the VUV irradiance when measurements are not realized. This is very important, because of a long term effect in the photocathode which changes the emitted photocurrent.

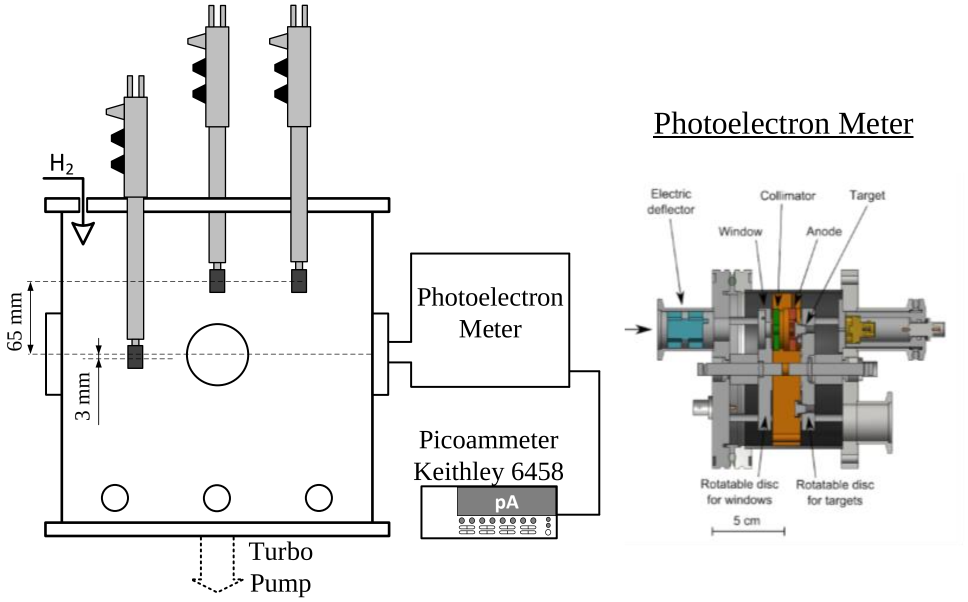

Figure A1. Experimental setup for measuring the photoelectron effect.

The sample, which is also adapted on a rotating disk, can be changed during measurements in order to study different materials. A parametric study is realized with materials typically used in plasma chambers: aluminium, copper, stainless steel, molybdenum and tantalum. The work function of such materials is in the order of 4.5 eV. For hydrogen plasmas, it is practically only the VUV photons that have enough energy to for an important photoelectron current. This is proved in [180] where a sapphire window with transmittance of about 80% in the visible region and almost 0% in the VUV, reduces the photoelectron current by three orders of magnitude (from ~10^1 nA to ~10^{-2} nA).

The photoelectron emission from the two regions is presented in Figure A2. The aluminium always has the highest current, reaching values of 140 nm when it looks in the ECR zones. The current of all the other materials is about 50% lower. Obviously, the photoelectron emission from the ECR range is much more important (about 6 times higher). The photoelectron current that is measured corresponds to a small illuminated circular surface 2 mm in diameter.

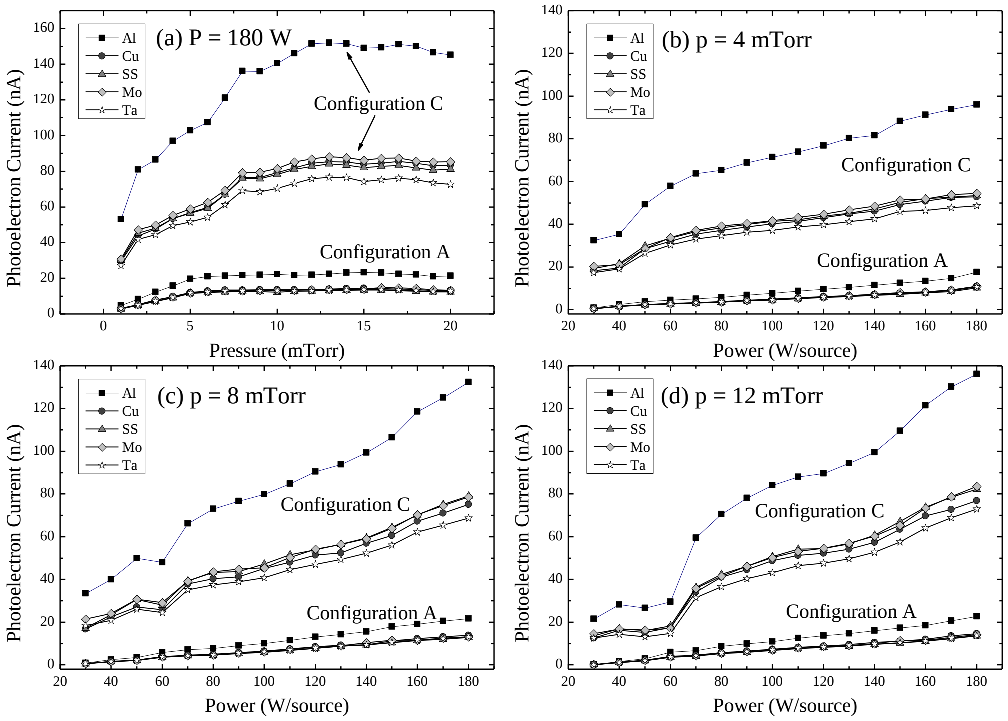

Figure A2. Sample photoelectron current when the photoelectron meter is looking in the bulk of the plasma (Configuration A) and in the ECR zone (Configuration C). In both cases, the photoelectron meter was adapted on the central viewport of the chamber. (a) Pressure dependence for Power = 180 W/source. (b) Power dependence for Pressure = 4 mTorr. (c) Power dependence for Pressure = 8 mTorr. (d) Power dependence for Pressure = 12 mTorr.

In order to determine the total contribution of photoelectron current to the electron density of the source, these measurements need to be extrapolated to account for the total internal surface of Prometheus I. This extrapolation is not straightforward and requires knowledge about: a) the light that is emitted by the plasma from its entire volume and b) how this light illuminates the various surfaces.

For the current state of Prometheus I, the material of interest is the stainless steel. The current of the stainless steel sample need to be scaled up to account for the photoelectron current from the entire chamber. Then, this current can be compared with ionization, which the main process that generates cold electrons.

For the source Prometheus I, which is characterized by an excess of vibrational states and a lack of electrons (See Section 4.4.2), an additional source of electron could be quite beneficial.